Investigations on a Flat, Square Plate at High Incidence in a Low Speed Flow

by

Aftab Ahmad

A Thesis Presented to the

FACULTY OF THE COLLEGE OF GRADUATE STUDIES

KING FAHD UNIVERSITY OF PETROLEUM & MINERALS

DHAHRAN, SAUDI ARABIA

In Partial Fulfillment of the
Requirements for the Degree of

MASTER OF SCIENCE

In

MECHANICAL ENGINEERING

May, 1988

INVESTIGATIONS ON A FLAT, SQUARE PLATE AT HIGH INCIDENCE IN A LOW SPEED FLOW

BY

AFTAB AHMAD

A Thesis Presented to the

FACULTY OF THE COLLEGE OF GRADUATE STUDIES

KING FAHD UNIVERSITY OF PETROLEUM & MINERALS

DHAHRAN, SAUDI ARABIA

In Partial Fulfillment of the
Requirements for the Degree of

MASTER OF SCIENCE

In

MECHANICAL ENGINEERING

MAY, 1988

KING FAHD UNIVERSITY OF PETROLEUM AND MINERALS
DHAHRAN 31261, SAUDI ARABIA

COLLEGE OF GRADUATE STUDIES

This thesis, written by

AFTAB AHMAD

under the direction of his Thesis Advisor and approved by his Thesis Committee, has been presented to and accepted by the Dean of the College of Graduate Studies, in partial fulfillment of the requirements for the degree of

MASTER OF SCIENCE IN MECHANICAL ENGINEERING.

Thesis Committee

Wolfgang H. Stahl

Chairman (Dr. Wolfgang H. Stahl)

Co-Chairman (Dr. David R. Otis)

Member (Dr. Muhammad U. Budair)

Member (Dr.-Ing. Roland Stuff)

Department Chairman
(Dr. Habib Abualhamayel)

Dean, College of Graduate Studies
(Dr. Abdullah S. Al-Zakari)

Date Aug 8, 1988

Dedicated

to

My Parents and Wife

ACKNOWLEDGEMENTS

Praise and thanks be to Allah, the Almighty, with whose gracious help, it was possible to accomplish this research.

Thanks are due to the King Fahd University of Petroleum and Minerals for providing support to this research.

I wish to express my deep gratitude and thankfulness to my major thesis advisor Dr. W.H.Stahl for his able guidance and help throughout the course of this research. He was always kind and sympathetic to me and made himself available at the time of my need. Working with him was indeed a wonderful experience which I thoroughly enjoyed.

I am also grateful to Dr. D.R.Otis, who served as Co-Chairman and other members of committee Dr. M.U.Budair and Dr. R.Stuff for their cooperation, help and invaluable suggestions.

I would also like to express my gratitude to Mr. M.Mahmood, Mr. M.N.Elabdin and Mr. Bakr for their help in this research.

I gratefully acknowledge the assistance provided by Dr. J.L.Knox of Electrical Engineering Department.

Finally, I would like to express my deep appreciation to Dr. Habib Abualhamayel, Chairman of Mechanical Engineering Department for his help and providing necessary facilities for carrying out this research.

page

CONTENTS

LIST OF FIGURES

ملخـــص بحـــث

ان ظاهرة التغيير الكبير والمفاجئ في القوة العادية التي تحدث في الاسقاط العالي من زاوية حرجة على الصفائح ذات السرعة المنخفضة وفي الدفق اللاانضغاطي ، تعتبر من الظواهر الهامة والمثيرة للانتباه وذلك لان هناك تطبيقات عملية لهذه الصفائح .. مثال اجنحة الصواريخ واسطح التحكم ودفات السفن والهيلوستات والهوائيات وهذا التغيير في القوة العادية من زاوية السقوط العالية يعود سببه الى التغيير في مجال الدفق .

تم فحص صفيحة مسطحة ومربعة حادة الاطراف في حالة دفق منخفض وباسقاط من زاوية حرجة مثلا (أ د 30°) وتمت دراسة مجال الانسياب عن طريق استعمال التصور الانسيابي مع تطبيق التحليل المغنطيسي الكهربائي . وتم اجراء الدفق في نفق هوائي منخفض السرعة بمعدل ٠,٨م * ١,١ م (بمعمل الابحاث الفضائية بالجامعة) .

وتم الحصول على نماذج للدفق عن طريق تقنية دفق الزيت السطحي وتصور الدفق الدخاني (بانارة بواسطة طائرة اضاءة بالليزر) أما الـ (TUFTS) فقد كانت من الصوف والورق . وتم ايضا تسجيل انسياب الدخاني في شريط الفيديو .

وتمت ايضا محاكاة الدفق الدوامي من خلال التجارب التي اجريت عن طريق التحليل المغنطيسي الكهربائي ـ بسلك حامل للتيار ومحاكاة دفق UNIFORM في المجال المغنطيسي داخل لغة اسطوانية مزودة بالتيار . تم الحصول على (نماذج دفق) عن طريق الـ IRONFILINGS . وتم استعمال نموذج نظري مبسط لوصف بعض الخصائص المميزة للدفق . وتحت العمليات الحسابية باستعمال الحاسب الالي ا ب م ٣٧٠ ـ المركزي بالجامعة .

ادت نتائج الاختبار الى نماذج دفق في جانب الامتصاص بالنسبة للصفيح واعطت التجارب معلومات اضافية عن قوى الدفق الدوامي النسبي في المحاكاة الدوامية . وفي جانب الضغط ـ من الصفيح ـ بينت نتائج فحص الدفق السطحي انحلالا في العقدة .

Investigations on a flat, square plate at high

incidence in a low-speed flow

Abstract

The phenomenon of abrupt and large change in normal force occuring at some high, critical incidence on low-aspect ratio plates in incompressible flow is of considerable interest, as such plates have practical applications, e.g. as missile wings and control surfaces, shiprudders, heliostats, and antennas. This change in normal force at high incidence has its origin in a change of the flow field.

A flat, square, sharp-edged plate was investigated in low-speed flow at subcritical incidence (i.e. $\alpha < 30°$). The flow field was studied using flow visualizations, applying an electromagnetic analogy, and using a simple theoretical approach. The flow visualization tests were carried out in the 0.8m*1.1m low-speed wind tunnel of the K.F.U.P.M. Aeronautical Laboratory. Flow patterns were obtained by means of surface oil-flow technique, smoke flow visualizations (with flow illumination by laser-light plane) and tufts of wool and paper. The smoke flow visualizations were also recorded on video tape. In experiments using the electromagnetic analogy, vortex flow was simulated by means of the magnetic field of a current-carrying wire and uniform-flow simulation was achieved by the uniform magnetic field inside a current-carrying cylindrical coil. "Flow patterns" were made visible by means of iron filings. A simplified theoretical model was used to describe some characteristic features of the flow, the computations were performed on the IBM 3033 central computer of K.F.U.P.M.

The flow visualization tests in the wind tunnel led to a conjectured, complex flow pattern on the suction side of the plate. The experiments using the electromagnetic analogy, and the results of theoretical modelling of the flow supported the conjectured flow pattern and gave additional information about the relative vortex strengths of the vortex configuration. On the pressure side of the plate, the surface flow visualization tests revealed a degenerate node.

1. INTRODUCTION AND OBJECTIVE

1.1 Introduction

The phenomenon of abrupt and large change in normal force occuring at some high incidence on low-aspect ratio plates in incompressible flow is of considerable interest, as such plates have practical applications, e.g. as missile wings and control surfaces, shiprudders, heliostats, and antennas. Such a large change in normal force impairs the manoeuvre performance of missiles and may lead to damage of the structure of heliostats and antennas.

The above phenomenon was first reported by W.H.Dines [1] for a square plate, when the incidence was increased from 35° to 40°. A typical variation of normal force with incidence for low-aspect ratio plates, as reported by S.F.Hoerner [2], is shown in Fig. 1.1. It may be seen that a sudden drop in normal force occurs around 40°. F.Ahlborn [3,4] investigated the flow field about flat, rectangular plates to get some insight into the origin of drag. He found a jump in the drag to occur on a practically square plate [4] at an incidence of about 30°, and related this to a change in the vortex system which he also observed at this incidence. Ahlborn's observations from further tests [5], on a rectangular plate of aspect ratio A=2, for different incidences, are shown in Fig. 1.2. He related the change in normal force with incidence, as found by W.H.Dines, to the rearrangement of the vortex flow field. L.Prandtl [6] also undertook

similar investigations as were done by W.H.Dines, with essentially the same findings and presented as an explanation of the abrupt change in force the change in the vortex structure, described by F.Ahlborn.

Early investigations of the three-dimensional flow field behind bluff bodies and its development with Reynolds number have been discussed in [7]. A very low-speed flow (Re <<1) past a normal plate remains attached to the rear side. When the Reynolds number is increased from 5 to 100-200, the flow separates and a permanent vortex ring exists behind the plate. Further increases in Reynolds number lead to the breakdown of the vortex ring, with successive portions shed at some distinct frequency, [8,9].

H.Winter [10] experimentally investigated a number of rectangular, flat, sharp-edged plates, which covered a wide range of aspect ratios. Fig. 1.3 shows, that the critical angle, $\alpha_{crit,u}$, at which the more or less abrupt change in normal force begins, decreases considerably with aspect ratio, A. The magnitude of the drop in normal force becomes less and less with increasing aspect ratio, and the changes become smoother.

A.E.Perry et al [11], M.Tobak and D.J.Peake [12], H.G.Hornung and A.E.Perry [13], H.G.Hornung [14], and U.Dallmann [15], inter alia, have recently investigated the geometrical and topological structures of three-dimensional, separated flows. Use was made of critical points (nodes, saddles, see Appendix I) in the flow and on

the body surface, subject to topological rules, to construct various separated flow patterns.

The effects of compressibility on the normal force on a square plate, for subsonic flows, have been studied by P.Van Westerhoven, E.Wedemeyer, and J.F.Wendt [16]. Their results are shown in Fig. 1.4. It is seen, that the large and abrupt drop occuring at a critical incidence in low-speed flow decreases and even vanishes as the Mach number increases, and that the variation becomes smoother.

In Fig. 1.5 the influence of planform shape can be seen, comparing a rectangular and a delta wing, both of aspect ratio A=1. The behaviour of the normal force with incidence is quite different for the delta plate [17] and the square plate at high incidence. The decrease in normal force occurs much less dramatically for the delta planform than for the square plate, as can be seen in the figure. Low-aspect ratio delta wings have been extensively investigated and the reason for the change in normal force is the breakdown of the leeside leading-edge vortices.

W.H.Stahl and M.Mahmood [18] carried out experiments on a flat, square, sharp-edged plate in order to obtain some insight into the phenomenon of the abrupt change in normal force at some critical incidence, α_{crit}. They found an abrupt change in normal force of about 17% to occur, with increasing incidence, at $\alpha_{crit} \approx 30°$, accompanied by distinct changes in the flow field on the wake side

and downstream of the plate. The observed flow patterns are shown in Fig. 1.6.

Recently, M.K.Abu Saleh [19] carried out experiments on the same flat, square-plate model in order to investigate the effects of Reynolds number. He found out that in the subcritical as well as in the supercritical regime the normal force is not appreciably affected by the variation of Reynolds number at constant angle of incidence, except at the critical incidence where the effect is more pronounced, see Fig. 1.7. The abrupt change in normal force occurs again at $\alpha_{crit} \approx 30°$, independent of Reynolds number. The percentage change in normal force at the critical incidence is quite appreciable. It increases linearly in the range of $Re_c = 0.5*10^5 - 1.5*10^5$ and remains approximately constant for further increases in Reynolds number.

H.Hornung and A.E.Perry [20] did experiments using electromagnetic analogy to study different types of separated flow patterns by various arrangement of the wires.

1.2 Objective

The phenomenon of abrupt and large change in normal force on the square plate at high incidence has its origin in a change of the flow field, as can be concluded from previous work [18]. It is the objective of the present study to further investigate, in greater detail, the flow field about a flat, square, sharp-edged plate in low-

speed flow at subcritical incidence (i.e. $\alpha < 30°$), in order to get as complete a knowledge of the flow structure as possible. This information then should form the basis to find out what changes occur when increasing the incidence to supercritical values. The present work builds on and carries further earlier investigations performed at K.F.U.P.M. and reported in [18,19]. The flow field is to be studied using flow visualizations, applying an electromagnetic analogy, and using a simple theoretical approach.

2. MODEL, EXPERIMENTAL EQUIPMENT, AND THEORETICAL APPROACH

The investigations essentially comprised of:

(a) Flow visualization tests in the wind tunnel

(b) Experiments using an electromagnetic analogy

(c) A theoretical approach

2.1 Flow Visualization Model and Wind Tunnel

The flow visualization tests were carried out on a flat, square, sharp-edged plate, made of plexiglass, with chord length C= 0.22 m. The model with its support system is shown in Fig. 2.1. The plate could be oriented in the free stream between α = 0° and 90°.

The flow visualization tests were carried out in the low-speed wind tunnel of the K.F.U.P.M. Aeronautical Laboratory. The wind tunnel has a closed, rectangular test section of 0.8m*1.1m cross-sectional area. The tunnel is of the open return type with a maximum wind speed of $V_\infty \approx 35$ m/s in the empty test section. Fig. 2.2 gives an overall view of the wind tunnel.

2.2 Flow Visualization Equipments and Procedure

Various flow visualization techniques were used. The flow pattern on the surface of the plate was made visible by means of a surface oil-flow technique. A mixture of kerosene and chalk powder was

sprayed evenly on the plate surface with a spray gun; under the action of the air flow the wall streamline pattern became visible.

The outer flow, especially on the suction side of the plate, was made visible with the aid of smoke. For generating the smoke, a straight tube, bent at right angle near its tip, was used. Oil was fed to the probe and vaporized at the tip by a built-in, electrically heated, coil. The smoke probe and its supply and control unit are shown in Fig. 2.3.

The flow was made visible by introducing smoke from the probe at various locations within the flow field and also through holes in the model, at the plate surface. The flow was illuminated with the aid of a laser-light plane. The arrangement of laser-light source, lenses, and mirror is shown in Fig. 2.4. The smoke flow visualizations were recorded on video tape in order to study the temporal behaviour of the generally unsteady flow.

Simple tufts of wool and paper were used to visualize the flow direction near and above the surface of the plate.

2.3 Electromagnetic Analogy

In this investigation, the flow field about a line vortex was simulated by means of the magnetic field existing about a current-carrying wire, put in place of the vortex line. Uniform-flow simulation was achieved by using the uniform magnetic field inside a current-carrying cylindrical coil. "Flow patterns" were made visible

by iron filings. The strength of the magnetic field could be varied by changing the strength of the current in the wire representing a vortex (See Appendix III for a detailed discussion of the electromagnetic analogy).

The wind tunnel model was represented by part of a rectangular, flat plexiglass plate, with the outlines of the square plate under investigation marked on it. Current-carrying wires represented the vortex configuration observed in the wind tunnel tests, an image wire-arrangement was used to fulfil the boundary conditions on the plate. The entire plate and wire arrangement could be inserted into the current-carrying cylindrical coil and exposed there to a uniform, axial magnetic field. Iron filings, applied to the plate, indicated the resulting "streamlines". The linear dimensions of the arrangement were reduced to about half the values of the corresponding dimensions of the wind tunnel model. The apparatus used is shown schematically in Fig. 2.5.

The current was provided by a D.C. power-supply unit, with maximum voltage and current of 40v and 120A, respectively. In each wire circuit a rheostat was connected in series; by varying the resistance, the current could be distributed in the various circuits according to the desired strengths of the vortices. All circuits were connected to the common terminals of the power-supply unit.

The model was made of plexiglass, also the supporting cylinder of the coil. For the "vortex" wires copper welding rods were used. The

"vortex"-wire (d= 2.5 mm) arrangement used is depicted schematically in Fig. 2.6 and the experimental set-up for the investigations using the electromagnetic analogy is seen in Fig. 2.7.

2.4 A Theoretical Approach

It has been observed that vortices play a major role in the flow on the wake side of the plate. The assumption was made, that these vortices could be represented, to some extent, by straight, two-dimensional, potential-vortex lines. The principle of superposition (See Appendix II) was used to find the resultant stream function, ψ_R, and streamlines (i.e. lines ψ_R = constant) due to the observed vortices and to image vortices, needed to fulfil the boundary conditions at the plate. The values of the resultant stream function were computed on the IBM 3033 central computer of K.F.U.P.M., using a FORTRAN compiler. These data were then put into the SURFACE-II plotting system. The execution time was about 5-6 minutes (for about 2000 data points) and the results, in the form of streamlines ψ_R = constant, were plotted on the Calcomp plotter.

3. RESULTS AND DISCUSSION

3.1 Flow Visualization

The phenomenon of abrupt change of the normal force on a flat, square, sharp-edged plate at some high incidence has its origin in the change of the flow field. W.H.Stahl and M.Mahmood [18] and M.K.Abu Saleh [19] investigated the flow field at angles of attack below and above the critical angle of about 30°, at which the change occurs. It was decided to investigate the flow field about the plate in greater detail, at subcritical incidence, $\alpha < 30°$, to obtain as complete a knowledge as possible of the flow structure.

Most of the tests were carried out at a free-stream velocity V_∞ = 7.3 m/s, to which corresponds a Reynolds number

$$Re_c = \frac{V_\infty \cdot C}{\nu_\infty} = 1.1*10^5 \quad .$$

A subcritical incidence of α = 25° was chosen. For surface flow visualization an oil-flow technique was used, and the flow region away from the plate was made visible by introducing smoke and illuminating the flow by laser-light sheets. Also tufts were used to some extent to visualize the flow.

3.1.1 Suction Side of the Plate

First some results of earlier surface flow visualization on the model suction side by W.H.Stahl and M.Mahmood [18] are presented,

as they formed the starting point for the present investigations.

Fig. 3.1 shows the flow pattern on the surface of the plate on suction side at subcritical incidences, α = 28° and 30°, and at a supercritical incidence, α = 32°, as obtained by the oil-flow technique. These visualization tests had to be done at a Reynolds number of $Re_c = 2.6*10^5$, as it was not possible to obtain clear patterns at the lower Reynolds number of $Re_c = 1.1*10^5$, established in the present tests. Therefore, and also because Fig. 3.1a and b were obtained at somewhat larger angles of attack than used in the present work (α = 25°), the flow field was checked under the present test conditions, whether it corresponds to that of Fig. 3.1. It was established that topologically the same type of flow also exists under the present test conditions on the suction surface of the plate.

The wall streamline pattern in subcritical flow, seen in Fig. 3.1a and b, is characterized by a number of critical points, i.e. points where the directions of the streamlines are indeterminate. They lend a distinctive structure to the flow pattern. The theoretical aspects of critical points have been dealt with extensively in Appendix I. An attempt to interpret the surface flow visualization pictures has been made and the result is presented in Fig. 3.2. There is a node, N, on the centerline near the trailing edge. It is not clear, whether the centerline or the normal to it, is the line to which the streamlines leave the node tangentially. Near the leading

edge, on the centerline, is a saddle point, S_1, connected with the rear node, N, by a wall streamline. Two foci, F_1 and F_2, can be recognized in the front part, placed symmetrically with respect to the centerline. Between the saddle point, S_1, and each of the two foci, F, we have a line along which the flow on the plate merges from both sides and separates from the wall. This is a socalled negative bifurcation line. Two saddle points, S_2 and S_3, are conjectured to be present, placed symmetrically to the centerline, as indicated in Fig. 3.2. Each of the saddles structures the flow into that going towards the neighbouring focus and that turning away from it. At each of the saddle points two negative bifurcation lines originate, one connecting to the adjacent focus and one extending towards the trailing edge. Additional oil-flow visualization tests revealed that on the narrow strip between the straight leg of the bifurcation line and the side edge (practically blank in Fig. 3.1), oil is pushed towards the bifurcation line. The flow is converging to these bifurcation lines from both sides and separating there from the surface.

A surface flow pattern very similar to that on our plate was observed by B.D.Fairlie [21] on the suction side of a circular cylinder with a hemispherical nose at $\alpha = 25°$ in a flow with a free-stream Mach number of $Ma_\infty = 0.55$ and $Re_d = 10^6$.

Some effort was then spent on visualizing the flow field above the

plate on suction side at $\alpha = 25°$ and $Re_c = 1.1*10^5$ by means of tufts and smoke.

With the aid of a tuft probe a focus could be detected on each side of the plate, at a position about a quarter chord from the leading and side edges, respectively. The tuft indicated fluid spiralling away from the plate with clockwise sense of rotation on the right hand side (looking upstream) and with opposite sense on the other side. This vortex flow was observed to leave the wall perpendicularly and after a short distance to turn in downstream direction. In order to obtain further evidence smoke was introduced through a hole in the plate at one of the foci. The smoke flow was examined in laser-light planes, which were placed at various distances parallel to the surface and with various inclinations to it. These observations confirmed our earlier findings about the vortex flow at a focus. After the vortex had turned downstream, it could be traced only a small distance, then it was no longer discernible in the highly instationary flow. The observed flow is sketched in Fig. 3.3. It is largely in accordance with the surface oil-flow picture (Fig. 3.1).

Next, the flow about the plate was studied in the symmetry plane in a laser-light sheet, with smoke fed into the flow at various places. The results of these observations are sketched in Fig. 3.4. The dominant feature of the flow is the large rotating mass of fluid on the suction side, with its center at or somewhat upstream of the middle

of the plate. A strong flow in forward direction was found to exist near the wall, as is also suggested by the surface oil-flow picture, Fig. 3.1a. Near the trailing edge, the flow can be seen to go towards the plate and attach to it in a region where a node is showing up in the wall oil-flow pattern. The forward flow on the surface separates near the leading edge, as is also indicated in the oil-flow picture. Interestingly, the upward flow partly turns backward into the free-stream direction, and partly it moves forward, against the outer flow, apparently attaching at the leading edge. The vortical flow, indicated behind the leading edge, is conjectured, it could not be observed in the tests. The flow moves smoothly past the trailing edge from both suction and pressure sides, no coiling up could be detected near the edge. This is in accordance with the results of earlier investigations on the plate [18], when no vortex shedding was observed at subcritical angles of attack.

Considering the critical points in the sectional flow in Fig. 3.4, we can apply the topological rule given in Appendix I, which states, that the number of saddles, S, exceeds the number of nodes, N, (including foci, F) by one :

$$\Sigma S = \Sigma N + 1 \quad ,$$

It can be seen, that with

$$\Sigma S = 3 \text{ and } \Sigma N = 2,$$

this relation is satisfied.

At the sharp side edges of the plate the flow separates and coils up into the well documented side-edge vortices, lying above the plate. They were clearly seen in the smoke flow visualizations in laser-light planes, and were confirmed by using tufts. Each side-edge vortex apparently starts at the respective front corner, with its axis inclined to the plate at an angle of about $\frac{\alpha}{2}$, as observed also by others [18,19]. The diameter of the vortex flow increases with increasing distance from the leading edge.

In the region between the side-edge vortices the flow was found to be highly instationary, with a very rugged boundary. Distinct gaps separate this inner flow region from the side-edge vortices. The observed flow is sketched in Fig. 3.5, photographs of the flow are presented in Fig. 3.6.

3.1.2 Pressure Side of the Plate

On the pressure side, the surface flow pattern exhibited an attachment line near the leading edge, which extended some distance to both sides of the symmetry plane, closely resembling to a degenerate node, as discussed in Appendix I. This, however, had to be concluded with the aid of tests at higher angles of attack at a higher Reynolds number, as oil-flow patterns at angles of attack around $\alpha = 25°$ and at $Re_c = 1.1*10^5$ were not very conclusive as to

the flow near the leading edge. A photograph of the surface oil-flow pattern on pressure side at $\alpha = 25°$ and $Re_c = 2.6*10^5$ is given in Fig. 3.7.

3.1.3 Conjectured Flow Field about Plate

With this information obtained in our tests, an attempt was made to construct the flow field past the plate at subcritical incidence. The conjectured flow configuration, based on the available experimental evidence and taking heed to Helmholtz' vortex theorems, is presented in Fig. 3.8. The time-mean flow pattern on the suction side of the plate is sketched in the flow symmetry plane and on the plate surface, and a skeleton of the vortices embedded in the flow is given (Only the starboard side of the plate is shown). The vortex, observed in the symmetry plane, (subsequently termed symmetry-plane vortex) extends some distance in spanwise direction and then turns in downstream direction. According to Helmholtz' vortex theorems, it must either continue to downstream infinity on both sides or it must form a closed loop. It was not possible, on the basis of our observations, to decide which vortex configuration actually exists. However, the vortex core, as drawn in the figure, is compatible with the wall streamline pattern underneath the vortex. The vortices, which have been observed to originate in the two foci ("focal vortices") and which could be seen only over a short distance, have been extended downstream; again, their continuation is not known.

Near the leading edge a vortex has been conjectured, which could not be detected in the flow observations, probably because it is very weak. This "leading-edge vortex" is, however, compatible with the flow observed in the symmetry plane. It is assumed to extend parallel to the leading edge about the symmetry plane, and to turn towards the foci on both sides and then wrap around the focal vortices. The two side-edge vortices drawn complete the picture of the vortex skeleton.

No special features were observed on the pressure side.

3.2 Electromagnetic Analogy

The flow visualization tests performed in the wind tunnel led to the conjectured flow field on the suction side of the plate, at subcritical incidence, as presented in Fig. 3.8. Investigations, making use of the electromagnetic analogy, were subsequently carried out in order to obtain additional information, which could support or refute the conjectured flow pattern. The electromagnetic analogy is described in detail in Appendix III.1.

Fig. 2.7 shows the experimental set-up. The wires above the plate represent the vortex skeleton of the conjectured flow. The wire representing the leading-edge vortex is not present in the arrangement shown. The wires on the lower side are in place of the image vortices, used to satisfy the boundary conditions of the flow at

the plate surface. The strength of the electrical current, I, is constant along the wire and therefore also the magnetic field induced about it. This implies that line vortices of constant strength, Γ, are simulated, which is not necessarily the case in the real flow. E.g., the increasing strength, Γ, in downstream direction of a side-edge vortex is not taken care of. At the outset of the experiments, the distribution of the strengths of the currents, i.e. the strengths of the vortices was chosen according to the visual observations in the wind tunnel of the vortical flows. Subsequently, these necessarily ambiguous current strengths were adjusted to give better agreement between the pattern of the iron filings and the one observed in the wind tunnel. This "vortex" arrangement was placed into the homogeneous magnetic field inside the cylindrical coil, as shown schematically in Fig. 2.5. The strength of this field was also varied during the tests.

The "flow" pattern obtained by use of the electromagnetic analogy, on the surface of the plate is presented in Fig. 3.9. In this test the leading-edge vortex conjectured was not included in the simulation. It can be seen that the topological features of the real flow are also showing up in the simulation, at least qualitatively. We find again the node on the rear part of the plate, however, shifted considerably forward. The saddle point near the leading edge in the symmetry plane, as well as the foci on the left and right hand side, respectively, are present. Negative bifurcation, or separation, lines connect the saddle to each focus. The saddle point conjectured to be

present somewhat downstream of a focus, is now confirmed by the electromagnetic analogy. At least one of the two separation lines, emerging from such a saddle in opposite directions, can be seen. However, the flow near the side edges is not correctly simulated.

Next, the leading-edge vortex, conjectured on the basis of the flow observations in the wind tunnel, was added in the electromagnetic simulation. The flow pattern was not significantly altered, as can be seen in Fig. 3.10. Only near the leading edge the flow is seen to be less divergent than is the case in the absence of the leading-edge vortex. The presence of such a vortex, which is probably very weak, is not excluded on grounds of this simulation.

The flow was also investigated in the symmetry plane by rotating the whole arrangement through 90°, thus orientating the symmetry plane horizontally. The set-up and a result is seen in Fig. 3.11. The picture shows clearly the symmetry-plane vortex flow. However, it is not very conclusive as to the flow near the leading edge, mainly due to the limited power supply.

It is concluded, that the results, obtained by use of the electromagnetic analogy, are largely in accordance with the flow structure as conjectured from the results of the various flow observations in the wind tunnel. Further tests using the electromagnetic analogy, would probably have provided still closer agreement between the flow patterns, and indicative values could have been attained of the relative vortex strengths in the vortex

configuration. This, however, was curbed by the limitations of the power supply.

3.3 A Theoretical Approach

A theoretical analysis of the flow field on the wake side of the plate was carried out under the assumption of potential and incompressible flow. The principle of superposition was used to find the resultant flow, due to the vortex flows and a uniform flow. Information obtained from the flow visualization tests in the wind tunnel and from the experiments using the electromagnetic analogy were used to model the flow.

The analysis was first made for the flow in a plane perpendicular to the plate centerline, shown in Fig. 3.12. The resultant stream function, ψ_R, due to the vortices is given as :

$$\psi_R(x,y) = \frac{1}{4\pi} *$$

$$\left[\Gamma_1 \ln \left\{ \frac{(a_1 - x)^2 + (b_1 + y)^2}{(a_1 - x)^2 + (b_1 - y)^2} \right\} + \Gamma_2 \ln \left\{ \frac{(a_2 + x)^2 + (b_2 - y)^2}{(a_2 + x)^2 + (b_2 + y)^2} \right\} \right.$$

$$+ \Gamma_3 \ln \left\{ \frac{(a_3 + x)^2 + (b_3 + y)^2}{(a_3 + x)^2 + (b_3 - y)^2} \right\} + \Gamma_4 \ln \left\{ \frac{(a_4 + x)^2 + (b_4 - y)^2}{(a_4 + x)^2 + (b_4 + y)^2} \right\}$$

$$\left. + \Gamma_5 \ln \left\{ \frac{(a_5 + x)^2 + (b_5 + y)^2}{(a_5 + x)^2 + (b_5 - y)^2} \right\} + \Gamma_6 \ln \left\{ \frac{(a_6 + x)^2 + (b_6 - y)^2}{(a_6 + x)^2 + (b_6 + y)^2} \right\} \right] .$$

With appropriate values of the parameters a_i, b_i (see Appendix II.2.2 for details), the results obtained for various combinations of the strengths of the vortices, Γ, are shown in Fig. 3.13. It can be seen from the plots that the flow field of Fig. 3.13c strongly resembles to the observations of the flow visualization tests. Furthermore, the relative strengths of the vortices, Γ, are in good agreement with those obtained from the experiments using the electromagnetic analogy. It was observed in the flow visualizations (see Fig. 3.5b) that there was a gap inboard of each side-edge vortex. In Fig. 3.13c it can be seen that the (calculated) flow is moving downwards between the streamlines A and B, this flow pattern being similar to the observed flow pattern in this region.

Next, the theoretical analysis was made for the flow in the symmetry plane, shown in Fig. 3.14, taking into account the symmetry plane vortex and the leading-edge vortex. The resultant stream function, ψ_R, is given as :

$$\psi_R\,(z,y) = \frac{1}{4\pi}\left[\,\Gamma_3 \ln\left\{\frac{(c_3 + z)^2 + (b_3 + y)^2}{(c_3 + z)^2 + (b_3 - y)^2}\right\}\right.$$

$$\left. + \Gamma_7 \ln\left\{\frac{(c_7 - z)^2 + (b_7 - y)^2}{(c_7 - z)^2 + (b_7 + y)^2}\right\}\right] - V_\infty\, y \quad .$$

Again, with appropriate values of b_i, c_i (see Appendix II.2.3 for details), the results are plotted and shown in Fig. 3.15. It can be

seen from the plots that the computed flow about the symmetry-plane vortex is, in essence, consistent with the flow observed in the wind tunnel. The computed flow field in the region near the leading edge is considerably different from the observed flow. This is probably largely due to the fact that the focal vortices and the side-edge vortices have not been included in the theoretical model. The velocities, which are induced by these vortices, especially by the two focal vortices, will cause the resultant flow field to become more consistent with the observed flow.

4. CONCLUSIONS

Extensive flow visualization tests, carried out in the wind tunnel on a flat, square, sharp-edged plate at subcritical incidence ($\alpha < 30°$) led to a conjectured, complex flow structure on the suction side.

Investigations, making use of the electromagnetic analogy, were subsequently carried out to test the conjectured flow pattern. The results were largely in accordance with the conjectured flow pattern, additional information was obtained about the relative vortex strengths of the vortex configuration. Further tests to get more information were curbed by the limitations of the power supply.

Further studies were carried out by theoretical modelling of the flow on the wake side. The computed flows in a plane normal to the centerline and in the symmetry plane, were reasonably consistent with the results of the flow visualization tests, except near the leading edge. The differences observed there were probably largely due to the fact that the focal vortices and the side-edge vortices were not included in the theoretical model. The relative strengths of the vortices, obtained by the theoretical model, were in good agreement with those obtained from the experiments using the electromagnetic analogy.

On the pressure side of the plate, the surface flow visualization tests revealed a degenerate node, inferred from higher angles of attack. No other special features were observed.

As a logical continuation, a corresponding detailed investigation should be carried out of the flow structure on the suction side of the plate at a supercritical angle of attack ($\alpha > 30°$). This should enable as to correlate changes in the flow field with the abrupt, large change in normal force.

APPENDIX I

Critical Point Theory

I.1 Background

Critical point theory (or phase-plane or phase-space method) was originally developed in the field of nonlinear dynamical systems. In more recent times, it has been used to some extent to study fluid-flow patterns; see e.g. A.E.Perry and B.D.Fairlie [24], H.G.Hornung and A.E.Perry [13], and A.E.Perry and H.G.Hornung [25].

Consider a nonlinear differential equation of second order, which does not explicitly contain the independent variable, t, (termed an autonomous equation). This second order equation can be reduced to a system of two first order autonomous equations :

$$\frac{dx_1}{dt} = \dot{x}_1 = P(x_1, x_2) \quad , \tag{I.1}$$

$$\frac{dx_2}{dt} = \dot{x}_2 = Q(x_1, x_2) \quad . \tag{I.2}$$

In order to study the original equation topologically, the quantities x_1 and x_2 are taken as cartesian coordinates, forming the socalled "phase-plane". If one divides (I.2) by (I.1) one obtains :

$$\frac{\dot{x}_2}{\dot{x}_1} = \frac{dx_2}{dx_1} = \frac{Q(x_1,x_2)}{P(x_1,x_2)} \quad . \tag{1.3}$$

This differential equation specifies, in the phase-plane, definite curves, the socalled phase trajectories or solution trajectories, of the differential equation (or the equivalent system of equations).

A point $(\bar{x}_1,\bar{x}_2)$ in the phase plane, for which

$$\frac{dx_1}{dt} = \dot{x}_1 = P(\bar{x}_1,\bar{x}_2) = 0 \tag{1.4}$$

and simultaneously

$$\frac{dx_2}{dt} = \dot{x}_2 = Q(\bar{x}_1,\bar{x}_2) = 0 \quad , \tag{1.5}$$

is called a singular, or critical, or equilibrium point.

It is convenient to consider the derivatives $\frac{dx_1}{dt}$ and $\frac{dx_2}{dt}$ as the x_1- and x_2- components of the velocity of the point $P(x_1,x_2)$ on the phase, or solution, trajectory.

A trajectory and a critical point are shown, for illustration, in Fig. 1.1 (representing a damped oscillator). The trajectory gives the evolution with time of the system from initial conditions $x_1(0)$ and $x_2(0)$. In general, there is only one trajectory passing through a point (x_1,x_2) i.e. the solution is unique. Starting with different pairs of initial conditions leads to different solution

trajectories, these are forming a socalled " phase-plane portrait". In general, these trajectories do not cross.

At a critical point $(\tilde{x}_1, \tilde{x}_2)$ the slope of the solution trajectory is seen from equations (1.4) and (1.5) to be indeterminate :

$$\frac{dx_2}{dx_1} = \frac{\dot{x}_2}{\dot{x}_1} = \frac{0}{0} \quad . \tag{1.6}$$

A detailed discussion of critical point theory is found e.g. in [26,30]. Such phase-plane portraits bear strong resemblance to flow patterns, as e.g. the trajectory in Fig.1.1 resembles to wall streamlines of the flow on the flat plate near the foci, see Fig. 3.2.

In a fluid flow the solution trajectories give simply the position (x_1, x_2) of a fluid particle; the derivatives $\frac{dx_1}{dt}$ and $\frac{dx_2}{dt}$ are the velocity components in x_1 and x_2 directions, respectively. The analogy which exists between flow patterns and phase-plane portraits is purely mathematical. Some aspects have to be regarded with caution, but the geometrical features of critical points are the same in flow patterns and nonlinear dynamical system analysis.

We consider now the behaviour of the solution of equations (1.1) and (1.2) in a small neighbourhood of a critical point, placed at the origin O. To this end, we use Taylor expansions of the functions $P(x_1, x_2)$ and $Q(x_1, x_2)$ about the critical point at O. Retaining only

the first order terms in the expansions and with (1.4) and (1.5), we get a system of linear equations :

$$\dot{x}_1 = P_{x_1} \cdot x_1 + P_{x_2} \cdot x_2 \qquad (1.7)$$

$$\dot{x}_2 = Q_{x_1} \cdot x_1 + Q_{x_2} \cdot x_2 \quad . \qquad (1.8)$$

Furthermore, we have

$$\frac{dx_2}{dx_1} = \frac{Q_{x_1} \cdot x_1 + Q_{x_2} \cdot x_2}{P_{x_1} \cdot x_1 + P_{x_2} \cdot x_2} = \frac{\dot{x}_2}{\dot{x}_1} \quad , \qquad (1.9)$$

With P_{x_1}, P_{x_2}, Q_{x_1}, Q_{x_2} the partial derivatives with respect to the coordinates x_1, x_2, at the origin, being constants.

The system of equations (1.7), (1.8) is expressed as :

$$\begin{bmatrix} \dot{x}_1 \\ \dot{x}_2 \end{bmatrix} = \begin{bmatrix} P_{x_1} & P_{x_2} \\ Q_{x_1} & Q_{x_2} \end{bmatrix} \cdot \begin{bmatrix} x_1 \\ x_2 \end{bmatrix} \qquad (1.10)$$

$$(\text{or} \quad \dot{\vec{x}} = [D] \cdot \vec{x})$$

where the determinant of the coefficient matrix, $D = \frac{\partial(P,Q)}{\partial(x_1,x_2)}$, is the Jacobian. It has, in general, eigenvalues, λ_1, λ_2, which may be either real or complex. These eigenvalues determine phase planes,

which contain solution trajectories.

We can now classify possible critical points, they are represented in the graph in Fig. 1.2. The coordinate axes are given by :

$$p = - (P_{x_1} + Q_{x_2}) \tag{1.11}$$

and

$$q = (P_{x_1} . Q_{x_2} - P_{x_2} . Q_{x_1}). \tag{1.12}$$

The eigenvalues are :

$$\lambda_{1,2} = - \frac{1}{2}[p \pm \sqrt{(p^2 - 4q)}] \quad . \tag{1.13}$$

The terms "stable" and "unstable", in Fig. 1.2, stem from dynamical systems theory, they are not related to hydrodynamic stability. Here they simply indicate the direction of the flow, shown by the arrows.

Besides the regular critical points (nodes, including foci, saddles) there exist, for values of p and q on the axes and on the parabola $p^2 = 4q$, degenerate critical points (node-saddles, centres, node-foci, star-nodes). At the origin O, only one of the infinitely many degenerate critical points is shown which can occur there (see e.g. [30]).

Carrying the analysis over to three dimensions, a critical point is one for which the slopes of the solution trajectories are indeterminate in space.

The corresponding set of equations is then, after linearization, written as follows :

$$\begin{bmatrix} \dot{x}_1 \\ \dot{x}_2 \\ \dot{x}_3 \end{bmatrix} = \begin{bmatrix} P_{x_1} & P_{x_2} & P_{x_3} \\ Q_{x_1} & Q_{x_2} & Q_{x_3} \\ R_{x_1} & R_{x_2} & R_{x_3} \end{bmatrix} \cdot \begin{bmatrix} x_1 \\ x_2 \\ x_3 \end{bmatrix} \qquad (1.14)$$

The coefficient matrix has three eigenvalues, and three eigenvectors, which will be either real or complex. If they are real, they define phase planes, containing solution trajectories, i.e. streamlines, near the critical point.

Equations of the above type for the velocity (1.14) near a critical point are substituted into the governing equations for incompressible fluid flow, namely :

Continuity equation : $$\nabla . \vec{V} = 0 \qquad (1.15)$$

Navier-Stokes equation : $$\frac{D\vec{V}}{Dt} = - \nabla(\frac{p}{\rho}) + \nu . \nabla^2 \vec{V} \qquad (1.16)$$

written in the ususal fluid mechanics notation. Here p is the pressure, ρ the fluid density, ν the kinematic viscosity, and

$$\vec{V} = u\vec{i} + v\vec{j} + w\vec{k} \quad , \qquad (1.17)$$

where

$$u = \dot{x}_1 = \dot{x}$$

$$v = \dot{x}_2 = \dot{y}$$

$$w = \dot{x}_3 = \dot{z} \quad .$$

We now shall assume solutions $\vec{V}$ of linearized form.

1.2 Viscous or No-Slip Critical Points

We consider the viscous, incompressible fluid flow on the surface of a body in the neighbourhood of a critical point, which is located at the origin of the coordinate system, shown in Fig. 1.3.

As the no-slip condition at the wall requires that $\frac{\vec{V}}{z} \to$ constant as $z \to 0$, we assume a solution of the following form (as discussed above) :

$$\begin{bmatrix} \frac{u}{z} \\ \frac{v}{z} \\ \frac{w}{z} \end{bmatrix} = \begin{bmatrix} e_1 & f_1 & g_1 \\ e_2 & f_2 & g_2 \\ e_3 & f_3 & g_3 \end{bmatrix} \cdot \begin{bmatrix} x \\ y \\ z \end{bmatrix} \quad , \qquad (1.18a)$$

or

$$\frac{\vec{V}}{z} = \frac{\vec{\dot{x}}}{z} = F \cdot \vec{x} \quad , \qquad (1.18b)$$

which we substitute into equation (1.15) and (1.16). We obtain the elements of the coefficient matrix F (for details see A.E.Perry and B.D.Fairlie [24]) as follows :

$$\left.\begin{array}{lll} e_1 = \eta_x & f_1 = \eta_y & g_1 = (\frac{p}{\rho})_x \cdot \frac{1}{2v} \\ e_2 = -\xi_x & f_2 = -\xi_y & g_2 = (\frac{p}{\rho})_y \cdot \frac{1}{2v} \\ e_3 = 0 & f_3 = 0 & g_3 = \frac{1}{2}(\xi_y - \eta_x) \end{array}\right\} \quad (1.19)$$

The subscripts denote partial differentiation, and the vorticity, $\vec{\Omega}$, is defined as

$$\begin{aligned} \vec{\Omega} &= \text{Curl } \vec{V} \\ &= \xi \vec{i} + \eta \vec{j} + \zeta \vec{k} \\ &= (\frac{\partial w}{\partial y} - \frac{\partial v}{\partial z}).\ \vec{i} + (\frac{\partial u}{\partial z} - \frac{\partial w}{\partial x}).\ \vec{j} + (\frac{\partial v}{\partial x} - \frac{\partial u}{\partial y}).\ \vec{k} \end{aligned} \quad (1.20)$$

Case (a) :

If the eigenvalues, equation (1.13), of the coefficient matrix F are all real, then we obtain three real eigenvectors, which define three phase planes, containing solution trajectories, i.e. streamlines. Letting the yz plane be a plane of symmetry, (with $(\frac{p}{\rho})_x = \xi_x = \eta_y = 0$) then the three phase planes are the xy plane, containing the wall, the yz symmetry plane, and an xs plane, as shown in Fig. 1.4. The critical point manifests itself as a saddle

point in the symmetry plane yz, as well as in the wall plane xy, and as a nodal point in the separated-flow plane xs. We refer here to this combination as a saddle-saddle-node trio.

Considering now a situation in which the vorticity component in y direction does not change normal to the symmetry plane yz, i.e. $\eta_x = 0$, eqn. (I.18a) becomes :

$$\left.\begin{aligned} \frac{u}{z} &= 0 \\ \frac{v}{z} &= f_2 . y + g_2 . z \\ \frac{w}{z} &= - f_2 . \frac{z}{2} \ , \end{aligned}\right\} \qquad (I.21)$$

describing the flow with two-dimensional separation shown in Fig. I.5. This is a degenerate case, vis. also Fig. I.2.

The angle θ between the wall and the separated-flow plane is given by :

$$\tan\theta = \frac{w}{v} = \frac{z}{y} = \frac{3.\nu.\xi_y}{\left(\frac{p}{\rho}\right)_y} \ . \qquad (I.22)$$

using (I.21).

Case (b) :

There are three eigenvalues of the coefficient matrix F of (I.18),

two of them complex and one real. In this case, we have only one plane containing solution trajectories, and that is the wall. The flow in the neighbourhood of this critical point, a focus, is shown in Fig. 1.6. Streamlines above the wall are seen to spiral around the eigenvector $\vec{s}$, which originates in O. Such critical points have been discussed by T.T.Lim, M.S.Chong, and A.E.Perry in [27].

Similarly, the analysis has been carried out with $\frac{\vec{V}}{z}$ expanded to higher order by U.Dallmann [15] and A.E.Perry [23]. The latter obtained a simple third-order solution (assuming symmetry in y to keep the problem manageable), which to the first-order approximation was degenerate. Fig. 1.7 shows A.E.Perry's solution, the pattern of a flow separation near an almost two-dimensional critical point.

1.3 Inviscid or Free-Slip Critical Points

These are critical points, which occur in the flow away from the wall, where the no-slip condition does not apply (though the fluid is, of course, viscous).

We assume a solution, $\vec{V}$, of the governing equations, expanded in a Taylor series around the critical point and with only first-order terms retained :

$$\begin{bmatrix} u \\ v \\ w \end{bmatrix} = \begin{bmatrix} e_1 & f_1 & g_1 \\ e_2 & f_2 & g_2 \\ e_3 & f_3 & g_3 \end{bmatrix} \cdot \begin{bmatrix} x \\ y \\ z \end{bmatrix} \qquad (1.23a)$$

or

$$\vec{V} = G.\vec{x} \qquad (1.23b)$$

We substitute into the continuity and Navier-Stokes equations, (1.15) and (1.16) respectively, and obtain the coefficients. It turns out, that the viscous terms are zero in this approximation, and such critical points are termed "inviscid" critical points.

Case (a) : <u>The case of Finite Vorticity</u>

Vorticity, $\vec{\Omega}$, is defined as before in eqn. (1.20). Substituting the velocity components from (1.23a) into (1.20), relations are obtained between the components of the vorticity vector, $\vec{\Omega}$, and the coefficients. The detailed workings to obtain the coefficients are given by A.E.Perry in [23] and are not repeated here.

With the known coefficients, the pressure field is obtained expressed as the kinematic pressure, $P = \frac{p}{\rho}$:

$$P = \frac{A_1}{2}(x^2 + y^2) + P(O) \quad , \qquad (1.24)$$

where P(O) is an arbitrary constant pressure at the origin and $A_1 = \text{const.} = P_{xx}$.

The coefficients in eqn. (1.23a) are :

$$\left.\begin{array}{lll} e_1 = \pm\sqrt{-P_{xx} - e_2(e_2 - \zeta)} & f_1 = e_2 - \zeta & g_1 = 0 \\ e_2 & f_2 = \mp\sqrt{-P_{xx} - e_2(e_2 - \zeta)} & g_2 = 0 \\ e_3 = 0 & f_3 = 0 & g_3 = 0 \end{array}\right\} \quad (1.25)$$

where e_2 depends on the orientation of the flow pattern in the xy plane.

We consider the flow in the xy plane with the coefficients e_1, f_1, e_2, f_2. Determining the values of p and q of the p-q chart in Fig. 1.2 from eqn. (1.11) and (1.12), we can classify the critical points as saddles and centres. The eigenvalues λ_1 and λ_2 are obtained from eqn. (1.13). If they are real, we have a saddle, if they are imaginary, we have a centre. It can be shown, that in the case of saddles we have a pressure maximum, and in the case of centres a pressure minimum.

Without loss of generality the value of e_2 can be adjusted, such that all streamlines cut the x and y axes at right angles. If the parameters P_{xx} and ζ, appearing in the coefficient matrix, are varied, such that $\frac{P_{xx}}{\zeta^2}$ varies from $-\infty$ to $+ 1/4$, we obtain the family of flow patterns shown in Fig. 1.8, progressing from an irrotational saddle to solid body rotation.

Case (b): The Case of Zero Vorticity

We now consider the case for which all three vorticity components vanish, i.e. $\xi = \eta = \zeta = 0$. Without loss of generality the coordinate system is aligned such that the streamlines lie in the xy plane. Proceeding as before, we obtain the elements of the coefficient matrix in eqn. (1.23) :

$$\begin{matrix} \pm\sqrt{-P_{xx} - f_1^2} & f_1 & 0 \\ f_1 & \pm\sqrt{-P_{yy} - f_1^2} & 0 \\ 0 & 0 & \pm\sqrt{-P_{zz}} \end{matrix} .$$

The constant f_1 is arbitrary and determines the orientation of the flow pattern in the xy plane. It can be adjusted, without loss of generality, to be zero. It turns out, that we have a pressure maximum at the critical point.

With the above coefficients, we get the solutions shown in Fig. 1.9 for the flow in the xy plane. Solutions for all three coordinate planes lie in the hashed area given in the p-q diagram at the top of the figure. The critical points in the other coordinate planes are saddles. These flow patterns are then referred to as saddle-node combinations or saddle-node trios.

Such solutions have been used for describing certain aspects of vortex structures in jets and wakes.

1.4 Topological Rule

For a simply connected isolated three-dimensional body, as the topological equivalent of a sphere, from continuity considerations the number of nodes, N, (including foci) must exceed the number of saddles, S, by two in the wall streamline field :

$$\Sigma N = \Sigma S + 2 \qquad (1.26)$$

Details are given by J.C.R.Hunt et al [22]. These authors have shown that these notions of critical points and topological rules can be extended to the flow above the surface on symmetry planes, crossflow planes, and others. For a simply connected body continuity requires for the sectional flow that the number of saddles, S, exceeds the number of nodes, N, (including foci, F) by one :

$$\Sigma S = \Sigma N + 1 \qquad (1.27)$$

APPENDIX II

Synthesis of Steady, Inviscid, Irrotational, Incompressible Flows

The following simple, inviscid, irrotational, incompressible flows can be superimposed to give more general flows :

- Uniform flow
- Source and sink flows
- Vortex flow .

The above flows satisfy continuity and, therefore, are physically possible.

II.1 Governing Equations and Boundary Conditions

II.1.1 Governing Equations

For two- and three-dimensional flows, which satisfy continuity and irrotationality, we have :

- Continuity equation for incompressible flow with velocity $\vec{V}$:

$$\text{div } \vec{V} = 0 \qquad \text{(II.1)}$$

In two-dimensional flow it is identically satisfied by the existence of a stream function, ψ. The equations for the velocity components in two-dimensional, incompressible flow are :

$$u = \frac{\partial \psi}{\partial y} \quad \text{and} \quad v = -\frac{\partial \psi}{\partial x} \qquad \text{(II.2)}$$

Irrotationality of compressible or incompressible flow is expressed by:

$$\text{Curl } \vec{V} = 0 \quad . \tag{II.3}$$

This irrotationality equation is identically satisfied by the existence of a velocity potential, φ.

The equations for the velocity components in a two-dimensional, irrotational flow are :

$$u = \frac{\partial \varphi}{\partial x} \quad \text{and} \quad v = \frac{\partial \varphi}{\partial y} \quad . \tag{II.4}$$

Substituting (II.4) into equation (II.1) and (II.2) into (II.3), we get

$$\nabla^2 \varphi = 0 \quad , \tag{II.5}$$

the continuity equation for two-(and three-)dimensional incompressible, irrotational flow, and

$$\nabla^2 \psi = 0 \quad , \tag{II.6}$$

the irrotationality equation for two-dimensional, incompressible flow, with the continuity equation fulfilled.

Each of the last two equations describes the same kind of flow, i.e. two-dimensional, incompressible, irrotational flow.

II.1.2 Boundary Conditions

In addition to the equations (II.5) and (II.6), boundary conditions are needed in order to choose the particular solution of the problem under consideration.

For a body submerged in a uniform free stream with velocity V_∞, it is required that :

- The surface of the body is a streamsurface, i.e, for a two-dimensional flow in a xy plane the contour of the body is a streamline:

$$\psi = \text{const or } \frac{\partial \varphi}{\partial n} = 0 \quad , \tag{II.7a}$$

with n normal direction to surface.

- At large distance from the body in two-dimensional flow :

$$u = \frac{\partial \varphi}{\partial x} = \frac{\partial \psi}{\partial y} = V_\infty$$

and (II.7b)

$$v = \frac{\partial \varphi}{\partial y} = - \frac{\partial \psi}{\partial x} = 0 \ .$$

The flow is sketched in Fig. II.1.

A solution of the Laplace equation (II.5) or (II.6), which satisfies the boundary conditions at a given body and at infinity, and with the magnitude of the circulation around the body specified, is a unique solution. This particular solution describes the two-dimensional, incompressible, inviscid, irrotational flow field around a given body.

Such solutions, i.e. two-dimensional, incompressible, inviscid, irrotational flows, are :

Table II.1

FLOW	ψ	φ
Vortex	$(\frac{\Gamma}{2\pi})$ ln r	$-(\frac{\Gamma}{2\pi})\,\theta$
Source	$(\frac{\Lambda}{2\pi})\,\theta$	$(\frac{\Lambda}{2\pi})$ ln r
Uniform flow in x-direction	V_∞ y	V_∞ x

The flow patterns and coordinates used are sketched in Fig. II.2.

II.2 Superposition of Flows

II.2.1 General Procedure

The Laplace equations :

$$\nabla^2 \psi = 0 \quad \text{and} \quad \nabla^2 \varphi = 0$$

are linear.

Therefore, if $\psi_1, \psi_2, \psi_3, \text{----}, \psi_n$ are solutions of $\nabla^2 \psi = 0$, the sum of these solutions :

$$\psi = \psi_1 + \psi_2 + \psi_3 + \text{-----} + \psi_n$$

is also a solution of the Laplace equation, i.e. it is also a two-dimensional, incompressible, irrotational flow.

The resulting flow, ψ, is automatically satisfying the boundary conditions at the body and at infinity, given by summing those of the component flows, ψ_1, ψ_2, ψ_3, ----, ψ_n.

The Laplace equation for φ is also linear, therefore,

$$\varphi = \varphi_1 + \varphi_2 + \varphi_3 + \text{-----} + \varphi_n \ .$$

The governing equations are also linear :

$$\text{div } \vec{V} = 0 \quad \text{and} \quad \text{Curl } \vec{V} = 0 \ .$$

Solutions $\vec{V}_i$ can be summed to give a new solution $\vec{V}$ of the governing equations :

$$\vec{V} = \vec{V}_1 + \vec{V}_2 + \vec{V}_3 + \text{-----} + \vec{V}_n \ .$$

The pressures, p, of the component flows cannot be superimposed, because they are nonlinear functions of the velocity, V.

II.2.2 Superposition of Straight Two-Dimensional Vortices Near a Solid Boundary .

We consider the superposition of the steady, incompressible, inviscid, irrotational flows of the straight, two-dimensional vortices shown in Fig. 3.12, which are arranged parallel to a solid, flat plate of infinite extent and to the symmetry plane. The boundary condition imposed by the solid wall is satisfied by image vortices of same strength and opposite sense on the other side of the plate.

The resultant flow at an arbitrary point P(x,y) in a plane z = constant is given by addition of the stream functions ψ_i of the actual vortices and $\bar{\psi}_i$ of the image vortices :

$$\psi_R(x,y) = \psi_1 + \bar{\psi}_1 + \psi_2 + \bar{\psi}_2 + \psi_3 + \bar{\psi}_3 + \psi_4 + \bar{\psi}_4 + \psi_5 + \bar{\psi}_5 + \psi_6 + \bar{\psi}_6 .$$

With stream function, ψ, as given in Table II.1, we get :

$$\psi_R(x,y) = -\frac{\Gamma_1}{2\pi}\ln r_1 + \frac{\Gamma_1}{2\pi}\ln\bar{r}_1 + \frac{\Gamma_2}{2\pi}\ln r_2 - \frac{\Gamma_2}{2\pi}\ln\bar{r}_2 - \frac{\Gamma_3}{2\pi}\ln r_3 + \frac{\Gamma_3}{2\pi}\ln\bar{r}_3 + \frac{\Gamma_4}{2\pi}\ln r_4 - \frac{\Gamma_4}{2\pi}\ln\bar{r}_4 - \frac{\Gamma_5}{2\pi}\ln r_5 + \frac{\Gamma_5}{2\pi}\ln\bar{r}_5 + \frac{\Gamma_6}{2\pi}\ln r_6 - \frac{\Gamma_6}{2\pi}\ln\bar{r}_6$$

$$= \frac{\Gamma_1}{2\pi}\ln\left(\frac{\bar{r}_1}{r_1}\right) + \frac{\Gamma_2}{2\pi}\ln\left(\frac{r_2}{\bar{r}_2}\right) + \frac{\Gamma_3}{2\pi}\ln\left(\frac{\bar{r}_3}{r_3}\right) + \frac{\Gamma_4}{2\pi}\ln\left(\frac{r_4}{\bar{r}_4}\right) + \frac{\Gamma_5}{2\pi}\ln\left(\frac{\bar{r}_5}{r_5}\right) + \frac{\Gamma_6}{2\pi}\ln\left(\frac{r_6}{\bar{r}_6}\right) ,$$

where :

$$r_1 = \sqrt{(a_1 - x)^2 + (b_1 - y)^2} \quad , \quad \bar{r}_1 = \sqrt{(a_1 - x)^2 + (b_1 + y)^2}$$

$$r_2 = \sqrt{(a_2 + x)^2 + (b_2 - y)^2} \quad , \quad \bar{r}_2 = \sqrt{(a_2 + x)^2 + (b_2 + y)^2}$$

$$r_3 = \sqrt{(a_3 + x)^2 + (b_3 - y)^2} \quad , \quad \bar{r}_3 = \sqrt{(a_3 + x)^2 + (b_3 + y)^2}$$

$$r_4 = \sqrt{(a_4 + x)^2 + (b_4 - y)^2} \quad , \quad \bar{r}_4 = \sqrt{(a_4 + x)^2 + (b_4 + y)^2}$$

$$r_5 = \sqrt{(a_5 + x)^2 + (b_5 - y)^2} \quad , \quad \bar{r}_5 = \sqrt{(a_5 + x)^2 + (b_5 + y)^2}$$

$$r_6 = \sqrt{(a_6 + x)^2 + (b_6 - y)^2} \quad , \quad \bar{r}_6 = \sqrt{(a_6 + x)^2 + (b_6 + y)^2} \; .$$

Then :

$$\psi_R (x,y) = \frac{1}{4\pi} *$$

$$[\, \Gamma_1 \ln \{\frac{(a_1 - x)^2 + (b_1 + y)^2}{(a_1 - x)^2 + (b_1 - y)^2}\} + \Gamma_2 \ln \{\frac{(a_2 + x)^2 + (b_2 - y)^2}{(a_2 + x)^2 + (b_2 + y)^2}\}$$

$$+ \Gamma_3 \ln \{\frac{(a_3 + x)^2 + (b_3 + y)^2}{(a_3 + x)^2 + (b_3 - y)^2}\} + \Gamma_4 \ln \{\frac{(a_4 + x)^2 + (b_4 - y)^2}{(a_4 + x)^2 + (b_4 + y)^2}\}$$

$$+ \Gamma_5 \ln \{\frac{(a_5 + x)^2 + (b_5 + y)^2}{(a_5 + x)^2 + (b_5 - y)^2}\} + \Gamma_6 \ln \{\frac{(a_6 + x)^2 + (b_6 - y)^2}{(a_6 + x)^2 + (b_6 + y)^2}\} \,] \; .$$

In Fig. 3.13 can be seen, as an example, a result of the foregoing calculation of the stream function ψ_R. Presented are the streamlines (i.e. lines ψ_R = constant) of the flow, resulting from a typical vortex configuration, as was conjectured from flow visualizations. The image vortices used are not shown.

The locations of the vortices are given by the following distances, a_i and b_i, from origin O in x- and y- direction, respectively :

$$a_1 = 2.75 \text{ cm} \quad , \qquad a_2 = a_3 = 2.75 \text{ cm}$$

$$a_4 = 19.25 \text{ cm} \quad , \qquad a_5 = a_6 = 13.75 \text{ cm}$$

$$b_1 = b_4 = 5.00 \text{ cm}, \quad b_2 = b_5 = 4.00 \text{ cm}$$

$$b_3 = b_6 = 2.5 \text{ cm}.$$

The values of the strengths of the vortices, Γ_i, are given in the legend of the figure.

II.2.3 Superposition of Straight Two-Dimensional Vortices and Uniform Flow in the Symmetry Plane

Analogous to the foregoing superposition of vortex flows, we now superimpose the flows of two straight, two-dimensional vortices, which are parallel to the leading edge, and a uniform flow, V_∞, parallel to the plate and normal to the leading edge (in negative z-direction), satisfying boundary conditions at the solid wall of the plate by image vortices as before, see Fig. 3.14. The resulting flow at an arbitrary point, Q(z,y), in the symmetry plane is given by :

$$\psi_R(z,y) = \psi_3 + \bar{\psi}_3 + \psi_7 + \bar{\psi}_7 + \psi_\infty .$$

With the stream functions of vortices and of uniform flow given in Table II.1, we get :

$$\psi_R(z,y) = -\frac{\Gamma_3}{2\pi} \ln r_3 + \frac{\Gamma_3}{2\pi} \ln \bar{r}_3 + \frac{\Gamma_7}{2\pi} \ln r_7 - \frac{\Gamma_7}{2\pi} \ln \bar{r}_7 - V_\infty y$$

$$= \frac{\Gamma_3}{2\pi} \ln\left(\frac{\bar{r}_3}{r_3}\right) + \frac{\Gamma_7}{2\pi} \ln\left(\frac{r_7}{\bar{r}_7}\right) - V_\infty y .$$

With :

$$r_3 = \sqrt{(c_3 + z)^2 + (b_3 - y)^2} \quad , \quad \bar{r}_3 = \sqrt{(c_3 + z)^2 + (b_3 + y)^2}$$

$$r_7 = \sqrt{(c_7 - z)^2 + (b_7 - y)^2} \quad , \quad \bar{r}_7 = \sqrt{(c_7 - z)^2 + (b_7 + y)^2} \; .$$

We finally have :

$$\psi_R\,(z,y) = \frac{1}{4\pi}\,[\,\Gamma_3 \ln\{\frac{(c_3 + z)^2 + (b_3 + y)^2}{(c_3 + z)^2 + (b_3 - y)^2}\}$$

$$+ \Gamma_7 \ln\{\frac{(c_7 - z)^2 + (b_7 - y)^2}{(c_7 - z)^2 + (b_7 + y)^2}\}\,] - V_\infty\, y \; .$$

A result of the foregoing calculation of the stream function ψ_R, in the symmetry plane, can be seen in Fig. 3.15.

The locations of the vortices are given by the following distances, c_i and b_i, from origin,O, in z- and y- direction, respectively :

$$c_3 = 3.55 \text{ cm} \quad , \quad c_7 = 3.55 \text{ cm}$$

$$b_3 = 2.50 \text{ cm} \quad , \quad b_7 = 1.00 \text{ cm}$$

The values of the strengths of the vortices, Γ_i, and the uniform-flow velocity, V_∞, are given in the legend of the figure.

APPENDIX III

Electromagnetic Analogy

III.1 General Background

The electromagnetic analogy is based on the fact that the magnetic field generated by a current in a wire, is described by the same functional relationship (Biot-Savart law) as is the velocity field around a vortex filament in an inviscid, incompressible fluid.

A straight, infinitely long vortex filament of strength, Γ, induces the tangential velocity, U_θ, at distance r in a plane normal to the filament, which is given by:

$$U_\theta = \frac{\Gamma}{2\pi r} \quad . \tag{III.1}$$

The vortex flow is shown in Fig. III.1a.

Around a straight, infinitely long wire carrying a current, I, there exists a magnetic field of strength, H, at a distance r, in a plane normal to the wire, which is given by:

$$H = \frac{I}{2\pi r} \quad . \tag{III.2}$$

The magnetic field is shown in Fig. III.1b.

Comparing equations III.1 and III.2, it can be seen that H and I corresponds to U_θ and Γ, respectively, i.e. the magnetic field lines correspond to the streamlines of the vortex flow.

Uniform flow can be simulated by the uniform magnetic field inside a relatively long cylindrical coil carrying a current of strength I (see Fig. III.1c). The strength of the magnetic field, H, inside the cylindrical coil is given by:

$$H = \frac{I.N}{L} \quad , \qquad \text{(III.3)}$$

with N number of windings and L length of coil.

In order to satisfy boundary conditions on the surface of the plate, the method of images is used.

However, this electromagnetic analogy cannot in practice, represent the unsteadiness of the flow fields observed, in which vortex filaments change position and direction with time, as well as probably strength, whereas wires and currents are fixed in a test.

The electromagnetic analogy also holds, as can be shown, for cases of more general, curved vortex filaments.

III.2 Strength of Current in Vortex-Wires

III.2.1 Configuration of Experiment 7

The current distribution in the vortex-wires (without leading-edge vortex-wire) is given below for an output of the power supply unit of I=110 amps at V=3.8 volts. The designation of the wires corresponds to the arrangement as seen in Fig. 3.9.

	Vortex-Wire	Current, amps
1.	Bottom Symmetry-Plane	34.00
2.	Top Symmetry-Plane	37.00
3.	Forward Focal	11.00
4.	Backward Focal	11.50
5.	Forward Side-Edge	8.00
6.	Backward Side-Edge	8.00
7.	Coil	0.25
	Total	109.75

III.2.2 Configuration of Experiment 8

The current distribution in the vortex-wires, with leading-edge vortex-wire, is given below for an output of the power supply unit of I=110 amps at V=4.5 volts. The designation of the wires corresponds to the arrangement as seen in Fig. 3.10.

	Vortex-Wire	Current, amps
1.	Bottom Symmetry-Plane	26.50
2.	Top Symmetry-Plane	31.00
3.	Forward Focal	13.50
4.	Backward Focal	14.00
5.	Forward Side-Edge	7.00
6.	Backward Side-Edge	7.00
7.	Upper Leading-Edge	5.50
8.	Lower Leading-Edge	5.50
9.	Coil	0.30
	Total	110.30

The currents in the wires, representing a vortex and its image vortex, should be the same. In the above tables there is a difference of 12% in currents for the symmetry-plane vortex-wires. This might be due to a manufacturing defect, i.e. a structural defect, or the wires were not of equal diameters.

NOTATION

a,b,c	distances from origin (see figures 3.12 & 3.14)
a_∞	free-stream speed of sound
A	aspect ratio, $\frac{B^2}{F}$
B	span
c_Z	normal-force coefficient, $c_Z = \frac{Z}{q_\infty F}$
C	chord, also denotes centre
d	diameter of cylinder
D	determinant
e,f,g	elements of the matrix (see equations 1.18 & 1.23)
F	planform area, also denotes focus
H	magnetic field strength
I	current
L	length of coil
M_∞	free-stream Mach number, $M_\infty = \frac{V_\infty}{a_\infty}$
N	number of windings, also denotes node
p	pressure
P	kinematic pressure, $P = \frac{p}{\rho}$
q_∞	free-stream dynamic pressure, $q_\infty = \frac{1}{2} \rho_\infty V_\infty^2$
r	radial distance
Re_c	Reynolds number, $Re_c = \frac{V_\infty . C}{\nu_\infty}$
S	saddle
t	time
u,v,w	cartesian velocity components

U_r	radial velocity
U_θ	tangential velocity
V_∞	free-stream velocity
$\vec{V}$	velocity vector
x,y,z	cartesian coordinates
$\vec{x}$	position vector
$\dot{\vec{x}}$	velocity vector
x_1,x_2,x_3	cartesian coordinates
$\dot{x}_1,\dot{x}_2,\dot{x}_3$	cartesian velocity components
Z	normal force

α	angle of incidence
θ	angle between s and y coordinates (see Fig. 1.5)
λ	eigenvalue
ψ	stream function
$\bar{\psi}$	stream function for image vortex
φ	velocity potential
Γ	vortex strength
Λ	source strength
ρ	density
ν	kinematic viscosity
ξ,η,ζ	cartesian components of vorticity
$\vec{\Omega}$	vorticity vector

Subscripts:

crit	critical value
∞	free-stream condition
l	lower value } see Fig. 1.3
u	upper value } see Fig. 1.3
R	resultant
x,y,z	denote partial differentiation

Superscripts:

$\cdot$	denotes differentiation with time
$\sim$	denotes values at critical point

Abbreviations:

L.E.	leading edge
S.E.	side edge
T.E.	trailing edge

REFERENCES

[1] Dines,W.H.: "On Wind Pressure upon an Inclined Surface", Proc. Roy. Soc., London, Vol. 48, 1890, pp. 233-257.

[2] Hoerner,S.F.: "Drag of Various Types of Plates", in Fluid Dynamic Drag, 2nd Edition, Published by Author, New York, 1965, pp. 3-16.

[3] Ahlborn,F.:"Hydrodynamische Experimentaluntersuchungen", Jb. Schiffbautechn. Ges., Vol. 5, 1904, pp. 417-447.

[4] Ahlborn,F.: "Die Wirbelbildung im Widerstandsmechanismus des Wassers", Jb. Schiffbautechn. Ges., Vol. 6, 1905, pp. 67-81.

[5] Ahlborn,F.: "Die Widerstandsvorgaenge im Wasser an Platten und Schiffskoerpern. Die Entstehung der Wellen", Jb. Schiffbautechn. Ges., Vol. 10, 1909, pp.370-431.

[6] Prandtl,L.: "Einige fuer die Flugtechnik wichtige Beziehungen aus der Mechanik. Etwas ueber den Luftwiderstand", Z. Flugtechnik Motorluftschiffahrt, Vol. 1, 1910, pp. 3-6, 25-30, 61-64, 73-76.

[7] Goldstein,S.(Editor): Modern Developments in Fluid Dynamics, Vol. II, Clarendon Press, Oxford, 1938, and Dover Publ., New York, 1965, pp. 577-579.

[8] Stanton,T.E. and Marshall,D.: "On the Eddy System in the Wake of Flat Circular Plates in Three-Dimensional Flow", ARC, R.M. 1358, 1932, also Proc. Roy. Soc. A, Vol. 130, 1931, pp. 295-301.

[9] Simmons,L.F.G. and Dewey,N.S.: "Wind Tunnel Experiments

with Circular Discs", ARC, R.M. 1334, 1931.

[10] Winter, H.: "Stroemungsvorgaenge an Platten und Profilierten Koerpern bei kleinen Spannweiten", Forsch. Ing.-Wes., Vol. 6, 1935, pp. 40-50 and 67-71.

[11] Perry,A.E.,Lim,T.T., and Chong,M.S.: "The Instantaneous Velocity Fields of Coherent Structures in Coflowing Jets and Wakes", J. Fluid Mech., Vol. 101, 1980, pp. 243-256.

[12] Tobak,M. and Peake,D.J.: "Topology of Three-Dimensional Separated Flows", Ann. Rev. Fluid Mech., Vol. 14, 1982, pp. 61-85.

[13] Hornung,H.G. and Perry,A.E.: "Some Aspects of Three-Dimensional Separation. Part I. Streamsurface Bifurcations", Z. Flugwiss. Weltraumforsch., Vol. 8, 1984, pp. 77-87.

[14] Hornung,H.G.: "The Vortex Skeleton Model for Three-Dimensional Steady Flows", AGARD-CP-342, 1983, pp. 2-1 to 2-12.

[15] Dallmann,U.: "Topological Structures of Three-Dimensional Vortex Flow Separation", AIAA 16th Fluid and Plasma Dynamics Conference, 1983, Danvers, MA., AIAA paper 83-1735, 1983.

[16] Van Westerhoven, P., Wedemeyer, E., and Wendt, J. F.: "Low Aspect Ratio Rectangular Wings at High Incidences", in Missile Aerodynamics, AGARD-CPP-336, 1982, pp. 15-1 to 15-14.

[17] Earnshaw,P. B. and Lawford,J. A.: "Low-Speed Wind-Tunnel Experiments on a Series of Sharp-Edged Delta Wings, Part I", R.A.E., T.N. Aero. 2780, 1961.

[18] Stahl,W. H. and Mahmood,M.: "Some Aspects of the Flow Past a Square Flat Plate at High Incidence", Z. Flugwiss. Weltraumforsch., Vol. 9, 1985, pp. 134-142.

[19] Abu Saleh,M.K.: "Experiments on a Flat Square Plate at High Angles of Attack", M.S. Thesis Dissertation, K.F.U.P.M, Dhahran, Saudi Arabia, 1987.

[20] Hornung,H. and Perry,A.E.: "Streamsurface Bifurcation, Vortex Skeletons, and Separation", DFVLR-IB 222-82 A 25, 1982.

[21] Fairlie,B.D.: "Flow Separation on Bodies of Revolution at Incidence", 7th Australasian Hydraulics and Fluid Mechanics Conference, Brisbane, Australia, Aug. 1980.

[22] Hunt,J.C.R., Abell,C.J., Peterka,J.A., and Woo,H.: "Kinematical Studies of the Flows around Free or Surface Mounted Obstacles, Applying Topology to Flow Visualization", J. Fluid Mech., Vol. 86, 1978, pp. 179-200.

[23] Perry,A.E.: "A Study of Degenerate and Nondegenerate Critical Points in Three-Dimensional Flow Fields", DFVLR-FB 84-36, 1984.

[24] Perry,A.E. and Fairlie,B.D.: "Critical Points in Flow Patterns", Advances in Geophysics, Vol. 18 B, 1974, pp. 299-315.

[25] Perry,A.E. and Hornung,H.G.: "Some Aspects of Three-Dimensional Separation. Part II. Vortex Skeletons", Z. Flugwiss. Weltraumforsch., Vol. 8, 1984, pp. 155-160.

[26] Jordan,D.W. and Smith,P.: Nonlinear Ordinary Differential Equations, 2nd Edition, Clarendon Press, Oxford, 1987.

[27] Lim,T.T., Chong,M.S., and Perry,A.E.: "The Viscous Tornado", Proc., 7th Australasian Hydraulics and Fluid Mechanics Conference, Brisbane, Australia, 1980, pp. 250-253.

[28] Perry,A.E. and Steiner,T.R.: "Large-Scale Vortex Structures in Turbulent Wakes behind Bluff Bodies. Part I. Vortex Formation Processes", J. Fluid Mech., Vol. 174, 1987, pp. 233-270.

[29] Steiner,T.R. and Perry,A.E.: "Large-Scale Vortex Structures in Turbulent Wakes behind Bluff Bodies. Part 2. Far-Wake Structures", J. Fluid Mech., Vol. 174, 1987, pp. 271-298.

[30] Kaplan,W.: Ordinary Differential Equations, Pergamon, Oxford, 1958.

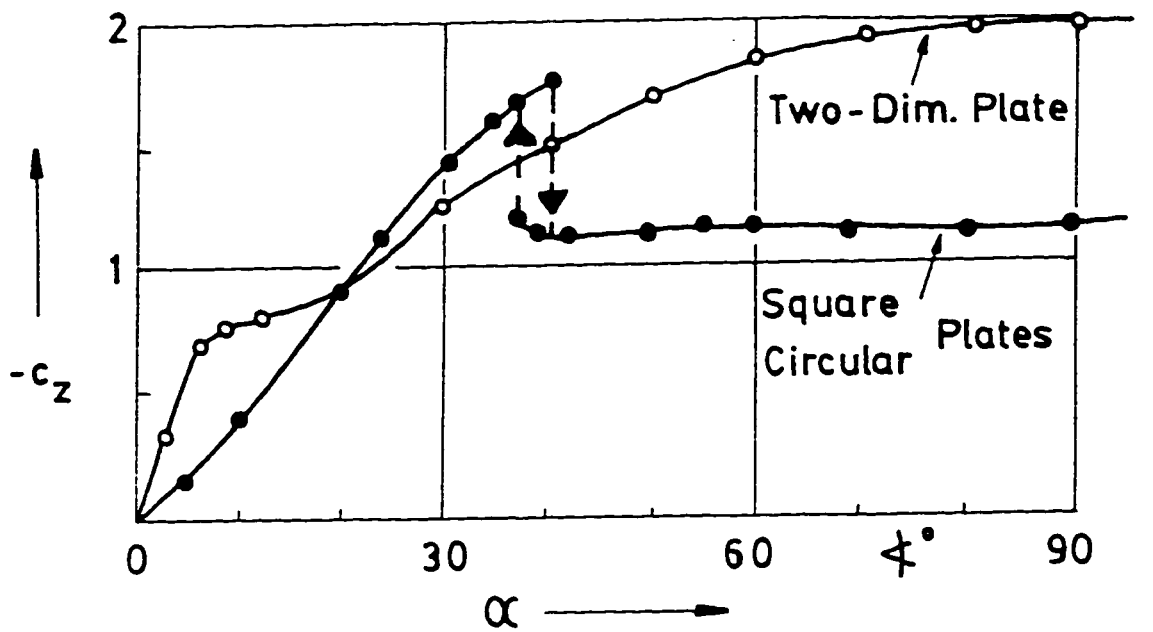

Fig. 1.1 Normal-Force Coefficient vs Incidence for Two-Dimensional, Circular, and Square Plates, from S.F.Hoerner [2].

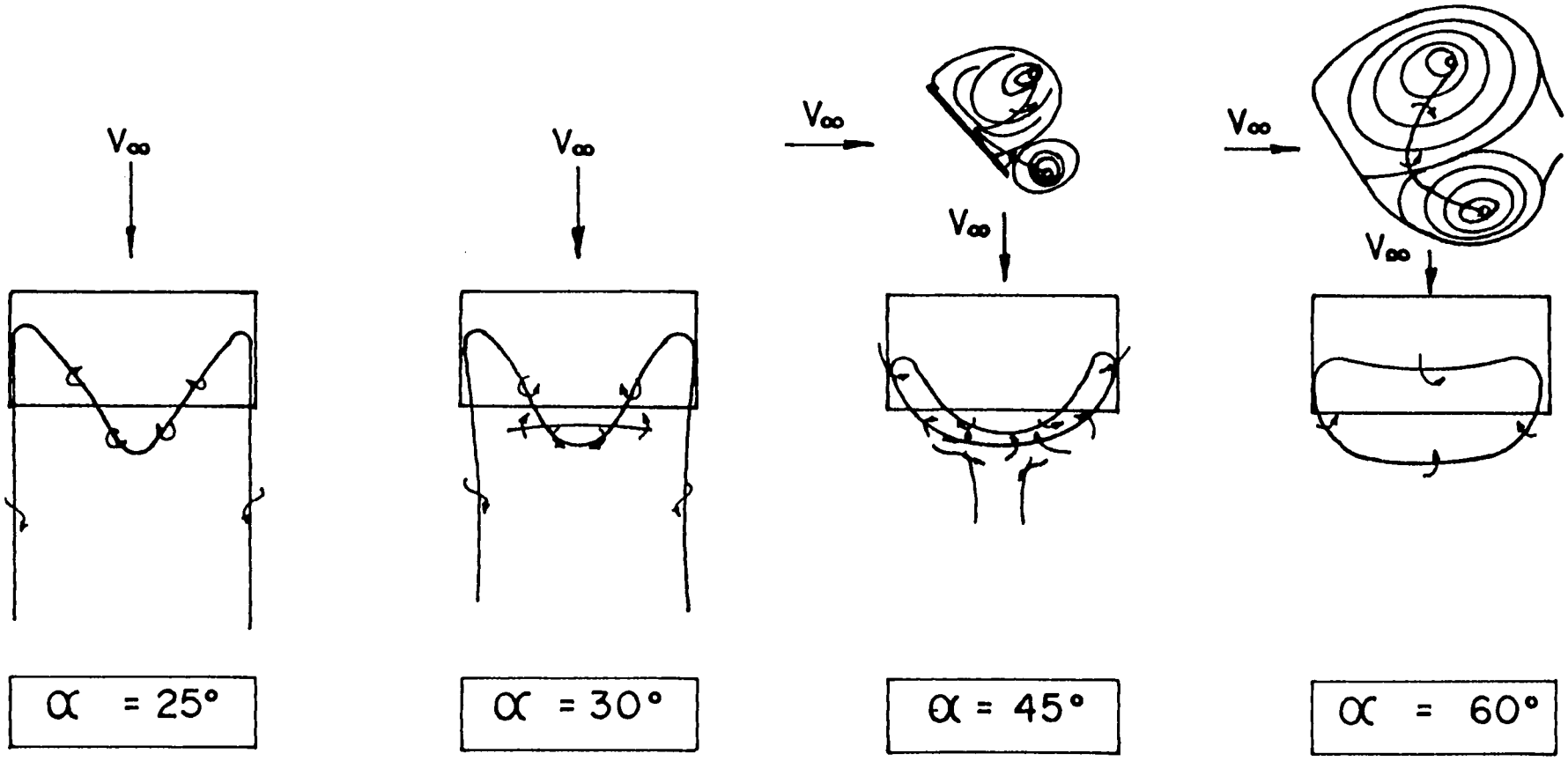

Fig. I.2: Vortex Patterns of Rectangular Plate, A = 2, at Various Incidences According to F. Ahlborn [5]

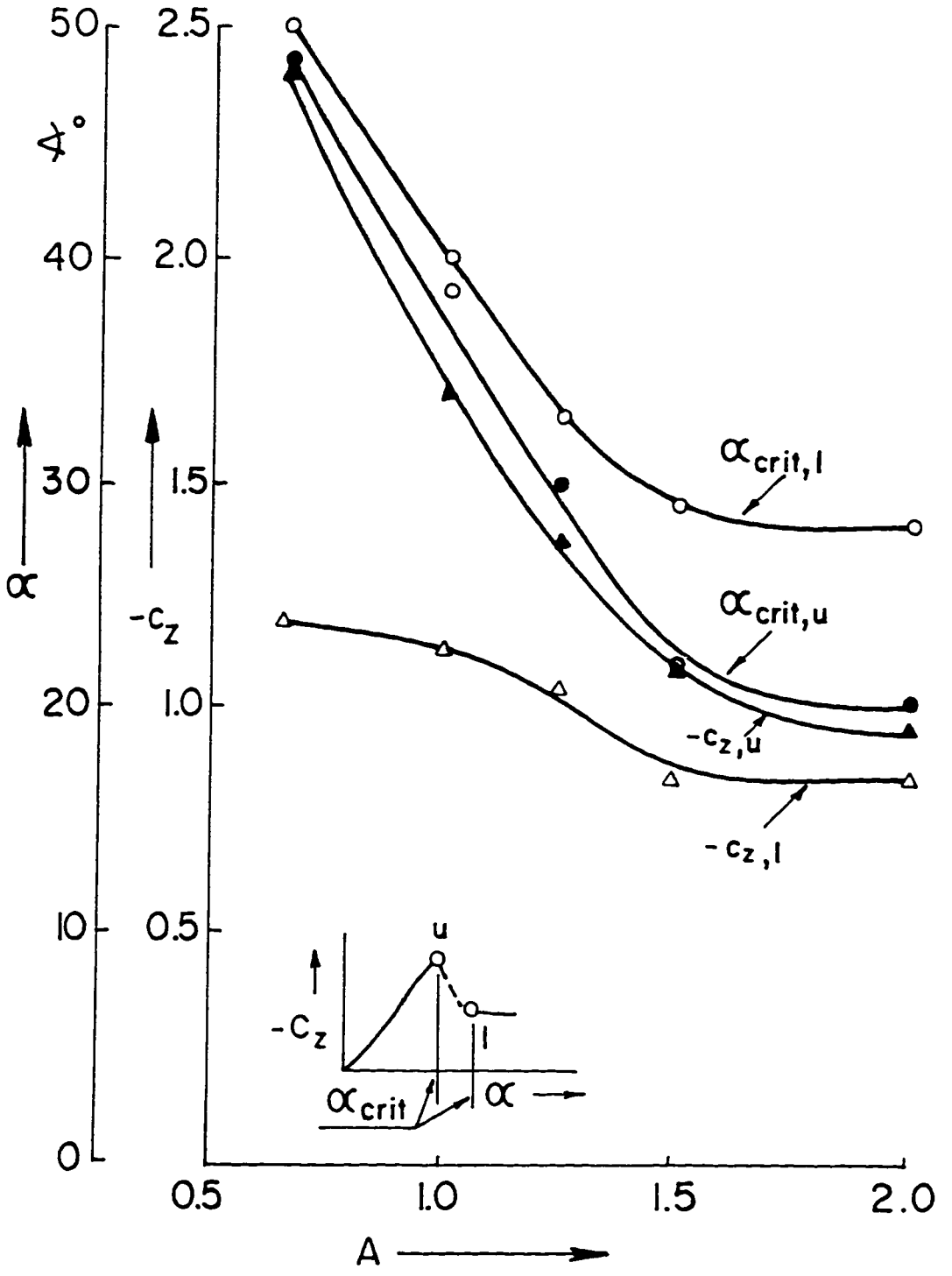

Fig. 1.3: Critical Angles of Incidence and Resp. Normal-Force Coefficients for Rectangular Plates of Various Aspect Ratios, from H. Winter [10]

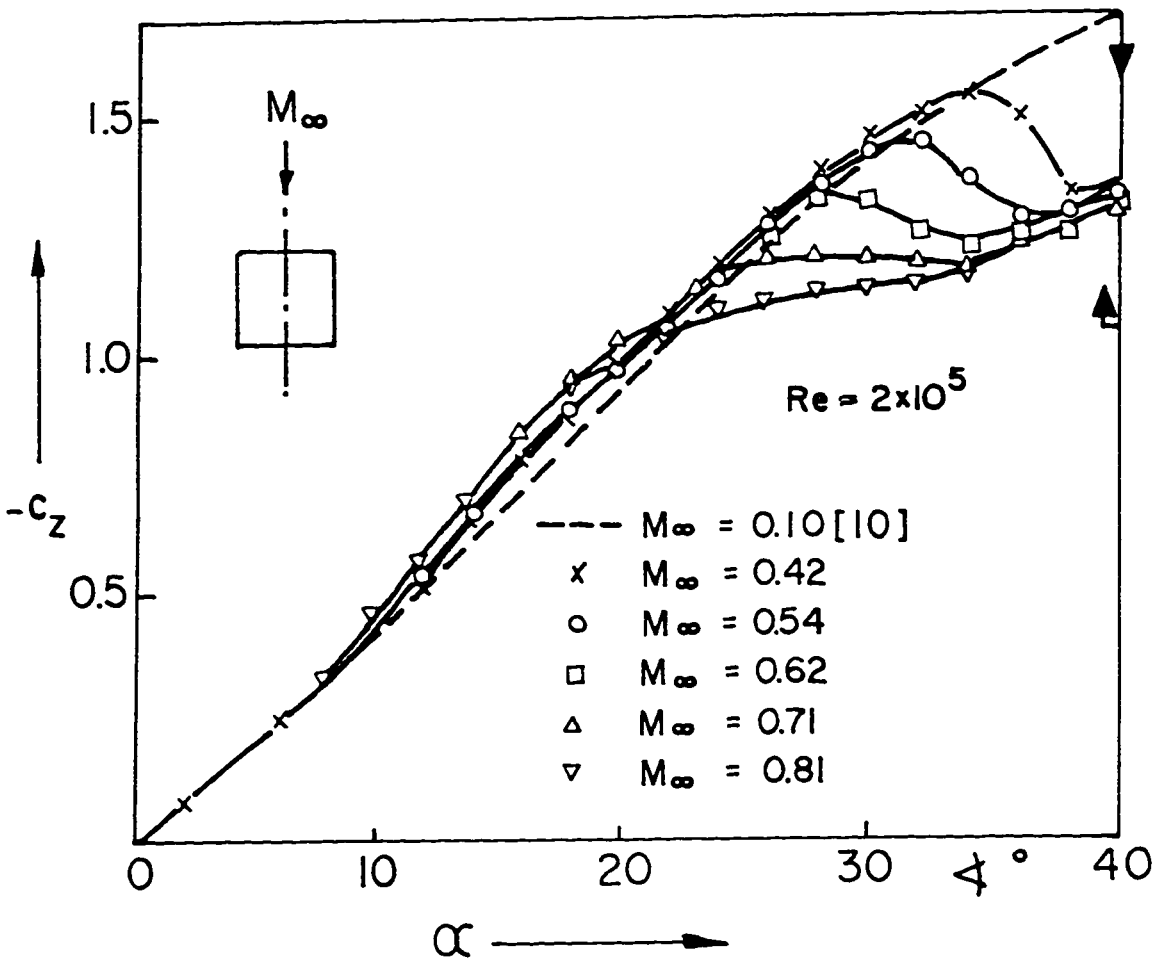

Fig. 1.4: Normal-Force Coefficient vs Incidence for Square Plate at Various Mach Numbers from P. Van Westerhoven et al [16]

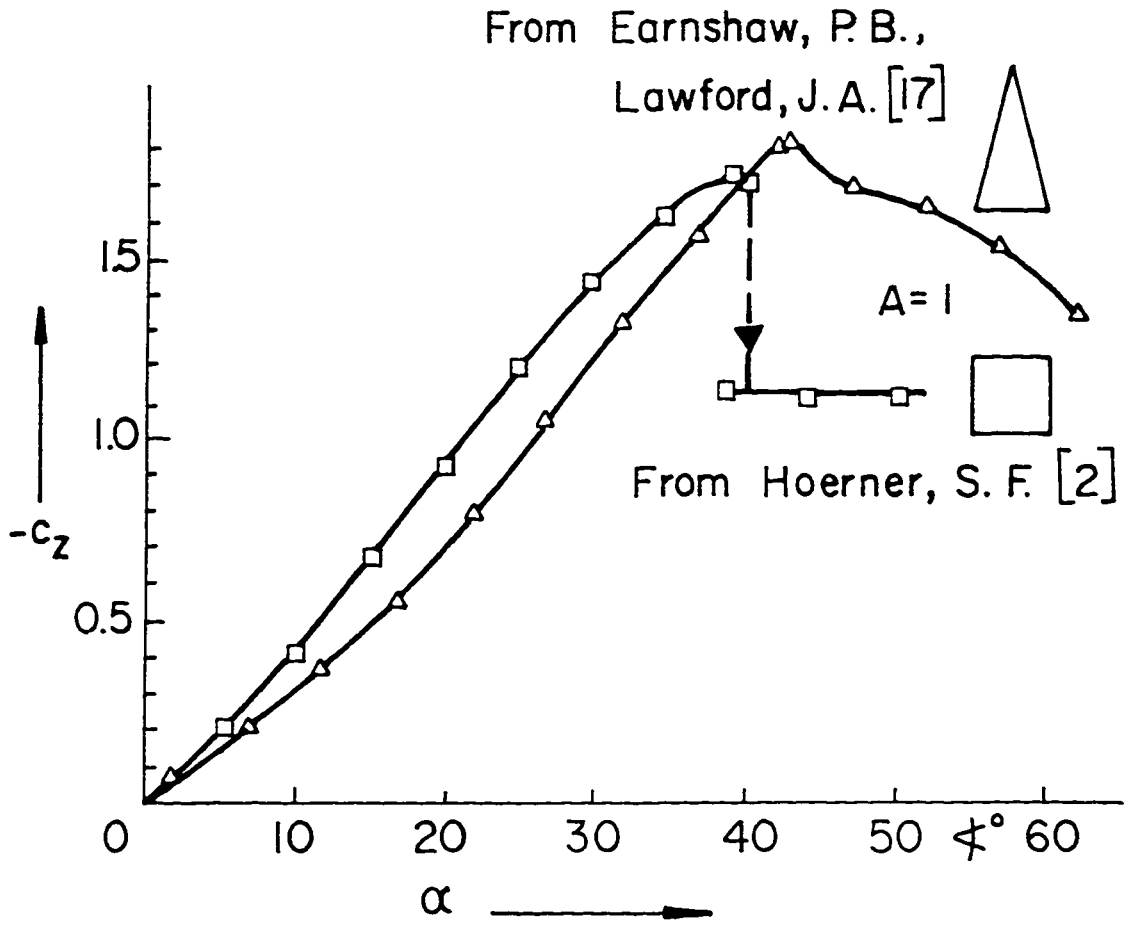

Fig. 1.5: Normal-Force Coefficient vs Incidence for Delta and Rectangular Wings of Small Aspect Ratio (A=1)

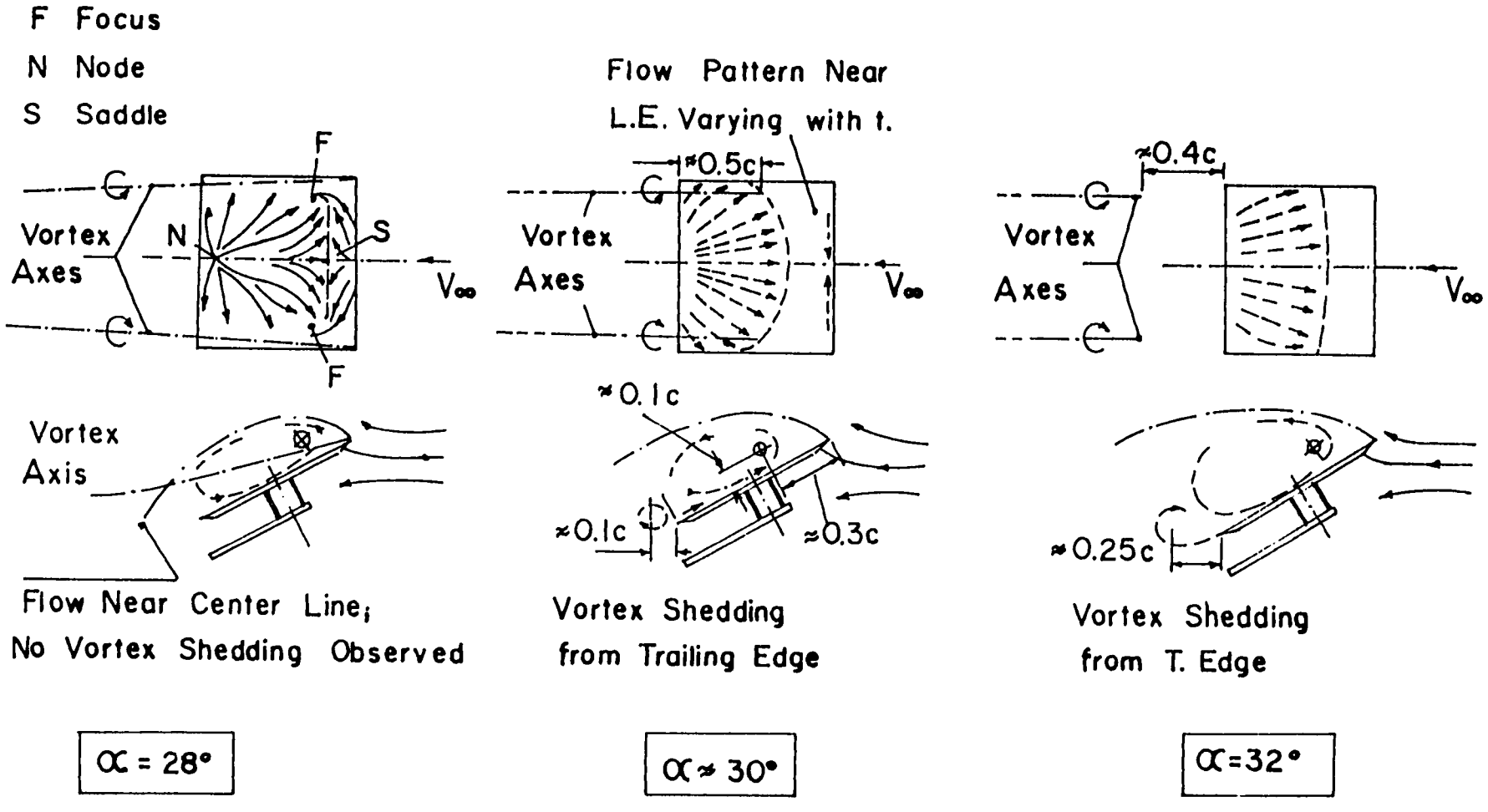

Fig. 1.6a: Flow Patterns for Square Plate at Various Incidences at $Re_c = 1.1 \times 10^5$, from W.H.Stahl and M.Mahmood [18].

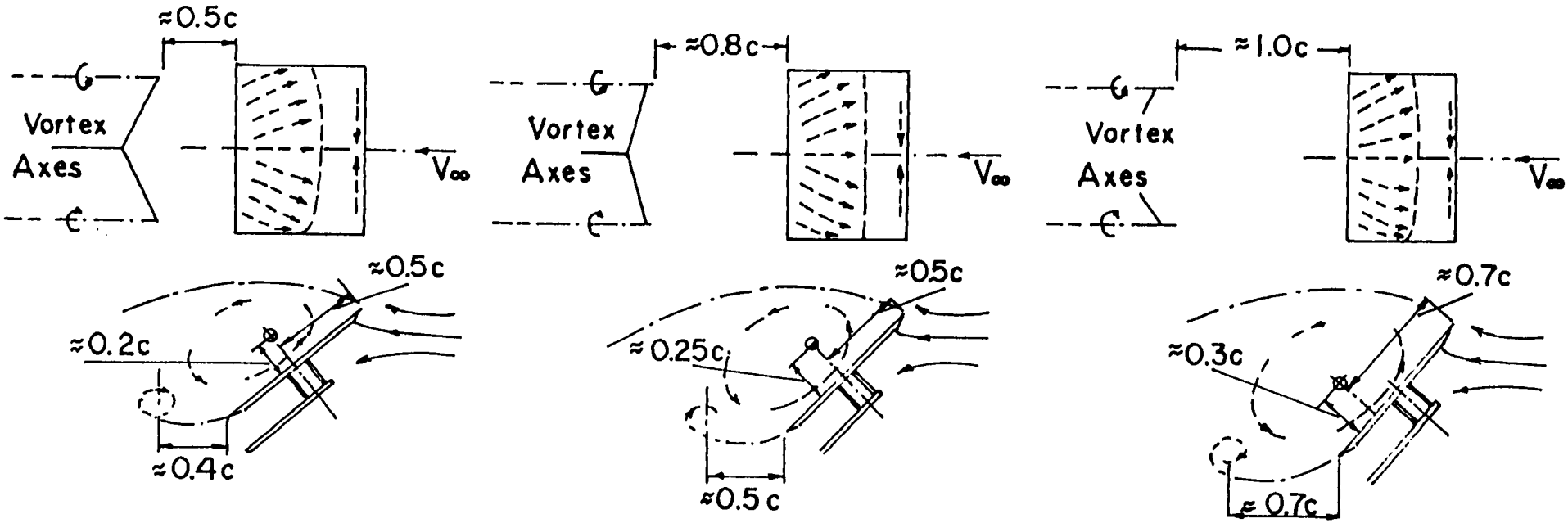

Fig. 1.6 b: Flow Patterns for Square Plate at Various Incidences at $Re_c = 1.1 \times 10^5$, from W.H. Stahl and M. Mahmood [18].

$$\alpha_{Crit} \approx 30^\circ \text{ Independent of } Re_c$$

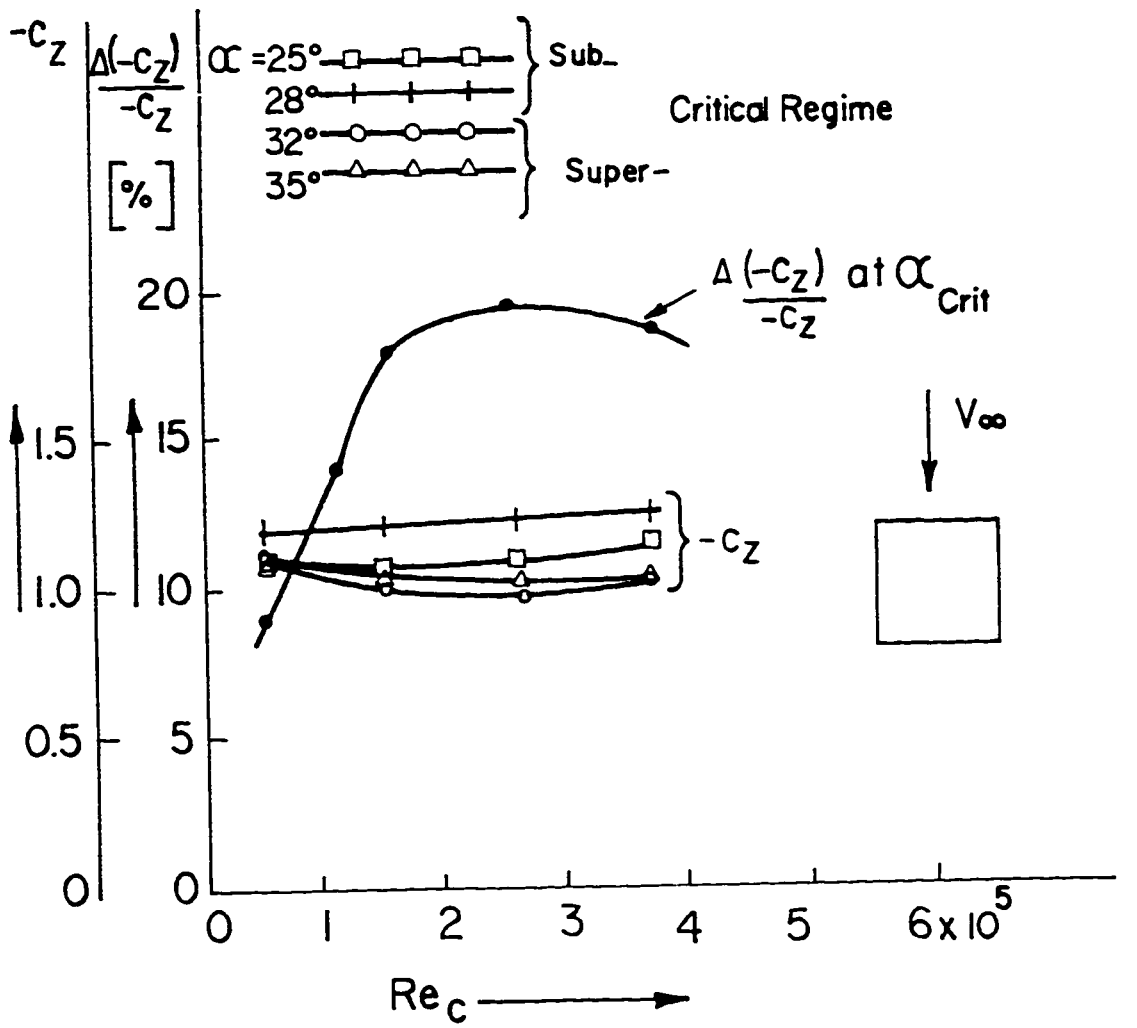

Fig. 1.7: Normal-Force Coefficient and Percentage Drop in Normal Force vs Reynolds Number for Square Plate, from M.K. Abu Saleh [19].

Fig. 2.1: Flat, Square, Sharp-Edged Plate in Test Section of K.F.U.P.M. 0.8*1.1 m^2 Low-Speed Wind Tunnel.

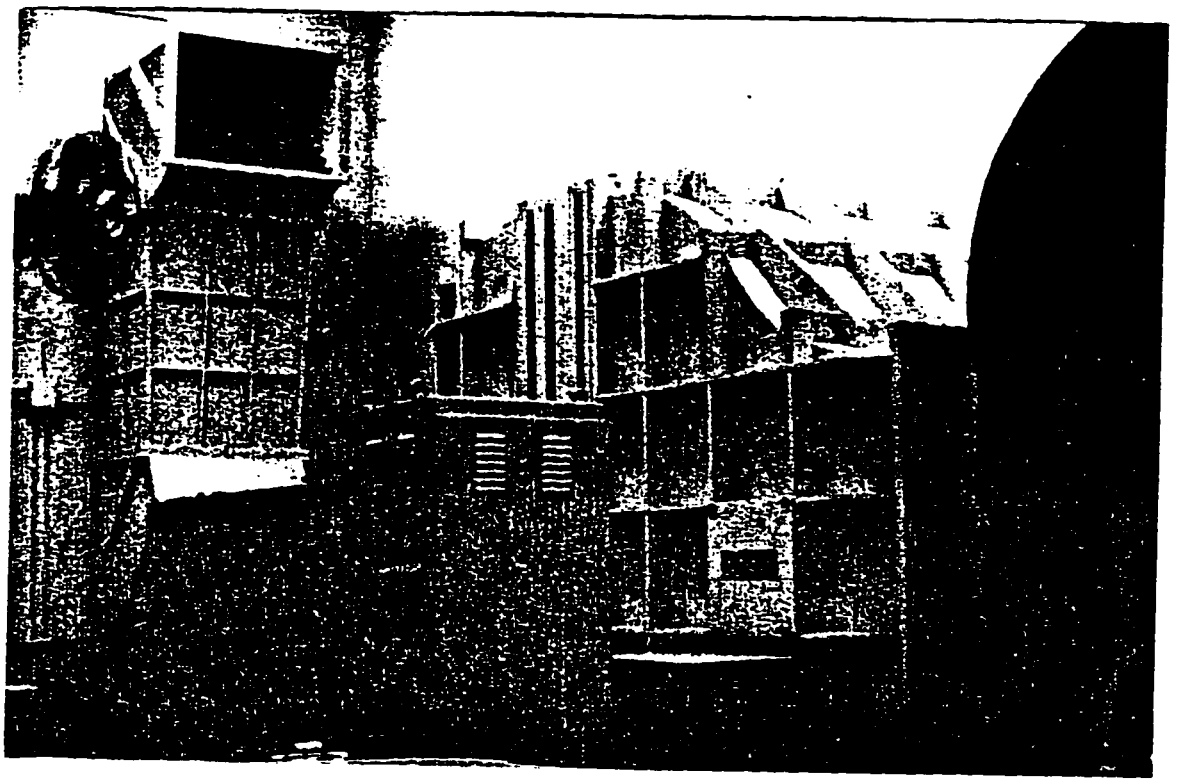

Fig. 2.2: K.F.U.P.M. $0.8 \times 1.1\,m^2$ Low-Speed Wind Tunnel.

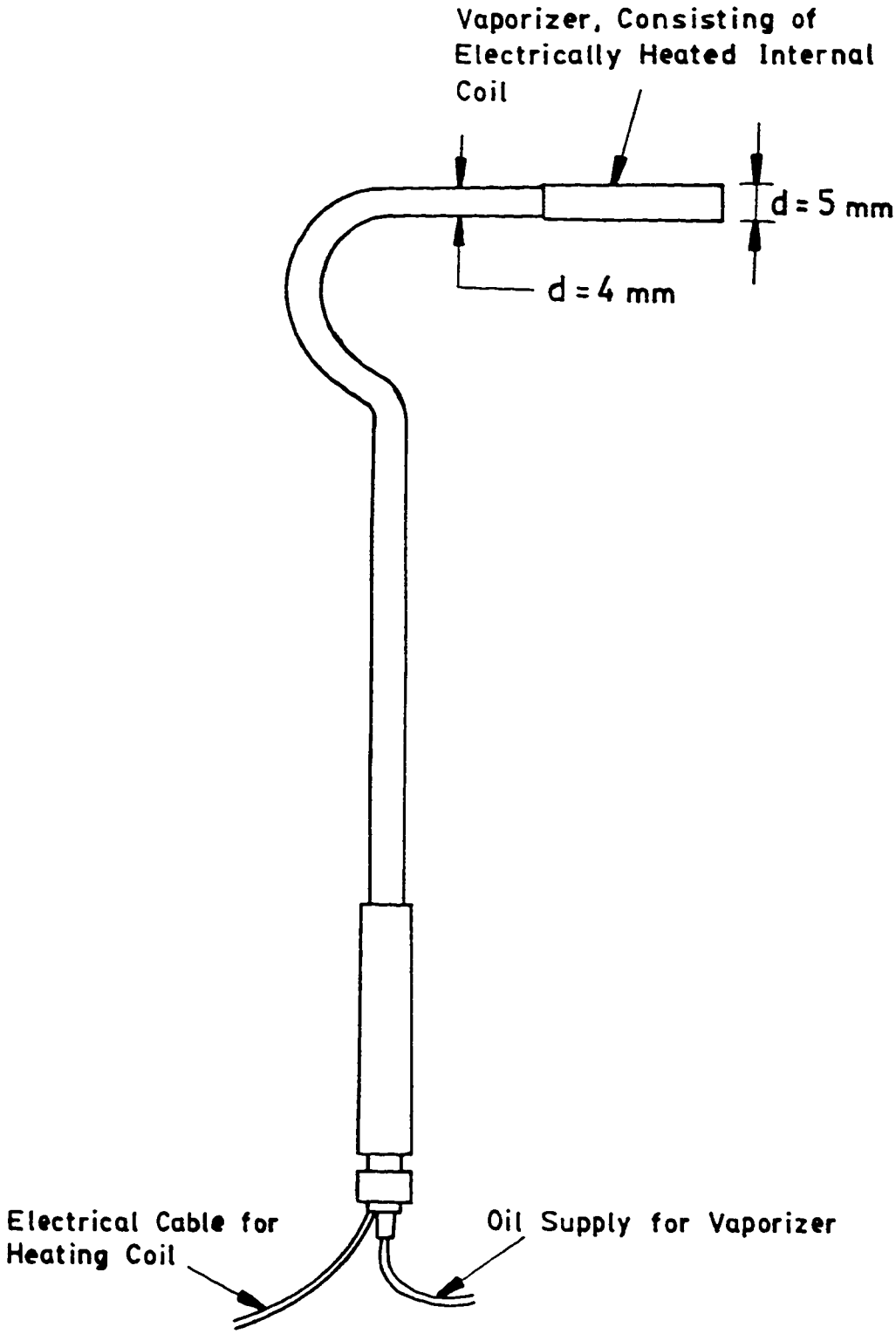

Fig. 2.3a Smoke Probe

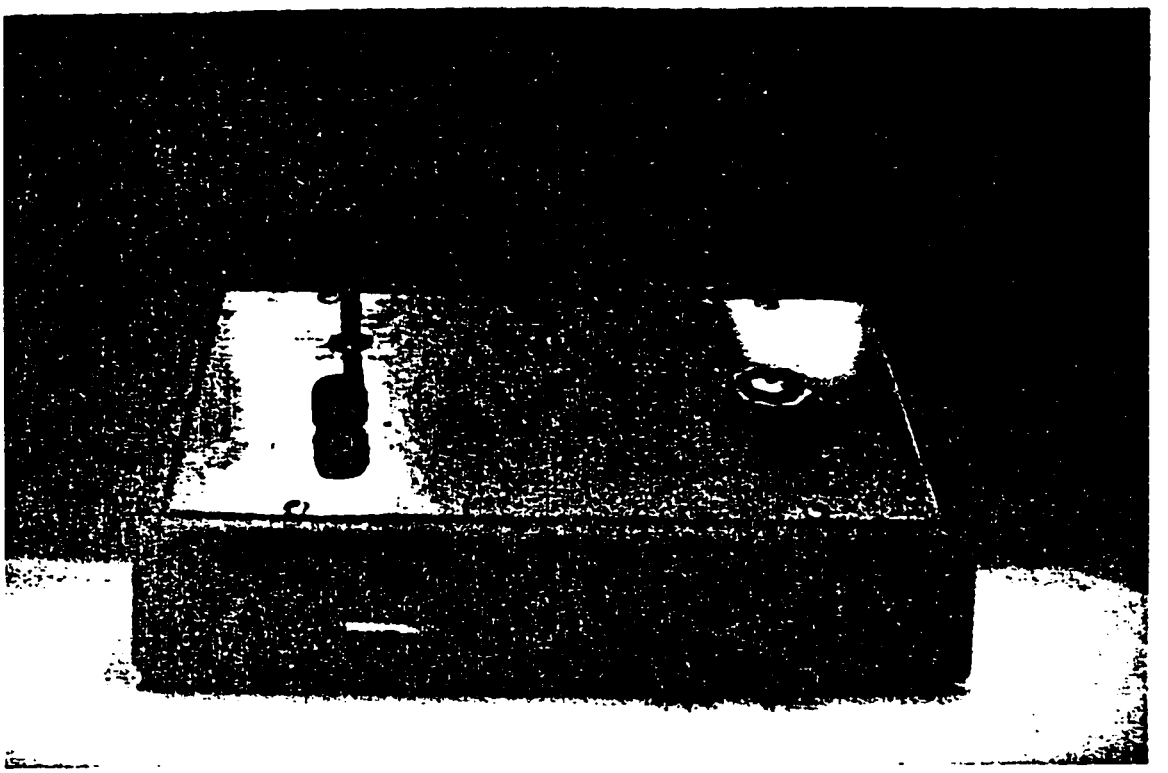

Fig. 2.3b: Oil-Supply and Control Unit for Smoke Generating Probe.

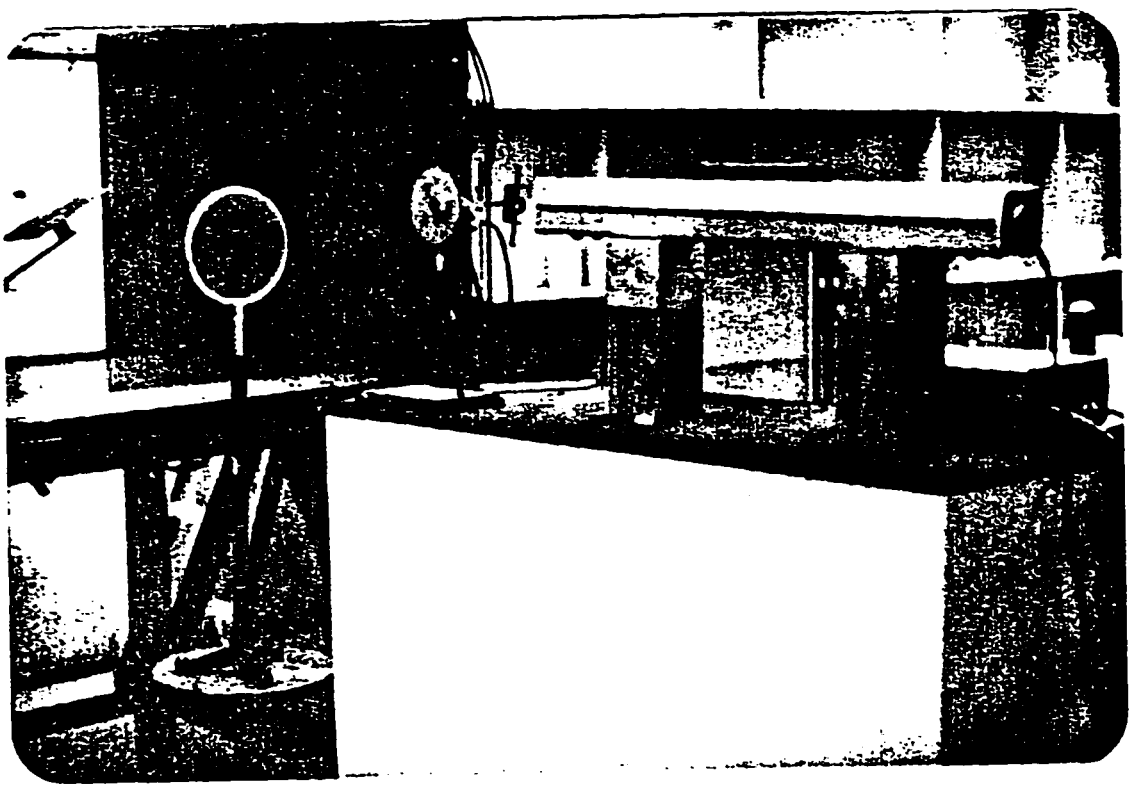

Fig. 2.4 Experimental Set-Up for Smoke Flow Visualization Using Laser-Light Plane.

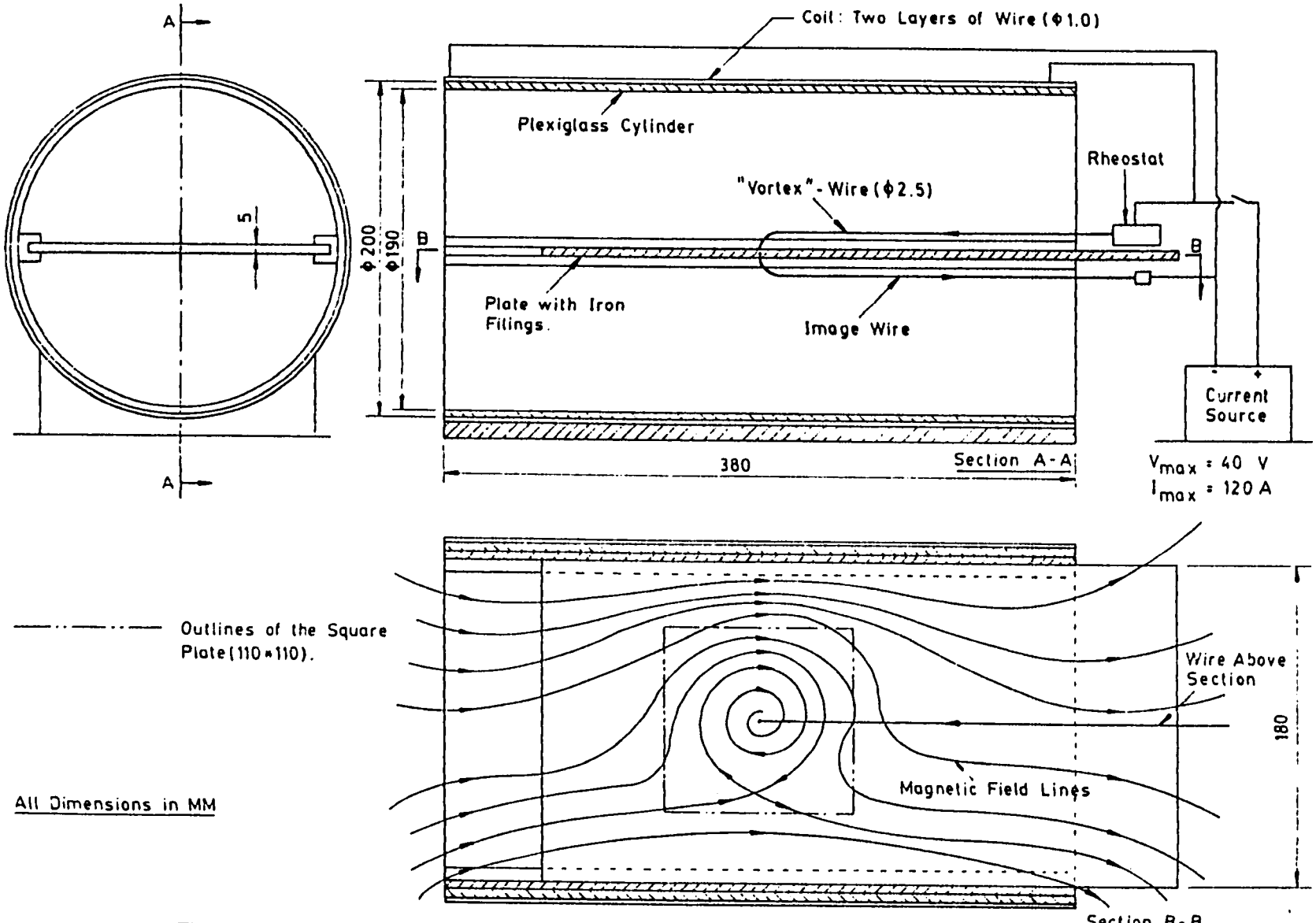

Fig. 2.5: Apparatus for Investigations Making Use of Electromagnetic Analogy.

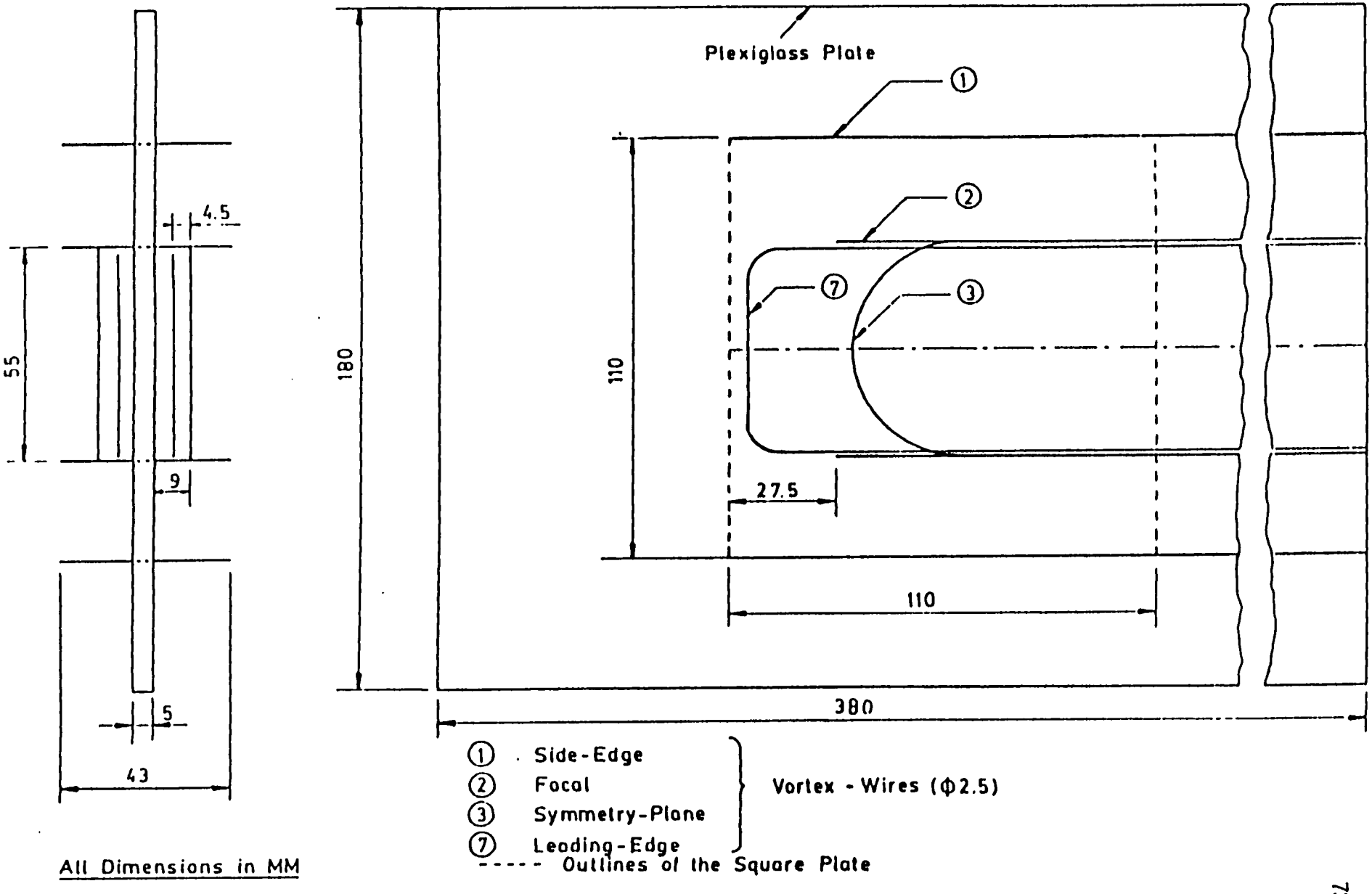

All Dimensions in MM

Fig. 2.6: Schematic Arrangement of Vortex - Wires.

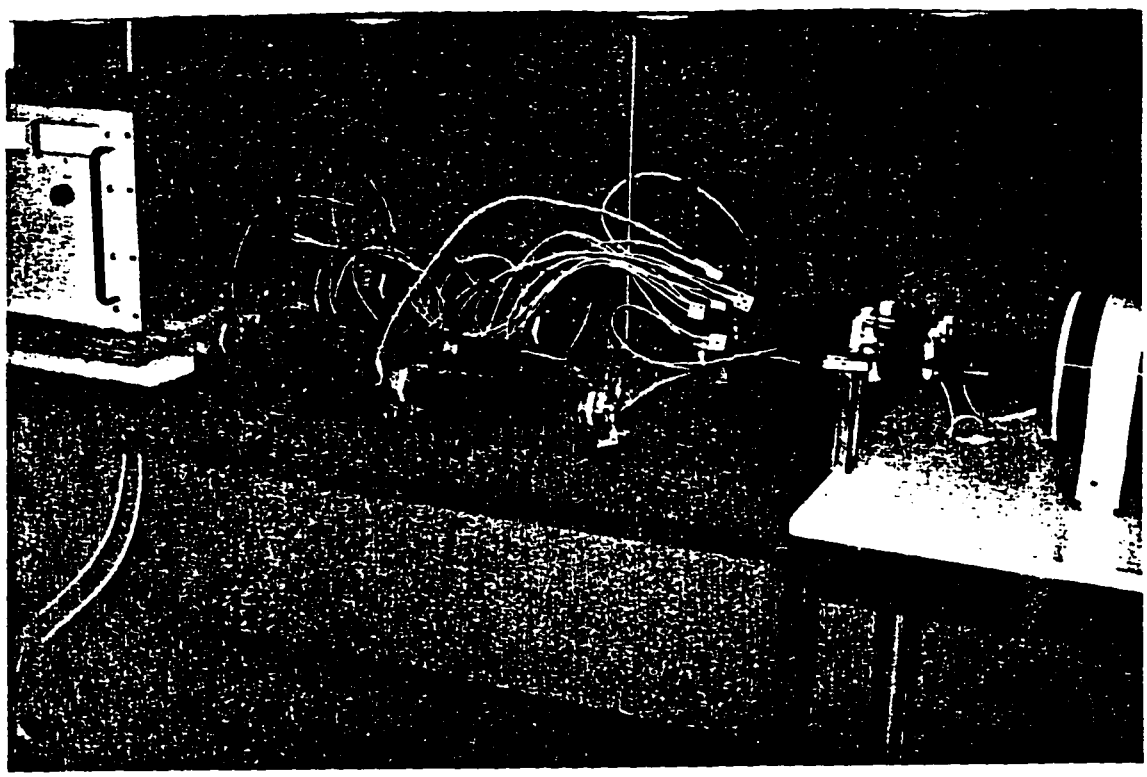

Fig. 2.7: Experimental Set-Up for Investigations Using Electromagnetic Analogy.

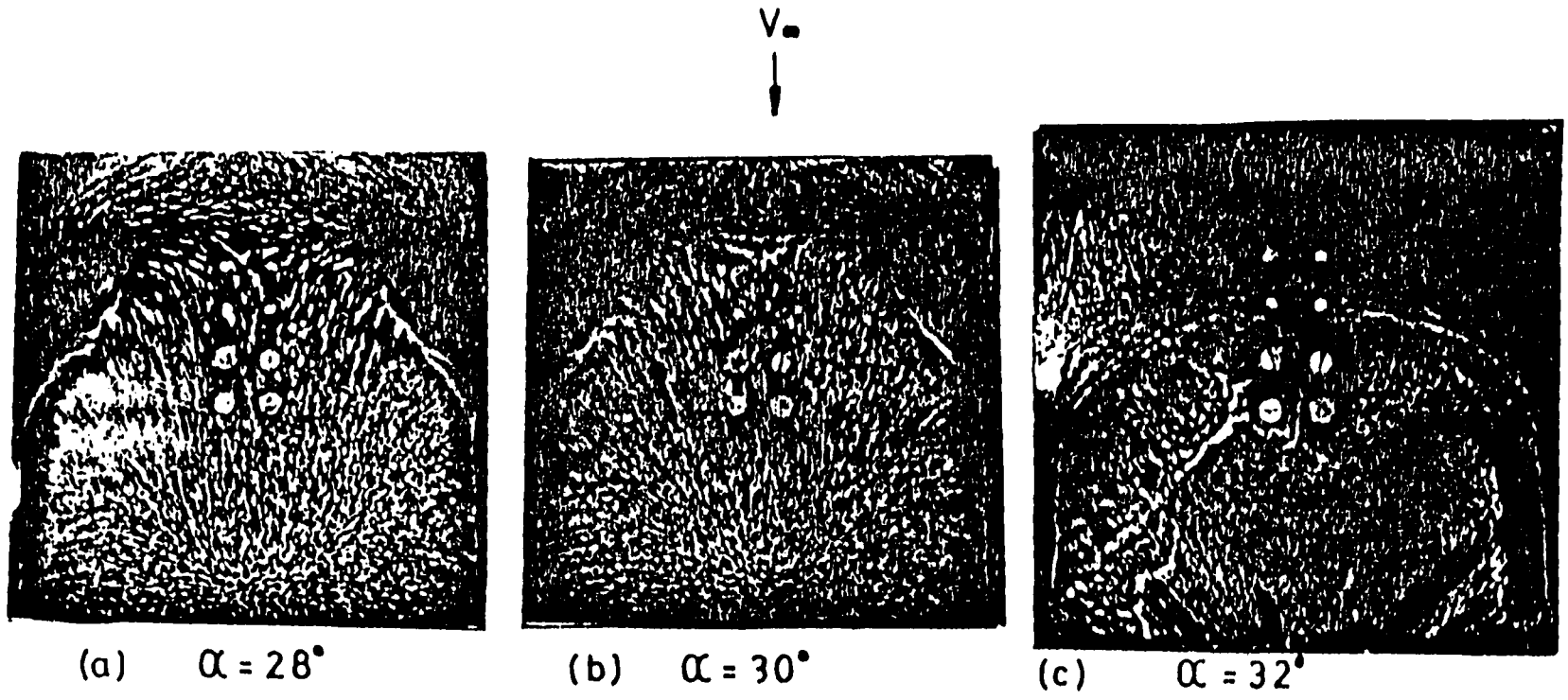

Fig. 3.1: Surface Flow Visualization on Suction Side of Square Plate at Incidence ($Re_c = 2.6 * 10^5$).

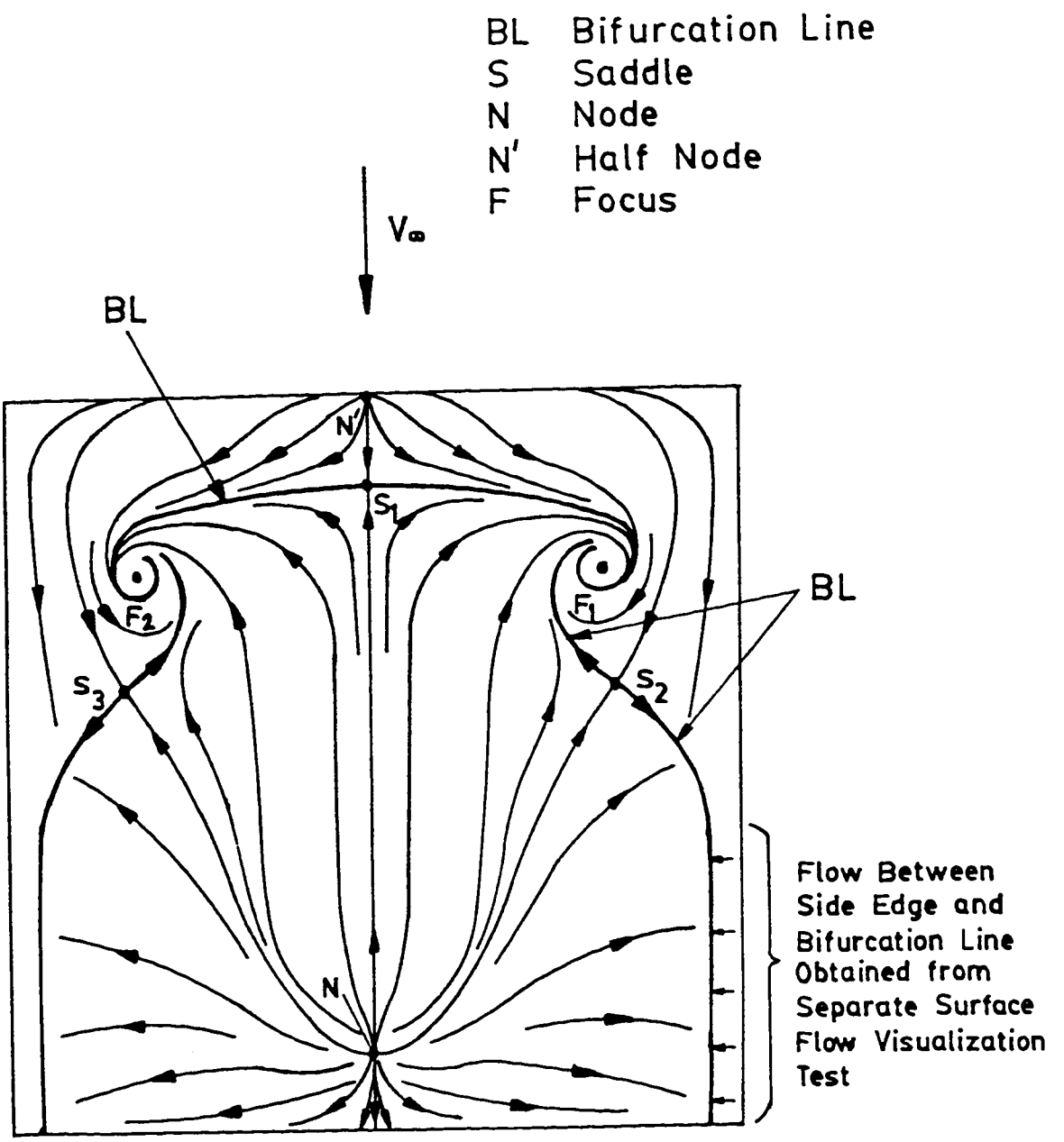

Fig. 3.2: Interpretation of Surface Flow Visualization Picture (Fig. 3.1a).

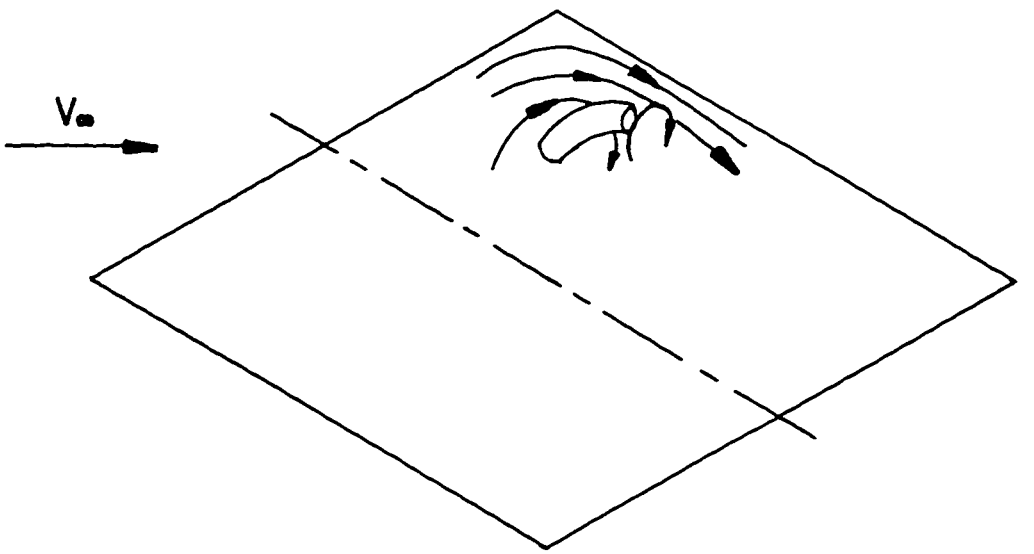

Fig. 3.3: Observed Flow Field Around and Above Focus from Smoke Flow Visualization; $\alpha = 25°$, $Re_c = 1.1 * 10^5$.

S Saddle
S′ Half Saddle
S″ Quarter Saddle
F Focus (Vortical Node)

$\Sigma S = 3$
$\Sigma N = 2$

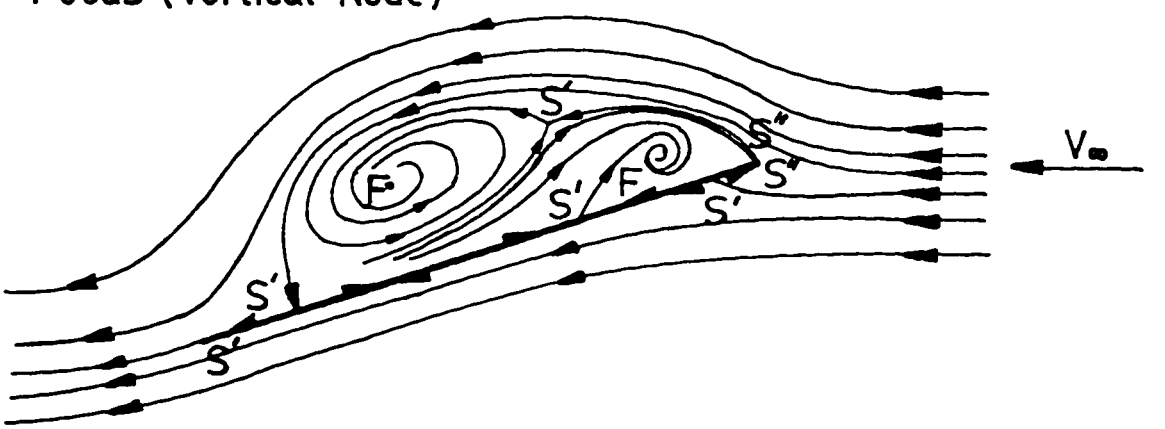

Fig. 3.4: Observed Flow in Symmetry Plane; $\alpha = 25°$, $Re_c = 1.1 * 10^5$.

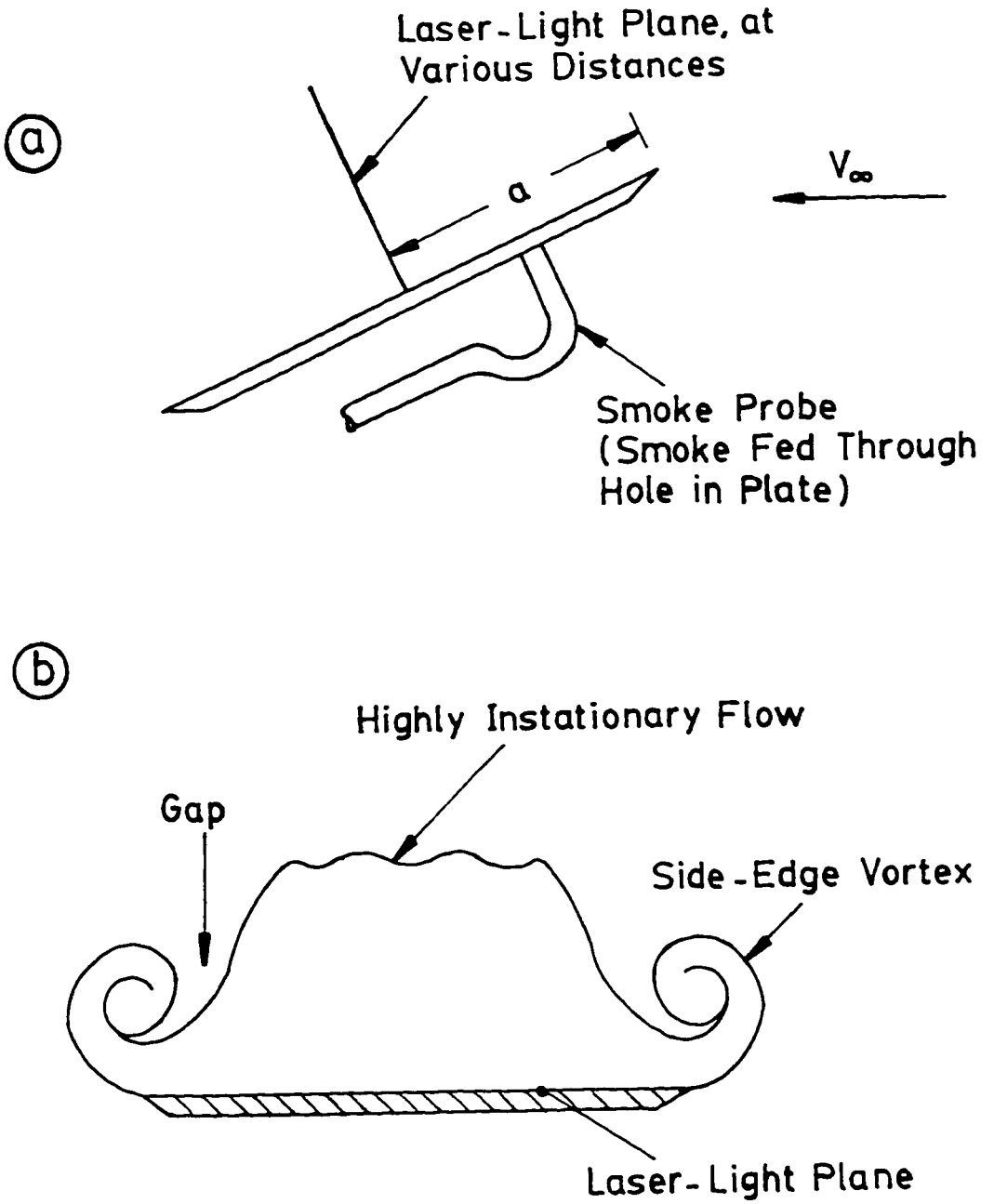

Fig. 3.5: Flow Observation in Planes Normal to Plate Centerline; $\alpha = 25°$, $Re_c = 1.1 * 10^5$,
(a) Arrangement for Flow Visualizations.
(b) Section Through Flow Field Over Rear Part of Plate.

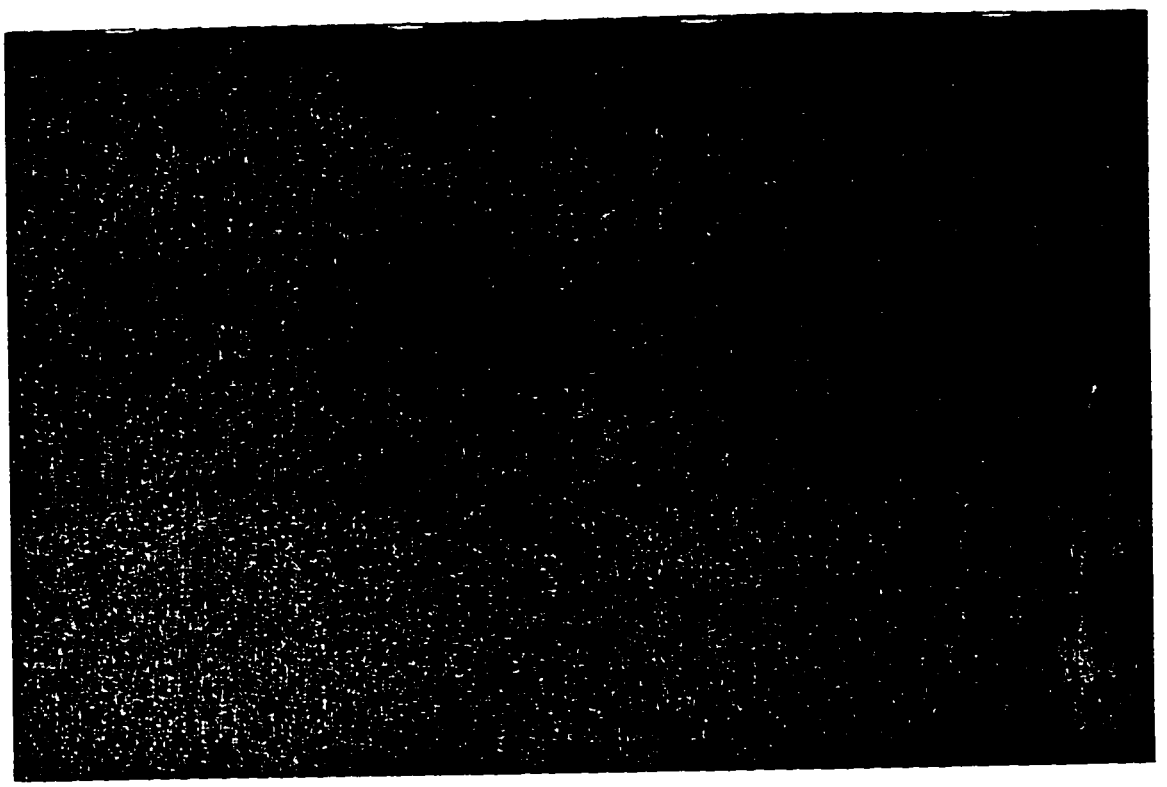

Fig. 3.6: Smoke Flow Visualization in Laser-Light Plane Normal to Plate Centerline; $\alpha = 25°$, $Re_c = 1.1 * 10^5$.

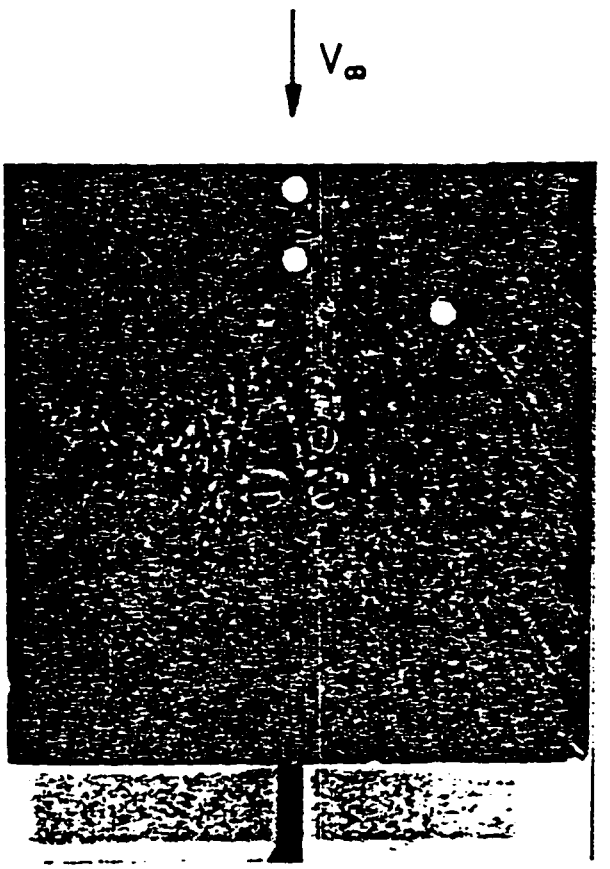

Fig. 3.7: Surface Flow Visualization on Pressure Side of Square Plate; $\alpha = 25°$, $Re_c = 2.6 * 10^5$.

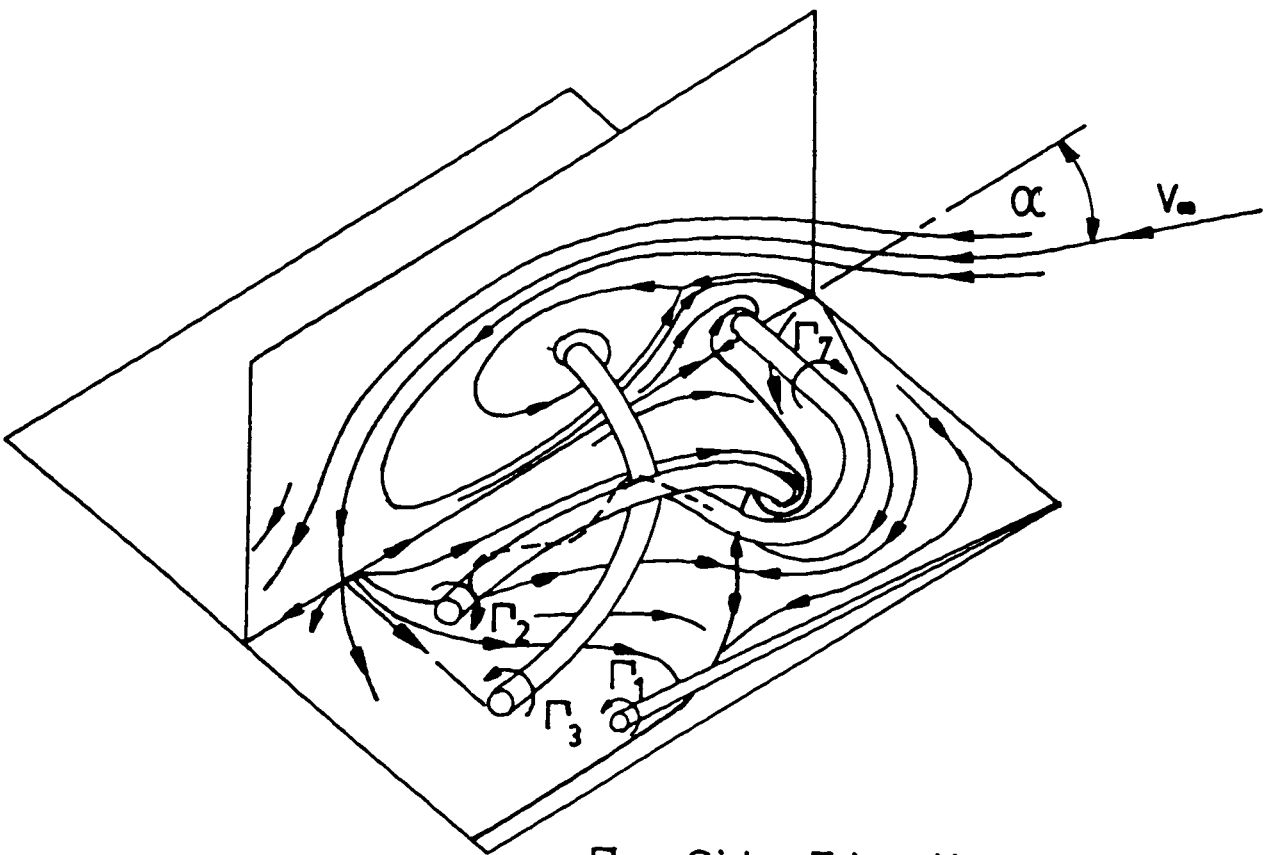

Γ_1 Side-Edge Vortex
Γ_2 Focal Vortex
Γ_3 Symmetry-Plane Vortex
Γ_7 Leading-Edge Vortex

Fig. 3.8 Conjectured Time-Mean Flow Pattern on Suction Side of Plate; $\alpha = 25°$, $Re_c = 1.1 * 10^5$.

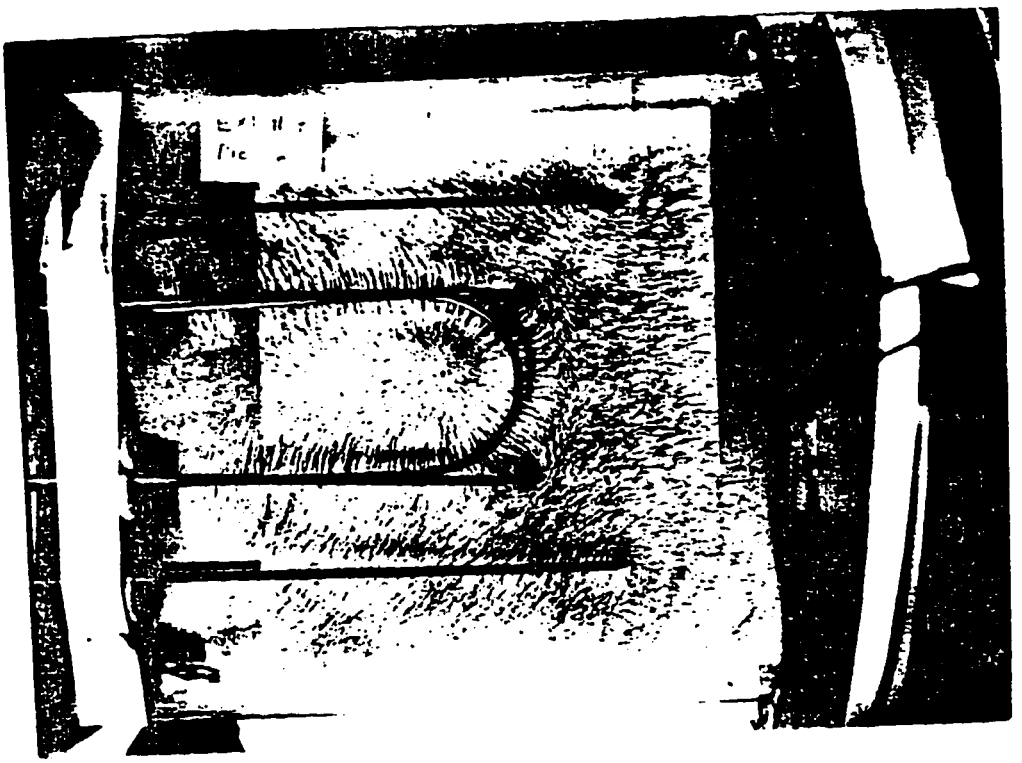

Fig. 3.9: Surface Flow Pattern, without Leading-Edge Vortex on Square Plate Using Electromagnetic Analogy.

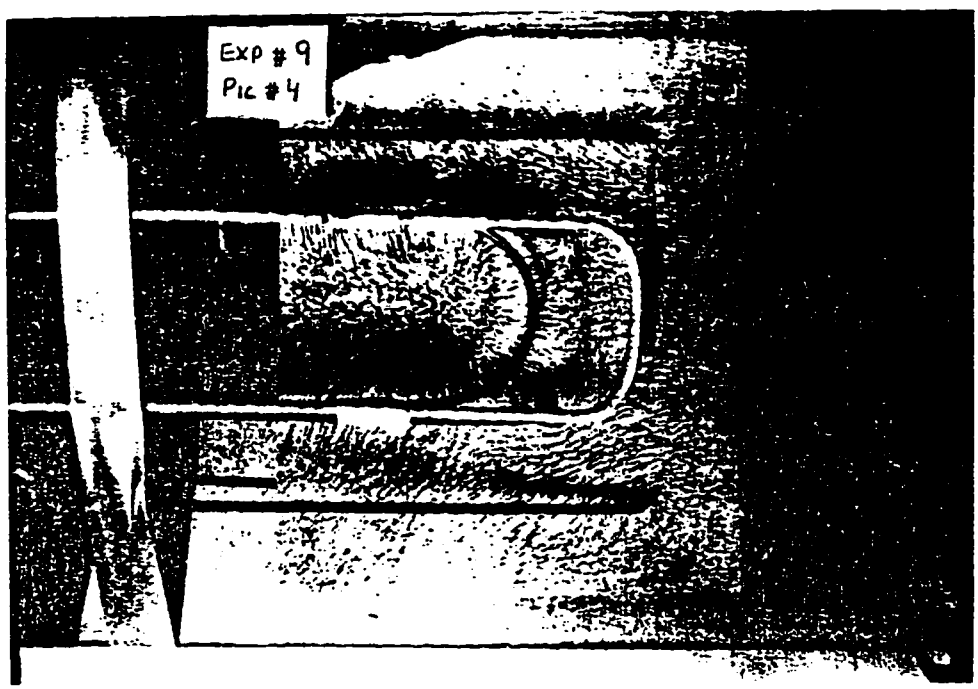

Fig. 3.10: Surface Flow Pattern, with Leading-Edge Vortex on Square Plate Using Electromagnetic Analogy.

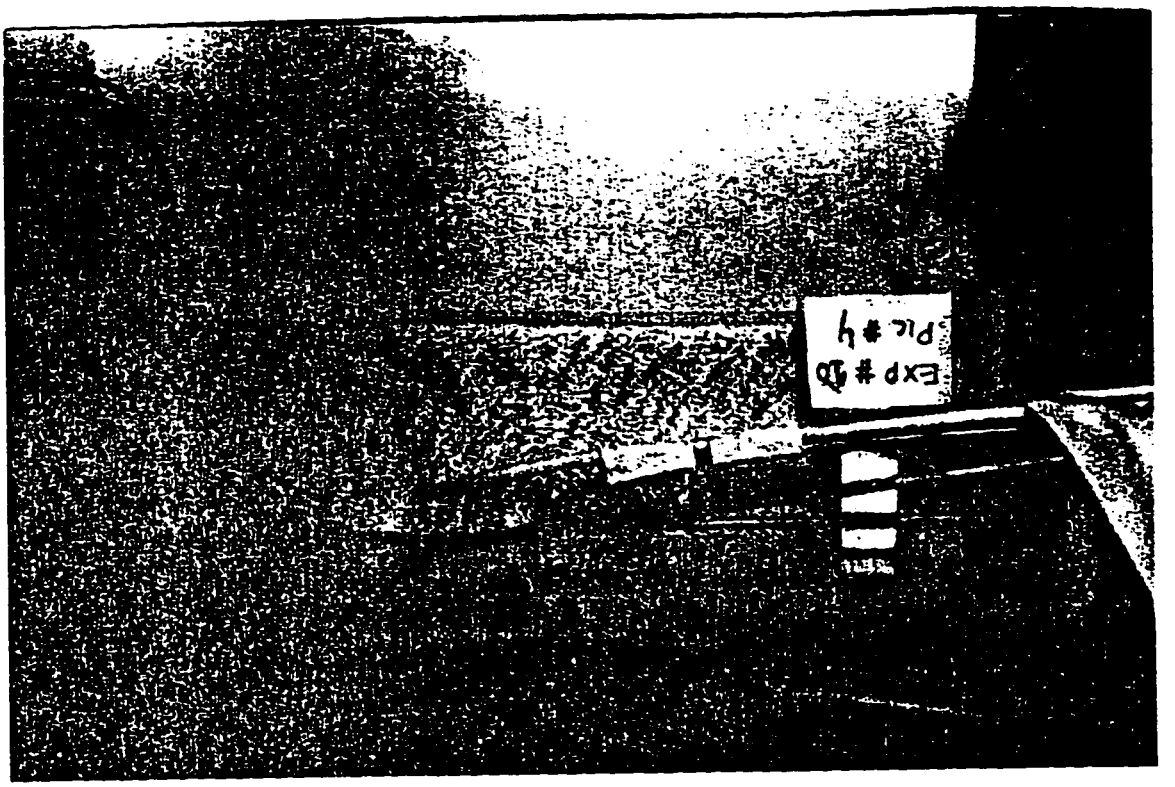

Fig. 3.11: Flow Pattern in Symmetry Plane of Square Plate Using Electromagnetic Analogy.

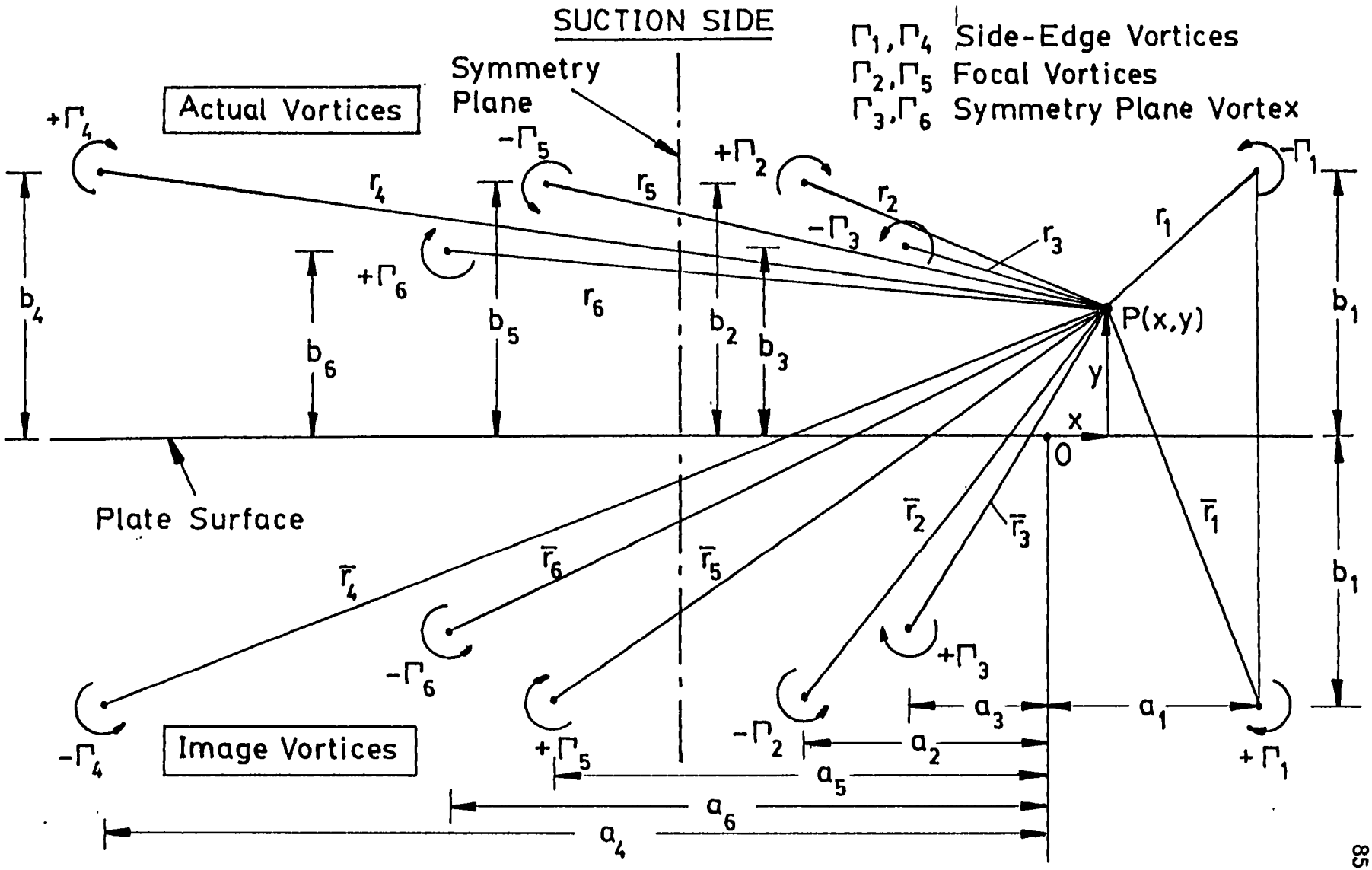

Fig. 3.12: Evaluation of ψ_R at an Arbitrary Point P(x,y) for a System of Vortices in Plane Normal to Plate Centerline.

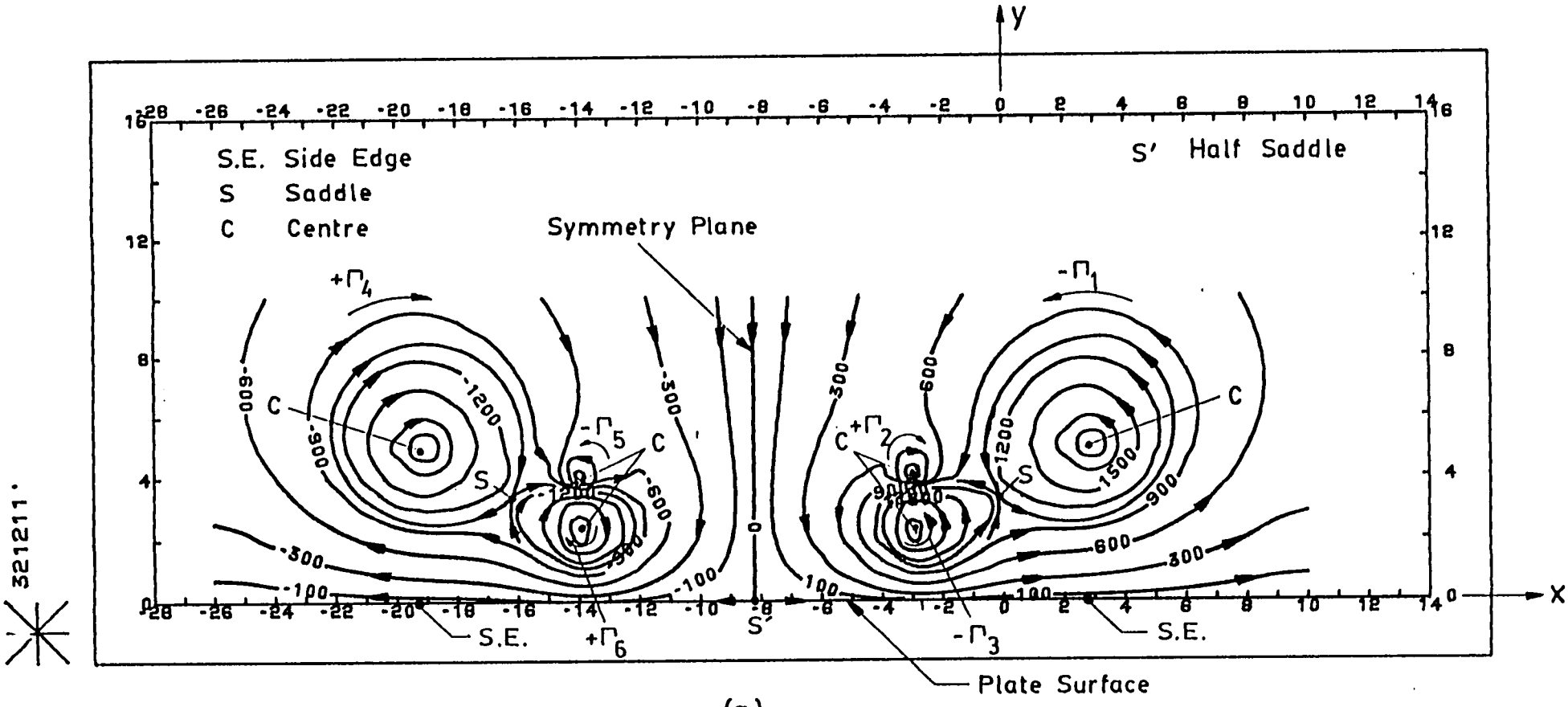

(a)

Fig. 3.13 Resultant Flow Field in Plane Normal to Plate Centerline due to Potential Vortices ($\Gamma_1 = \Gamma_4$, $\Gamma_2 = \Gamma_5$, $\Gamma_3 = \Gamma_6$, for $\Gamma_1 = 0.5\ [m^2/s]$), (a) $\Gamma_3 = 2\Gamma_1$, $\Gamma_2 = \Gamma_1$,

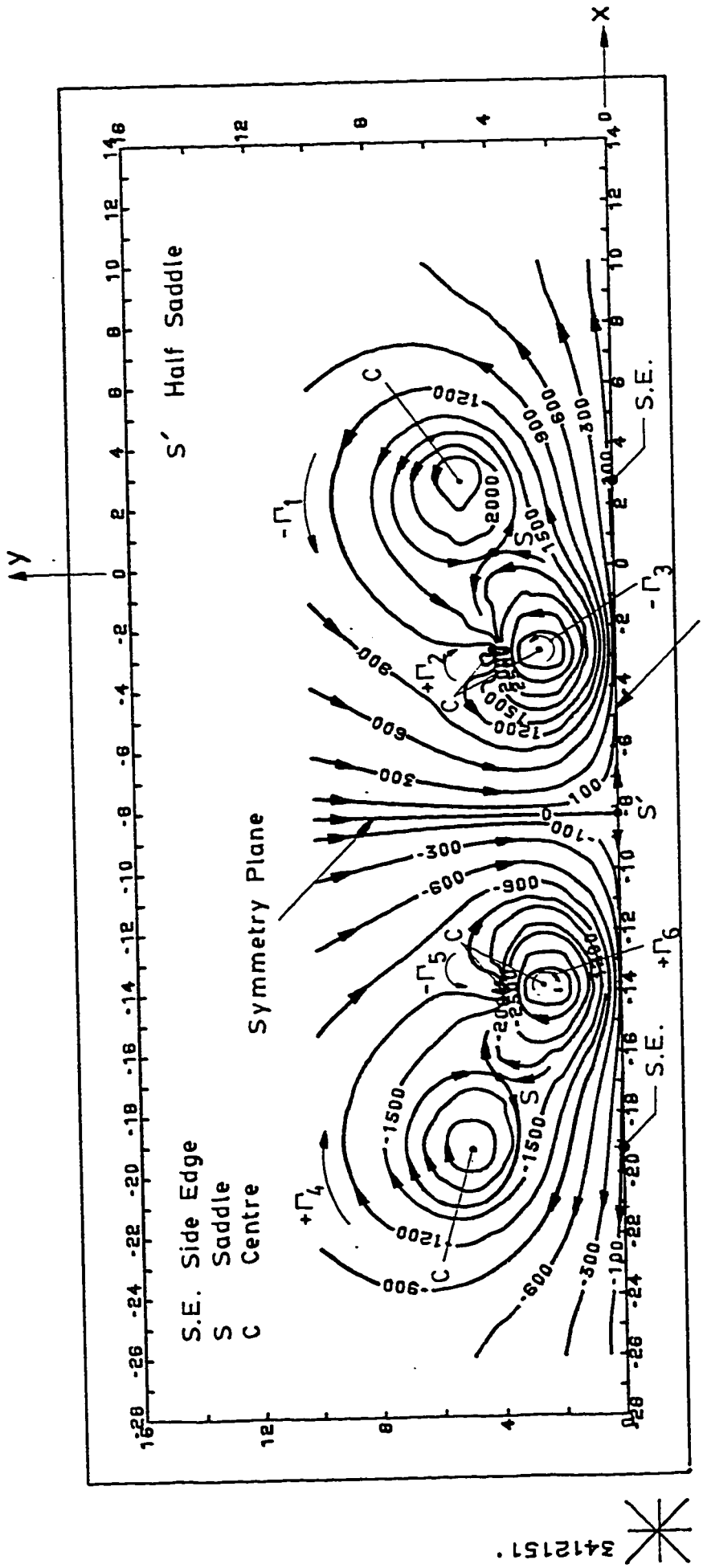

(b)

Fig. 3.13 ctd.: (b) $\Gamma_3 = 4\Gamma_1$, $\Gamma_2 = 1.5\Gamma_1$

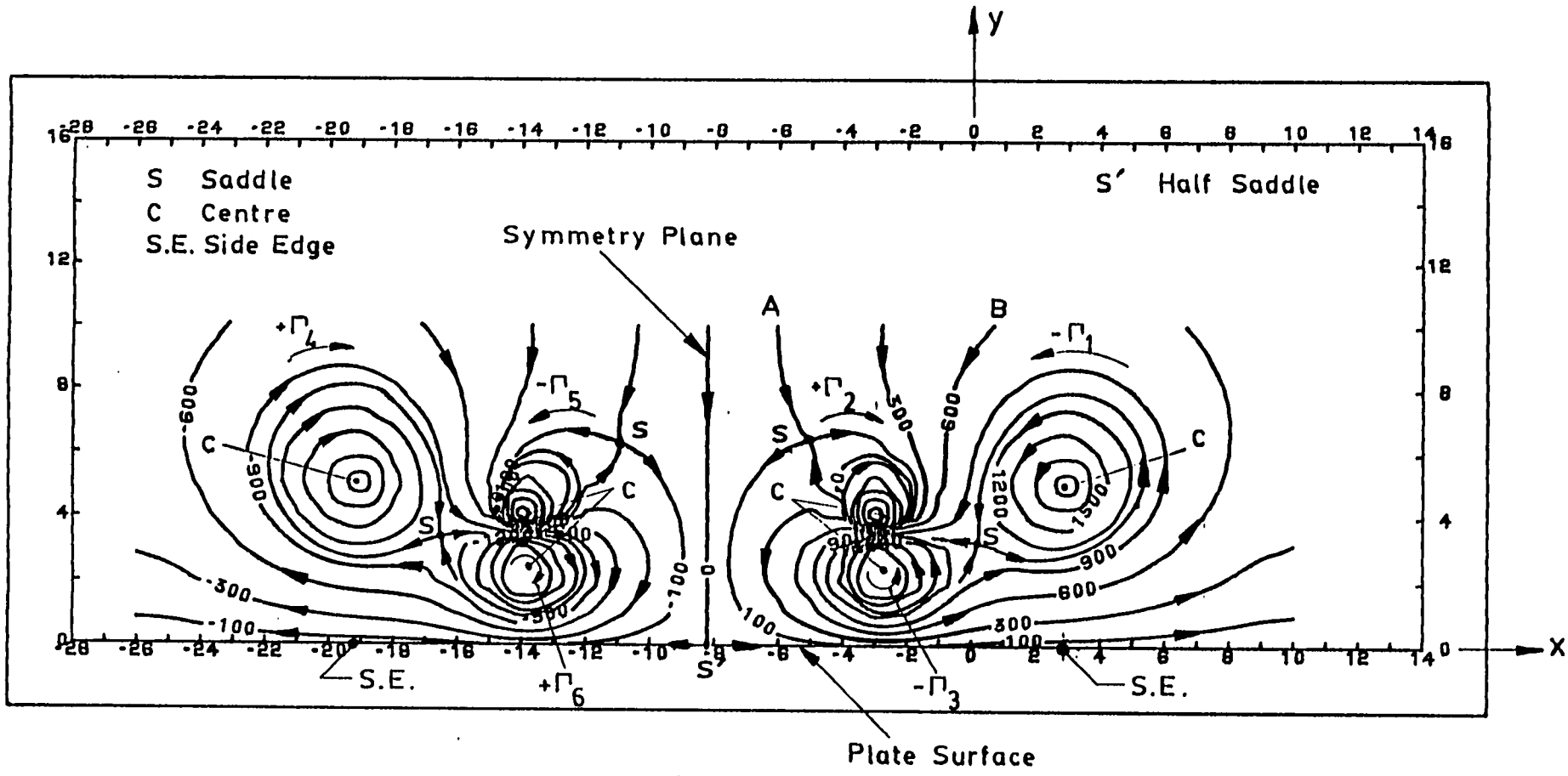

(c)

Fig. 3.13 ctd.: (c) $\Gamma_3 = 3\Gamma_1$, $\Gamma_2 = 2\Gamma_1$

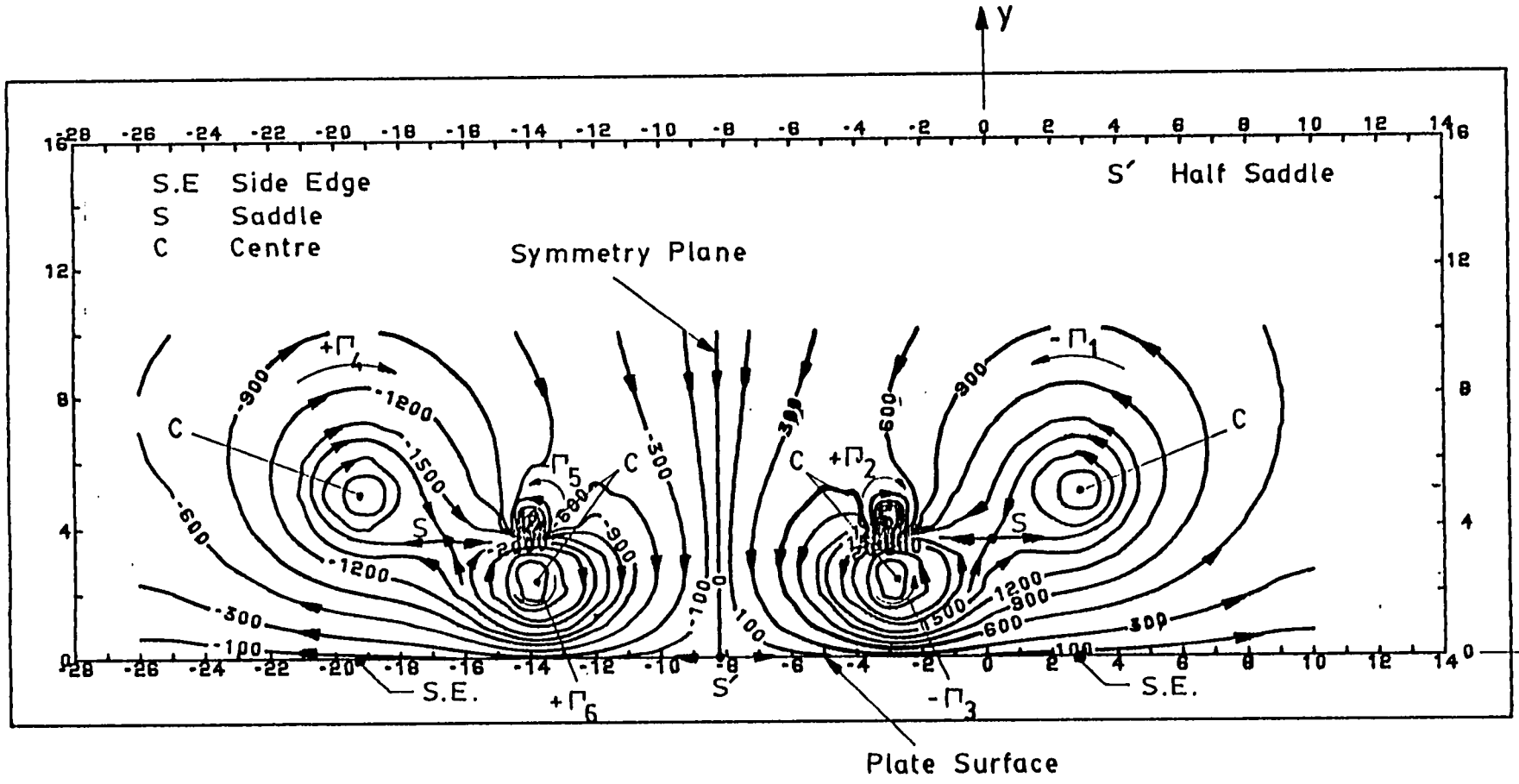

(d)

Fig. 3.13 ctd.: (d) $\Gamma_3 = 4\Gamma_1$, $\Gamma_2 = 2\Gamma_1$.

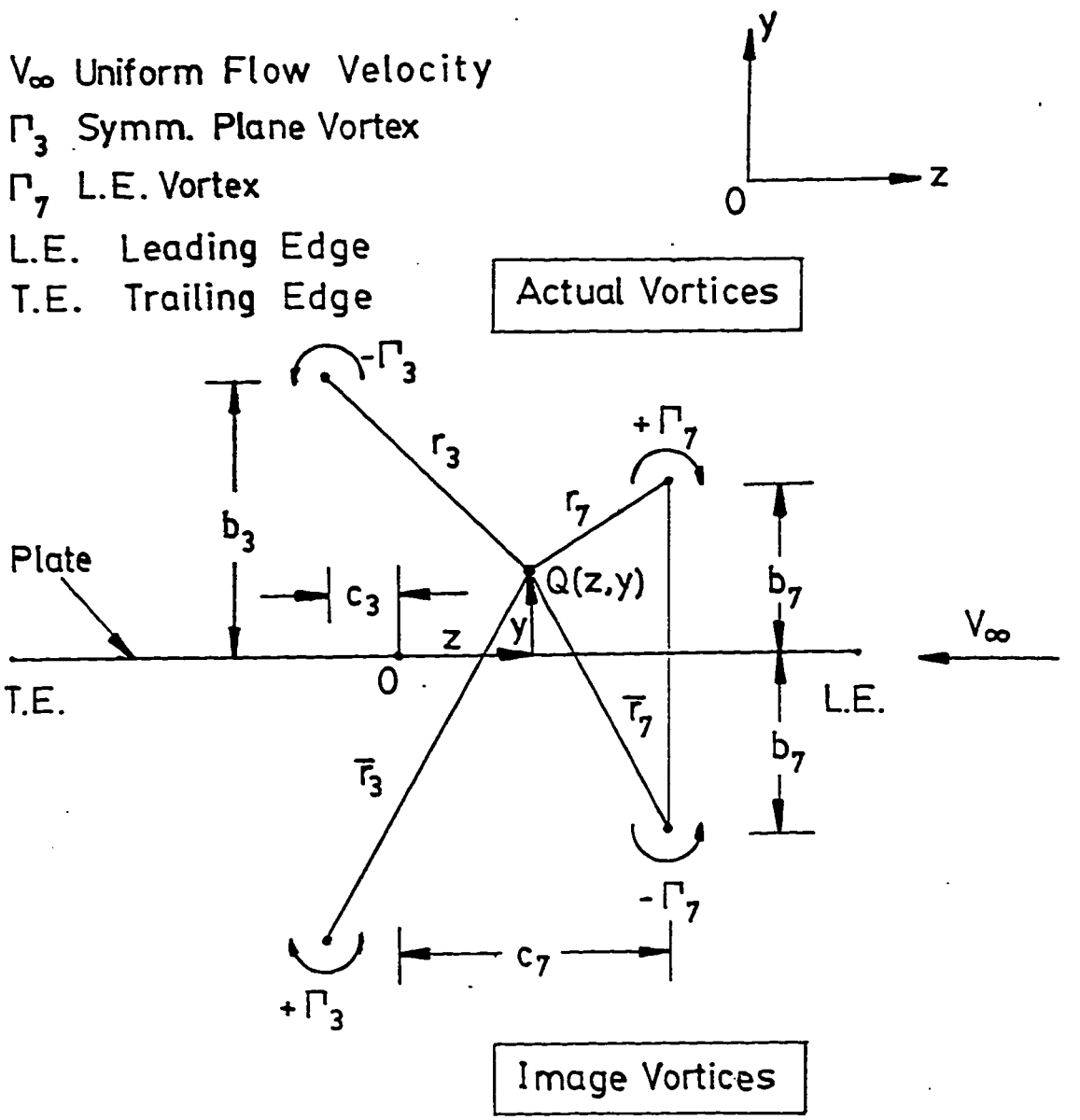

Fig. 3.14 Evaluation of ψ_R at an Arbitrary Point Q(z,y) in the Symmetry Plane of Square, Flat Plate.

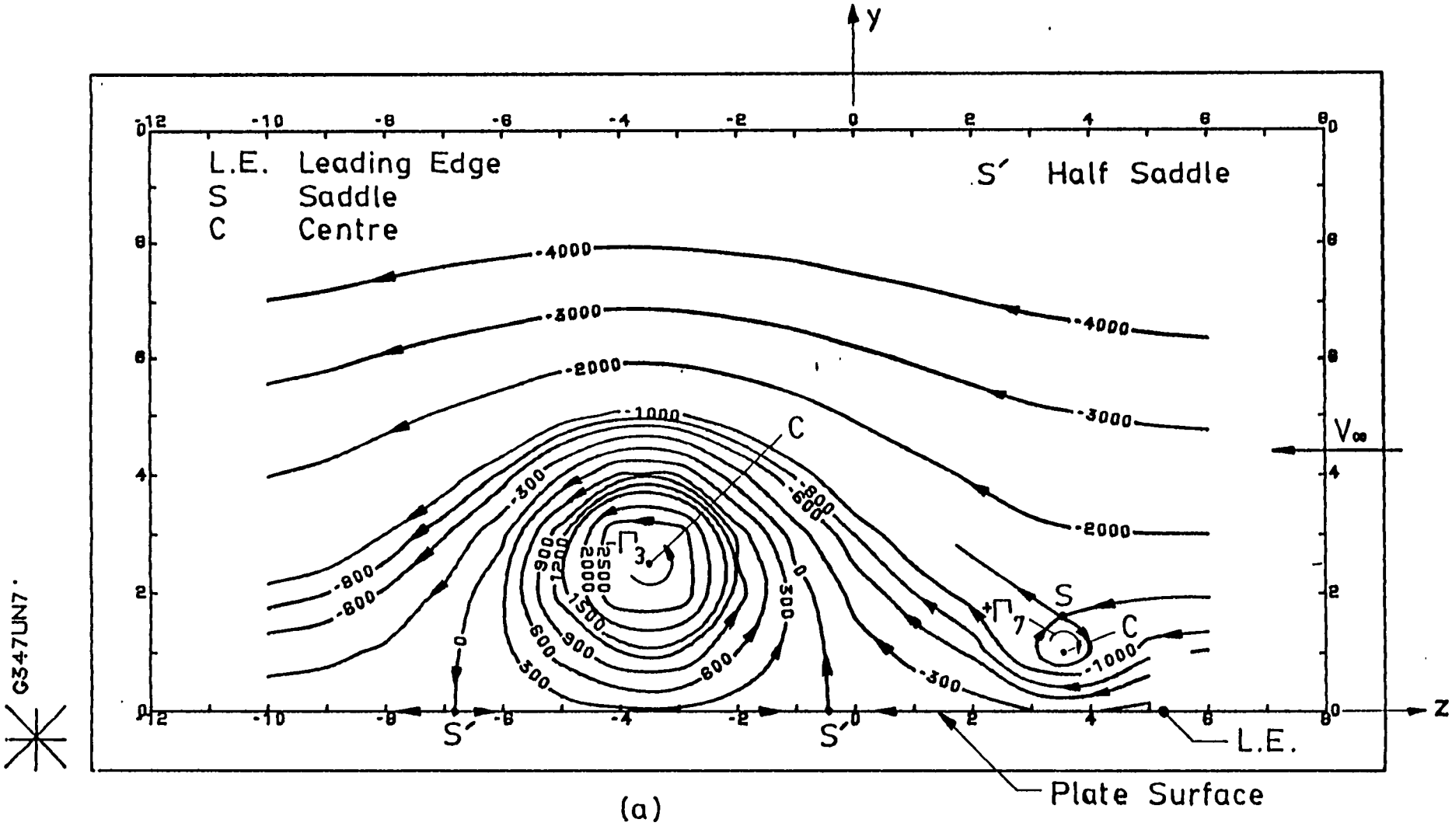

(a)

Fig. 3.15 Resultant Flow Field in Symmetry Plane due to Potential Vortices and Uniform Flow;
(a) $\Gamma_3 = 1.5\,[m^2/s]$, $\Gamma_3 = 4\Gamma_7$, $V_\infty = 7.0\,[m/s]$,

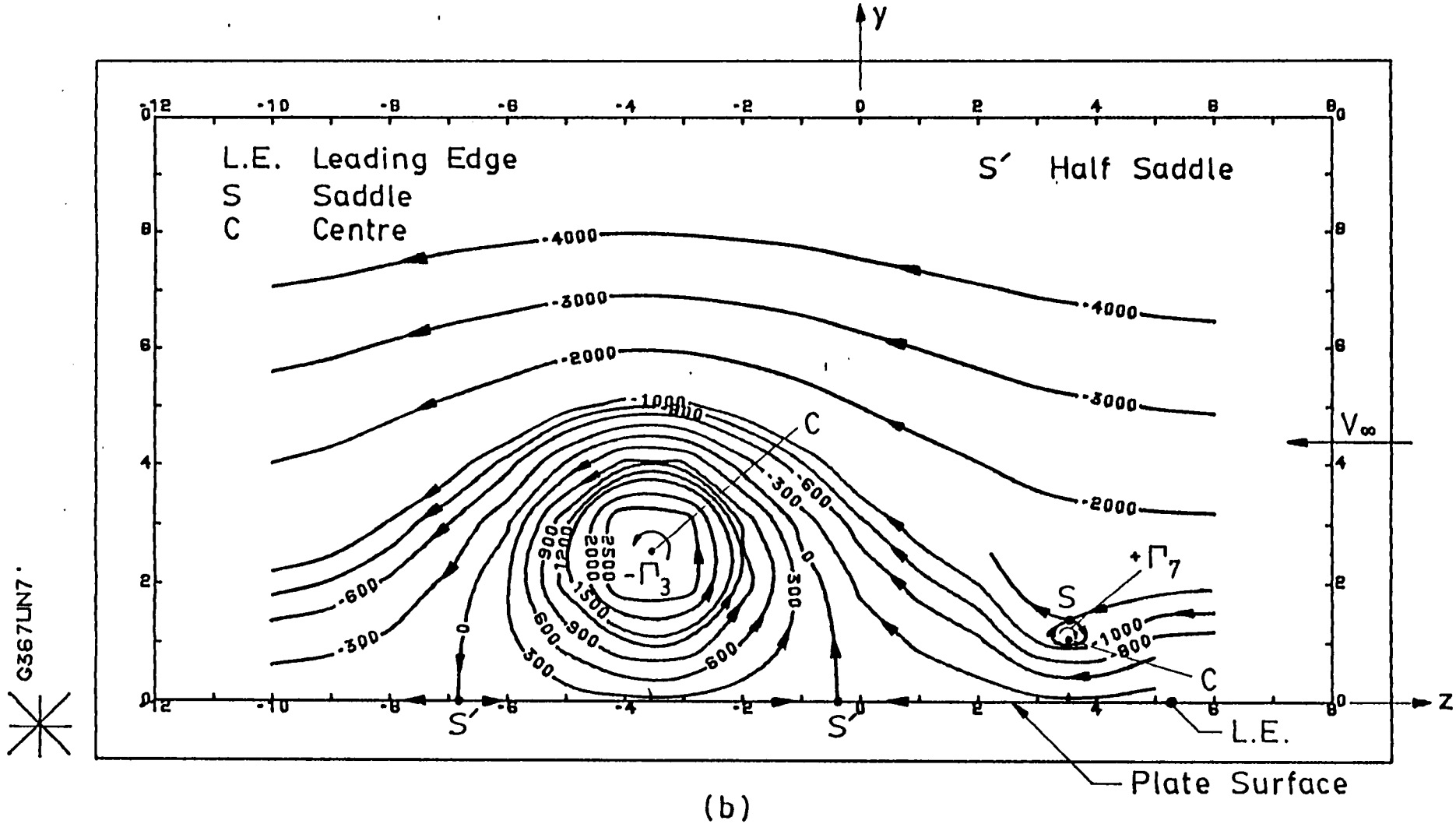

(b)

Fig. 3.15 ctd. : (b) $\Gamma_3 = 1.5\ [m^2/s]$, $\Gamma_3 = 6\Gamma_7$, $V_\infty = 7.0\ [m/s]$.

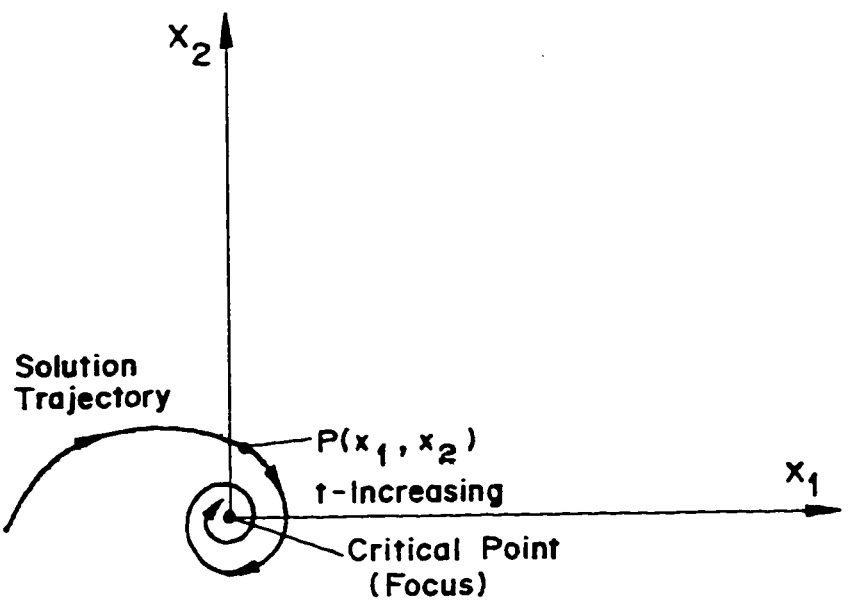

Fig. I.1: Solution Trajectory and Critical Point at Origin in Phase Plane.

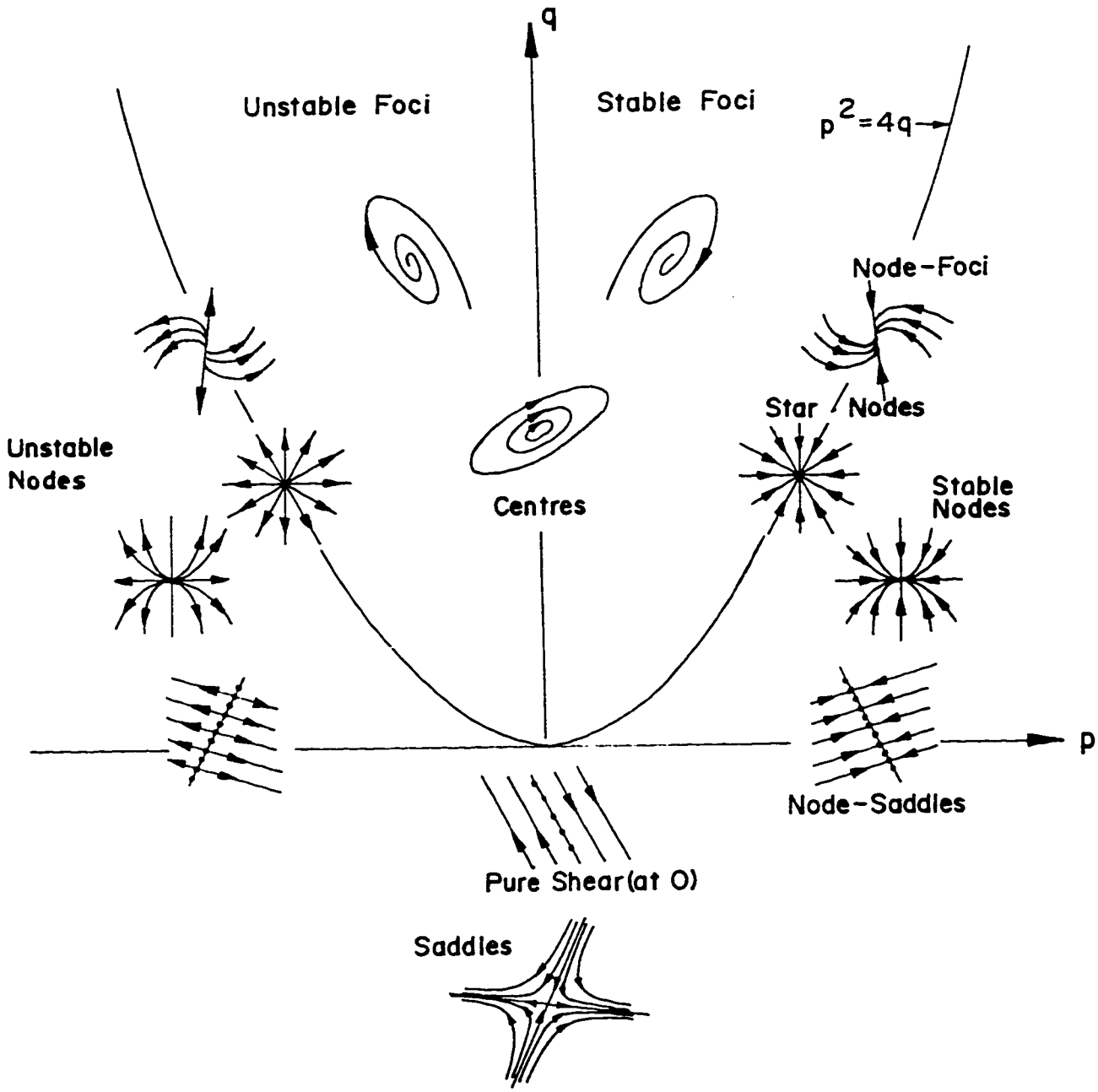

Fig. I.2: Classification of Critical Points.

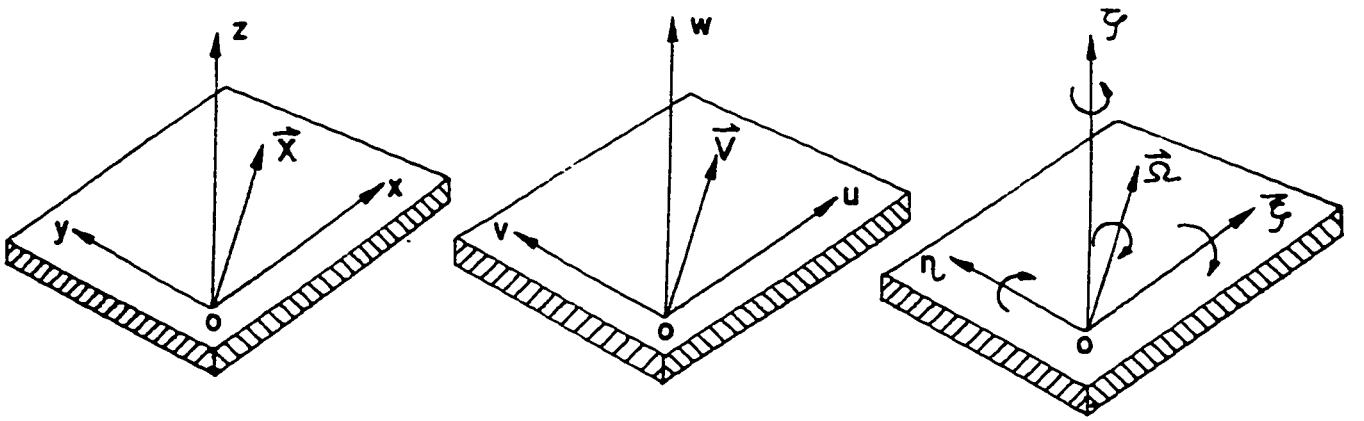

Fig. I.3: Systems of Coordinates for Position, Velocity, and Vorticity.

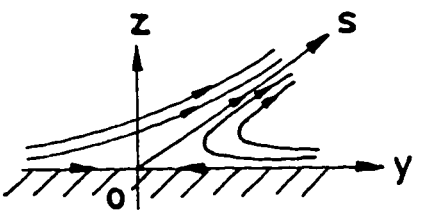

Symmetry Plane
Saddle Point at O

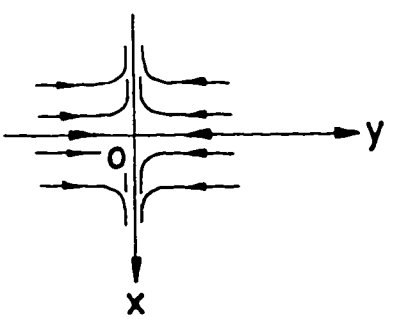

Wall Plane
Saddle Point at O

Saddle-Saddle-Node Trio

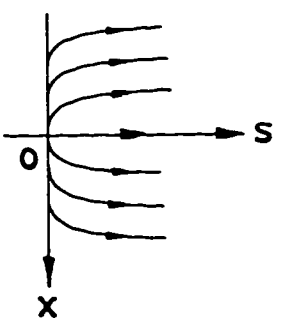

Separated-Flow Plane
Nodal Point at O

Fig. I.4: Phase Planes with Solution Trajectories (Streamlines) Near Critical Points.

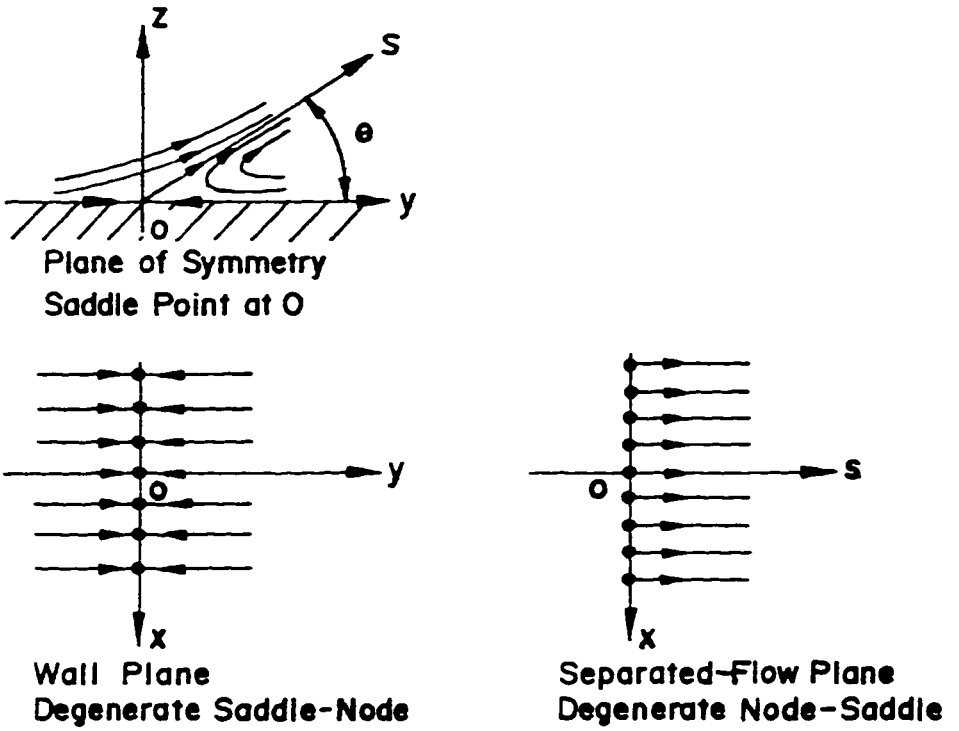

Fig. I.5: Degenerate Case of Two-Dimensional Flow Separation.

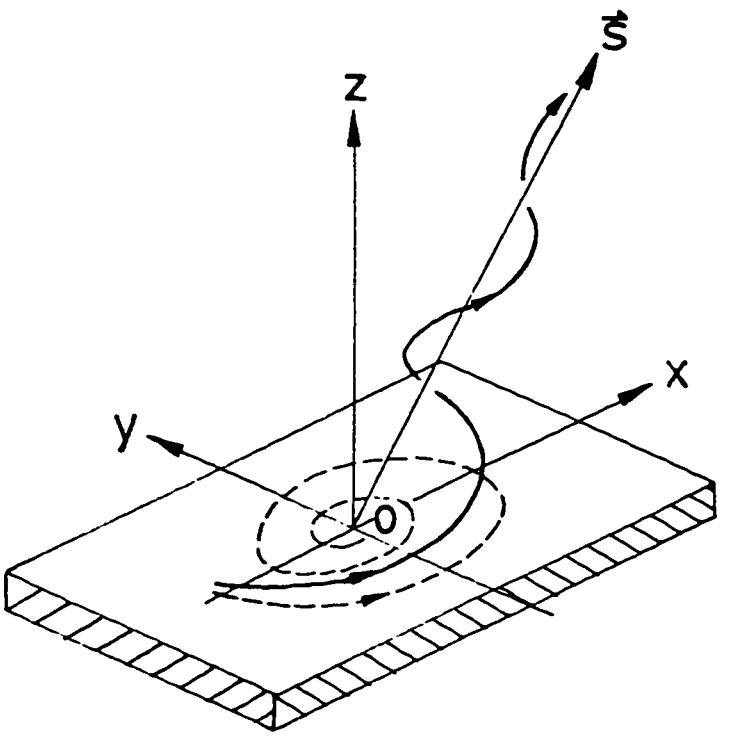

Fig. I.6: Solution Trajectories Near a Focus.

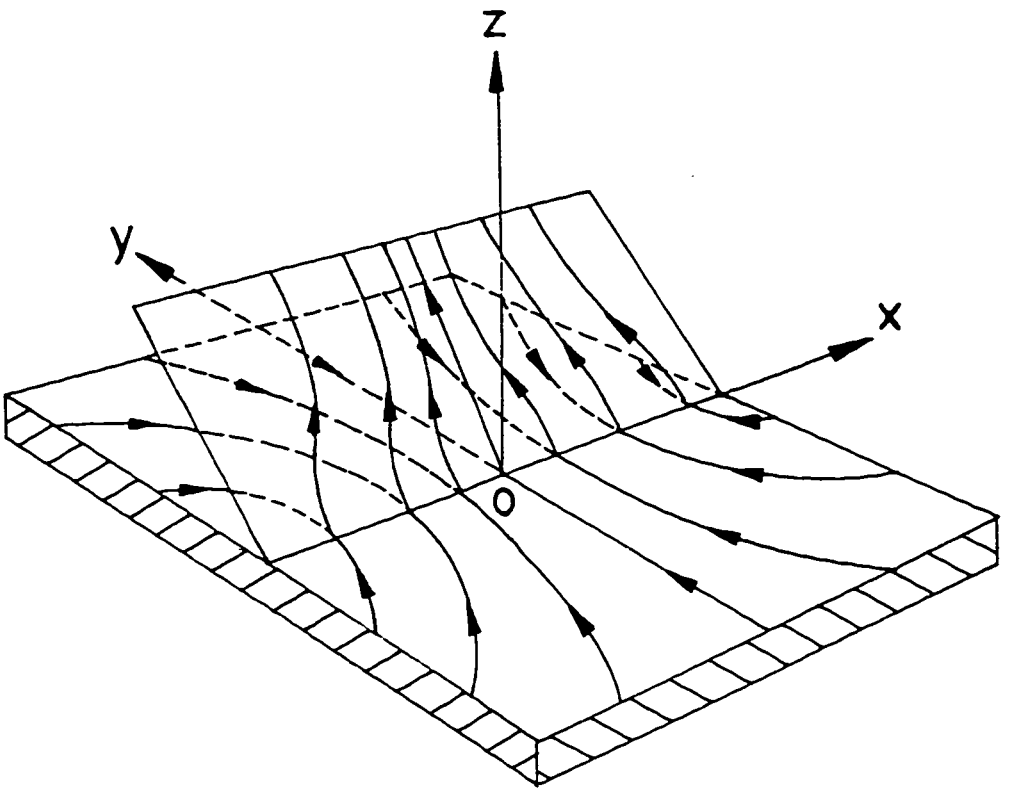

Fig. I.7: Pattern of Flow Separation Near Almost Two-Dimensional Critical Point, According to A.E.Perry [23].

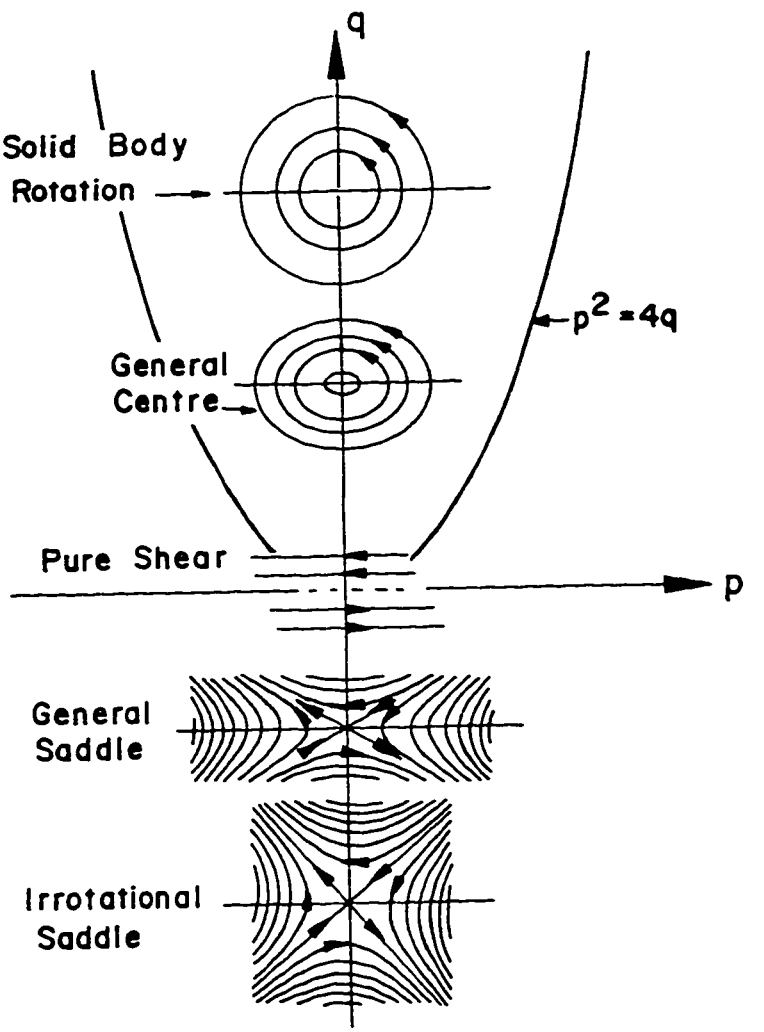

Fig. 1.8: Family of Flow Patterns Near Critical Points in Flow with Uniform Vorticity from A.E.Perry [23].

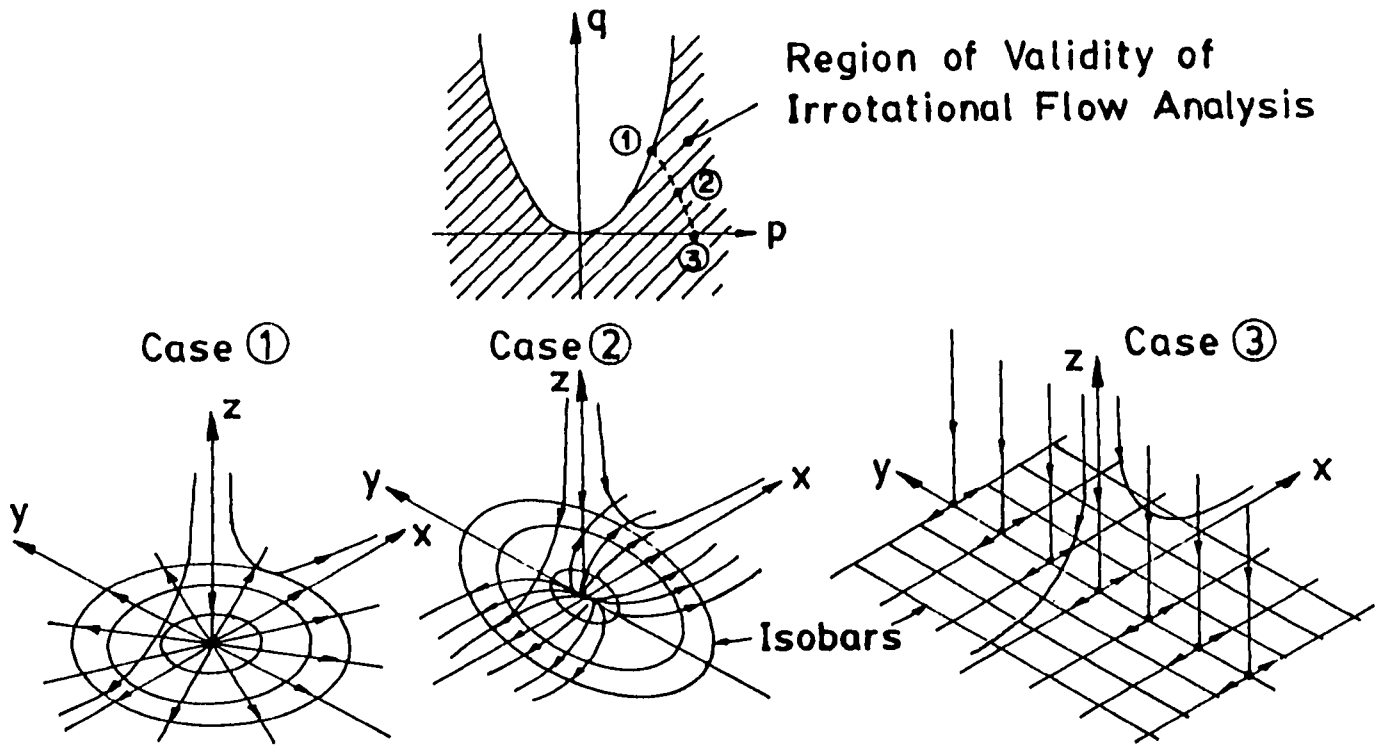

Fig. I.9: Critical Points in Irrotational Flow in xy Plane, According to A.E.Perry [23].

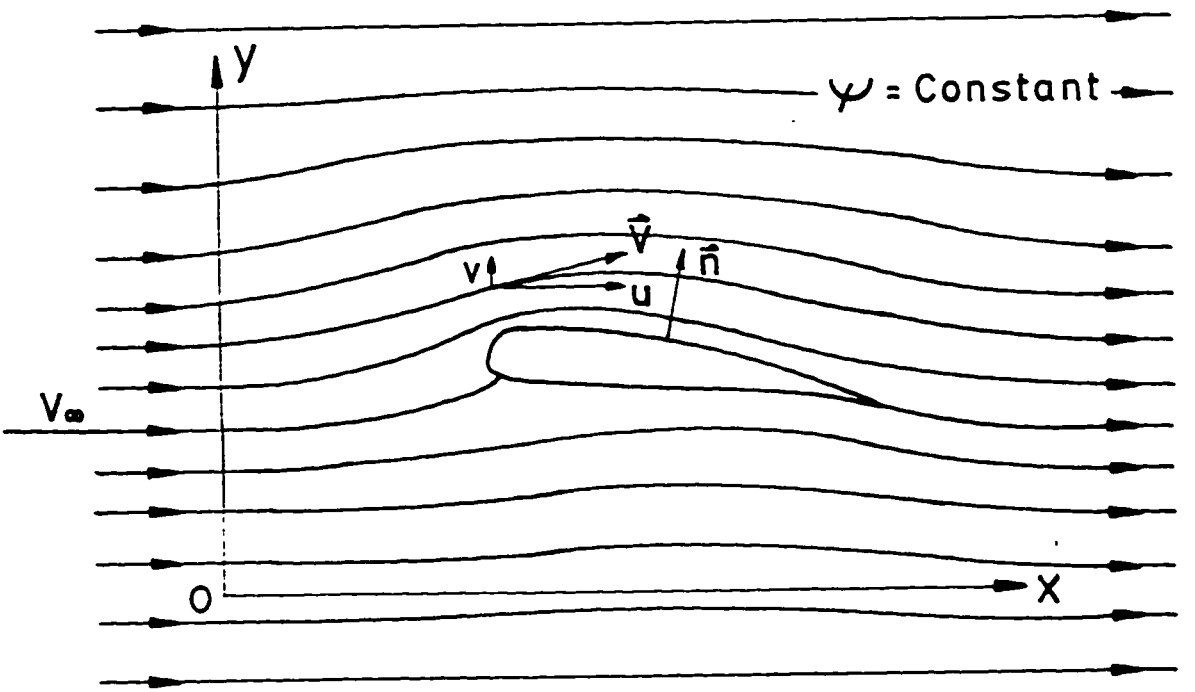

Fig. II.1: Flow Past a Two-Dimensional Body (Airfoil).

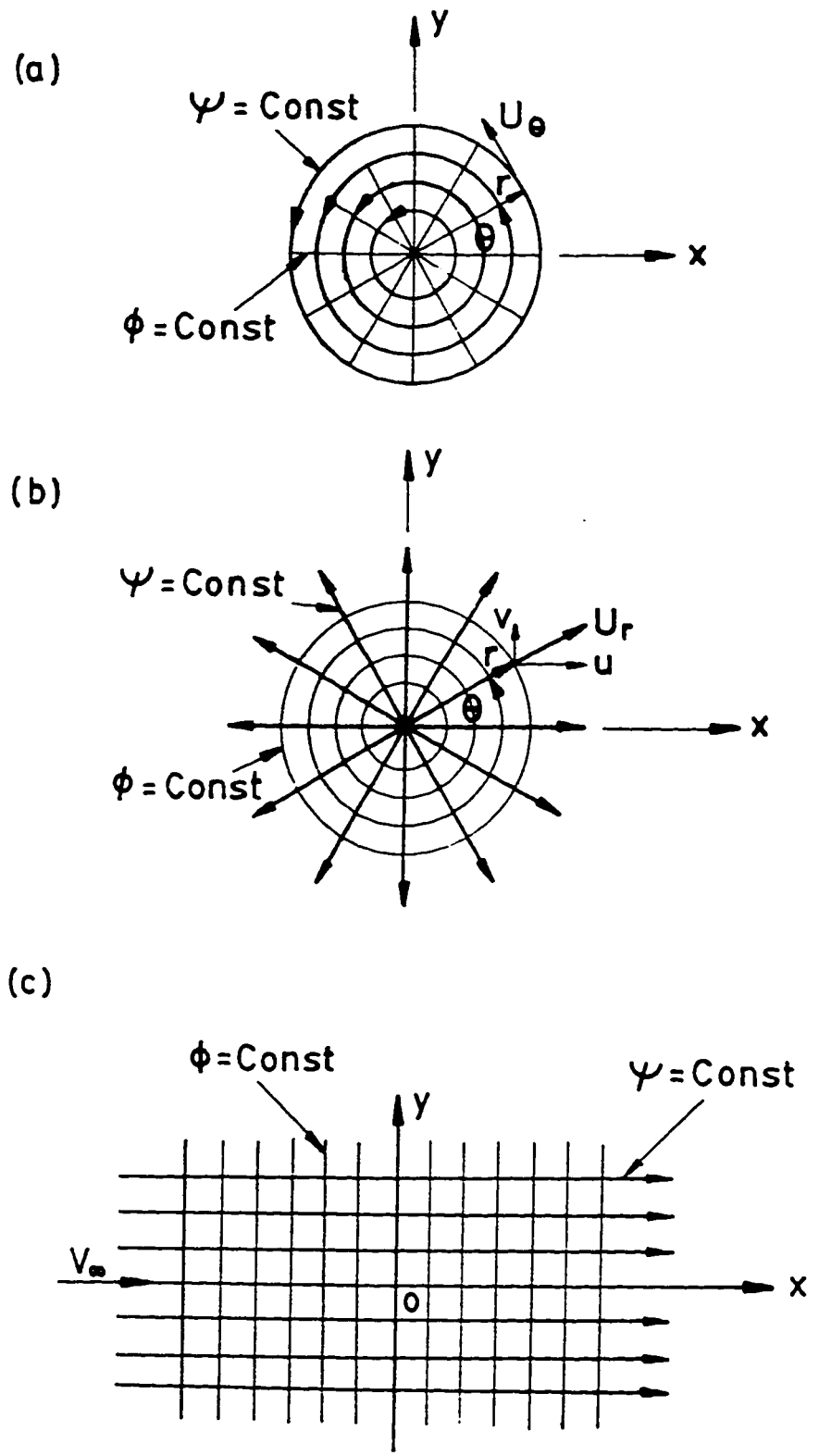

Fig. II.2 (a) Vortex Flow, (b) Source Flow, (c) Uniform Flow .

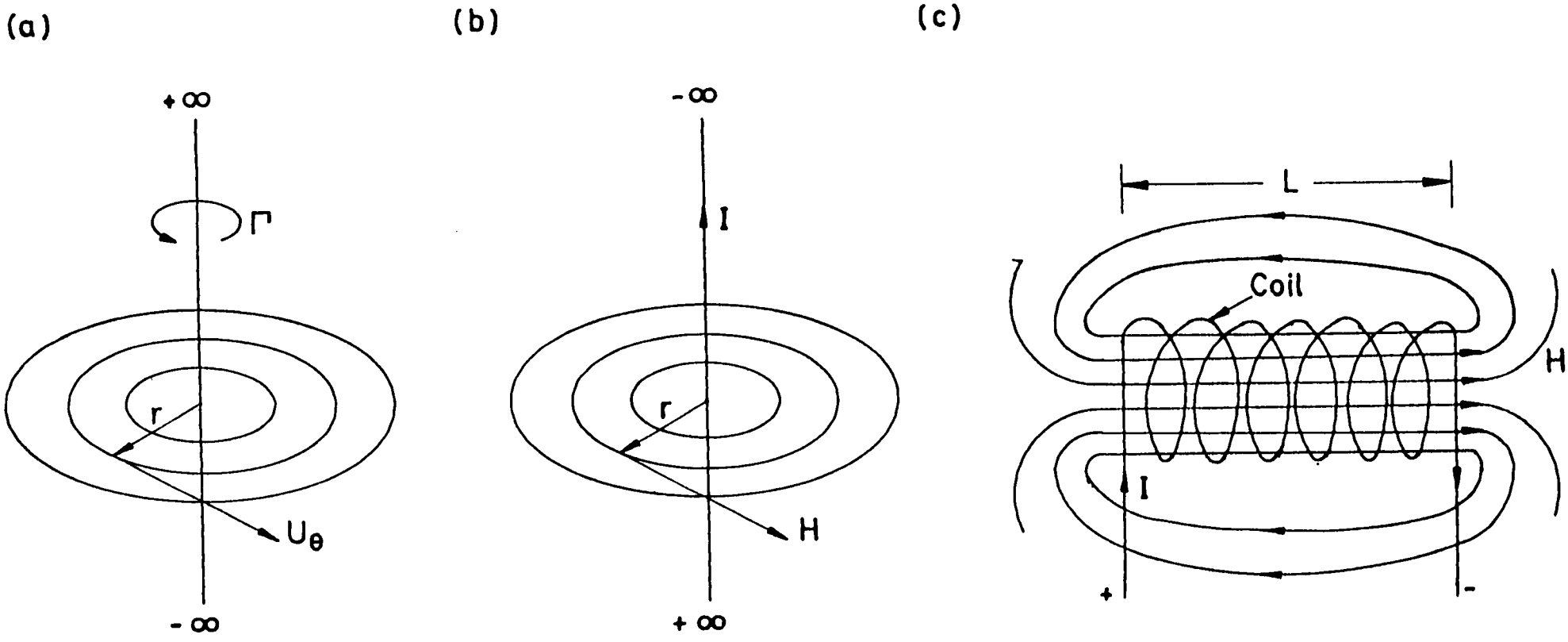

Fig. III.1 (a) Vortex Flow, (b) Magnetic Field Around a Wire, (c) Cylindrical Coil with Uniform Magnetic Field Inside .